TESE DE DOUTORADO Nº 140

OPTIMIZED MICROLENS-ARRAY GEOMETRY FOR HARTMANN-SHACK WAVEFRONT SENSOR: DESIGN, FABRICATION AND TEST

Otávio Gomes de Oliveira

DATA DA DEFESA: 29/02/2012

Universidade Federal de Minas Gerais

Escola de Engenharia

Programa de Pós-Graduação em Engenharia Elétrica

OPTIMIZED MICROLENS-ARRAY GEOMETRY FOR HARTMANN-SHACK WAVEFRONT SENSOR: DESIGN, FABRICATION AND TEST

Otávio Gomes de Oliveira

Tese de Doutorado submetida à Banca Examinadora designada pelo Colegiado do Programa de Pós Graduação em Engenharia Elétrica da Escola de Engenharia da Universidade Federal de Minas Gerais, como requisito para obtenção do Título de Doutor em Engenharia Elétrica.

Orientador: Prof. Davies William de Lima Monteiro

Belo Horizonte – MG

Fevereiro de 2012

"Optimized Microlens-Array Geometry For Hartmann-Shack Wavefront Sensor: Design, Fabrication And Test"

Otavio Gomes de Oliveira

Tese de Doutorado submetida à Banca Examinadora designada pelo Colegiado do Programa de Pós-Graduação em Engenharia Elétrica da Escola de Engenharia da Universidade Federal de Minas Gerais, como requisito para obtenção do grau de Doutor em Engenharia Elétrica.

Aprovada em 29 de fevereiro de 2012.

Por:

Prof. Dr. Davies William de Lima Monteiro
DEE (UFMG) - Orientador

Prof. Dr. Rodney Rezende Saldanha
DEE (UFMG)

Prof. Dr. Marcos Pinotti Barbosa
DEMEC (UFMG)

Prof. Dr. Paulo Schor
Departamento de Oftalmologia (UNIFESP)

Prof. Dr. Jose Paulo Rodrigues Furtado de Mendonça
Departamento de Física (UFJF)

Prof. Dr. Jarbas Caiado de Castro Neto
Instituto de Física e Ciência dos Materiais (USP - São Carlos)

To my parents, for once having dared to win.

“Aos meus pais, por um dia terem ousado vencer.”

ABSTRACT

The Hartmann-Shack (H-S) wavefront sensor is now deployed in many different fields, from astronomy to industrial inspection, where the quality of optical media or components can be measured by the distortions (wavefront aberrations) they impart on a wavefront transmitted or reflected by them. In ophthalmology, this sensor is a core component of major aberrometers, used in the assessment of the visual quality of the eye, academic research and clinical diagnosis.

The H-S wavefront sensor is also found in adaptive optics (AO) systems, which are used to improve the quality and the capabilities of optical systems, by compensating for wavefront aberrations that affect light waves. These image distortions can represent a serious problem in many different applications where high-quality images are demanded.

The microlens array is an important element in the H-S sensor, responsible for sampling the aberrated wavefront into light spots on the focal plane. The position of each light spot relates to the average tilt of the wavefront over the respective microlens. These spot-position coordinates are then used in the modal reconstruction to approximate the wavefront topology with a combination of orthogonal basis functions. The wavefront reconstruction error describes the deviation of the reconstructed wavefront from the reference one.

The wavefront sampling is influenced by the microlens distribution pattern in the array, lens contour and size, number of microlenses and fill factor. Adopted grids typically consist in either rectangular or hexagonal configurations. The influence of the array geometry on the wavefront reconstruction error was already discussed in the literature, which demonstrated that random arrays might perform better than regular ones.

This work proposes the optimization of the microlens-array geometry to be used in a specific context, such as ophthalmology. The workflow consisted of three major steps: numerical optimization, to find the optimal microlens arrays; fabrication of the arrays; and test on an optical bench, to comparatively assess the performance of the fabricated and commercial arrays.

The optimization comprises the minimization of the wavefront reconstruction error and/or the number of necessary microlenses in the array, considering a known aberration statistics. Within the ophthalmological context, as a case study, it was demonstrated by the numerical simulations that 10 or 16 suitably located microlenses can be used to produce reconstruction errors as small as those of a 36-microlens rectangular array.

The optimized arrays were then fabricated in a clean room, where KOH anisotropic etching was used to obtain the silicon molds from which the microlens arrays were replicated on polymer by casting. Four arrays were fabricated: 10- and 16-microlens optimized arrays and 16- and 36-microlens rectangular arrays.

All four arrays were tested and compared to a standard 127-microlens hexagonal commercial array, using an arbitrary wavefront aberration, which is compatible with the used ophthalmological wavefront-aberration statistics. The final results corroborate with the predictions of the computational simulations.

RESUMO

O sensor de frente de ondas de Hartmann-Shack (H-S) é aplicado a diversas áreas do conhecimento, da astronomia à inspeção industrial, em que a qualidade de meios ou componentes ópticos pode ser medida através das distorções (aberrações de frentes de onda) que eles inserem em uma frente de onda, seja por reflexão ou refração. Em oftalmologia, este sensor é um componente central da maioria dos aberrômetros, que são usados na avaliação da qualidade óptica do olho, em pesquisas e em diagnóstico clínico.

O sensor de frentes de onda de H-S é também encontrado em sistemas ópticos adaptativos, que são usados para aumentar a qualidade de sistemas ópticos, por meio da compensação de aberrações de frentes de onda. Essas distorções nas frentes de onda podem representar um sério problema em diversas aplicações que requerem imagens de alta qualidade.

A matriz de microlentes é um importante elemento no sensor de H-S, responsável pela amostragem da frente de onda aberrada em pontos de luz no flano focal. A posição de cada ponto de luz relaciona a inclinação média da parte da frente de onda amostrada pela respectiva microlente. As coordenadas das posições de todos os pontos de luz são usados no processo de reconstrução modal para aproximar a topologia real da frente de onda através de uma combinação de funções ortonormais. O desvio dessa aproximação é chamado de erro de reconstrução.

A amostragem da frente de onda é influenciada pelo padrão de distribuição das microlentes na matriz, formato e tamanho das microlentes, número de microlentes e fator de preenchimento da matriz. As matrizes comumente encontradas no mercado possuem, em geral, configuração retangular ou hexagonal. A influência da geometria da matriz sobre o erro de reconstrução já foi discutido na literatura, que demonstrou que geometrias aleatórias podem apresentar performance melhor do que as geometrias regulares.

Este trabalho propõe a otimização da geometria da matriz de microlentes para ser usada em um contexto específico, como oftalmologia. O trabalho consistiu de três fases: optimização numérica, para encontrar as matrizes ótimas; fabricação e teste em bancada óptica, para avaliar comparativamente a performance das matrizes fabricadas e uma matriz comercial.

A otimização consiste na minimização do erro de reconstrução e/ou do número de microlentes necessárias na matriz, considerando uma estatística de aberrações conhecida. No contexto oftalmológico, usado como estudo de caso, foi demonstrado pelas simulações que matrizes otimizadas com 10 ou 16 microlentes podem ser usadas para produzir erros de reconstrução da mesma ordem que matrizes retangulares com 36 microlentes.

As matrizes otimizadas foram então fabricadas em uma sala limpa, onde corrosão anisotrópica por KOH foi utilizada para obter-se moldes dos quais as microlentes foram replicadas em polímero. Foram fabricadas as matrizes otimizadas com 10 e 16 microlentes e também as matrizes retangulares com 16 e 36 microlentes. Todas as matrizes foram testadas e comparadas com uma matriz hexagonal comercial, com 127 microlentes. Os testes foram feitos com uma aberração arbitrária, mas compatível com a estatística estudada. Os resultados finais corroboram com os previstos pelas simulações computacionais.

SUMMARY

LIST OF FIGURES

LIST OF TABLES

1. INTRODUCTION

"If the Theory of making Telescopes could at length be fully brought into Practice, yet there would be certain bounds beyond which telescopes could not perform. For the air through which we look upon the stars, is in a perpetual tremor; as may be seen by the tremulous motion of shadows cast from high towers, and by the twinkling of the fix'd stars. But these stars do not twinkle when viewed through telescopes which have large apertures. For the rays of light which pass through divers parts of the aperture, tremble each of them apart, and by means of their various and sometimes contrary tremors, fall at one and the same time upon different points in the bottom of the eye, and their trembling motions are too quick and confused to be perceived severally. And all these illuminated points constitute one broad lucid point, composed of those many trembling points confusedly and insensibly mixed with one another by very short and swift tremors, and thereby cause the star to appear broader than it is, and without any trembling of the whole. Long telescopes may cause objects to appear brighter and larger than short ones can do, but they cannot be so formed as to take away that confusion of the rays which arises from the tremors of the atmosphere. The only remedy is a most serene and quiet air, such as may perhaps be found on the tops of the highest mountains above the grosser clouds." (NEWTON, 2007).

When trying to observe fainter astronomical objects (such as other galaxies), using large telescopes, astronomers faced a limitation: images appeared blurred and the objects could not be distinguished. The reason was that light coming from the astronomical object passed through turbulent atmosphere before reaching the telescope lenses (HEIN, 2005). As claimed by Sir Isaac Newton in his *Opticks*, the "quiet air" of high mountains contributes to better observations. However, even such a "serene air" is prone to contain turbulences, and therefore, to decrease the quality of the observed image by introducing aberrations in the light beam that passes through it.

Despite representing a big problem in fields such as astronomy, communications and defense, it was only in the second half of the 20th century that astronomers and the military started to develop ways of overcoming turbulent effects of the atmosphere. Although it is impossible to avoid the introduction of aberrations in the images when light passes through the atmosphere, it is feasible to compensate for these aberrations, using a deformable element in the optical system. Basically, in practice, the system must be capable of detecting the deformation present in the image, quantifying it and converting the results into information useful to actuate the deformable element. A requirement is that all this has to be continually performed in a loop and in real-time. Hence, an optical system like this would constantly adapt itself to the atmospheric turbulence, therefore compensating for the deformations present in the observed images.

Aberrations are introduced not only by atmosphere. Actually, any transparent medium is likely to introduce some degree of deformation to the light beam that traverses it. This makes the problem of detecting, quantifying and even eventually correcting, of great importance in many different areas. Besides astronomy and defense, industry and medicine also can benefit from measuring aberrations. Particularly in ophthalmology, these aberrations can be inserted by the optical components of the human eye. This may imply in decreased vision quality, depending on what are the aberrations like.

Hence, measuring the aberrations is of great importance to find ways of overcoming the problems imposed by them. In ophthalmology, this is done by means of equipment referred to as aberrometers. There are several different methods to measure aberrations both qualitatively and quantitatively, as will be discussed later. The most widely used method is called Hartmann-Shack. In this method, the core component is a microlens array, which is responsible for sampling the aberrated light beam into light spots on the focal plane. The positions of the light spots are directly related to the amount of aberration present in the beam. Thus, if these positions are measured, the aberration can be quantified after some computer processing.

The distribution pattern of the microlenses on the array influences on how it samples a given set of aberrations. Therefore, a pattern that is optimized to fit a given aberration statistics provides benefits such as reduction of the measurement error and/or reduction in the necessary processing time to obtain a mathematical description of the aberration.

The objective of this work is to optimize the microlens array to be used in the measurement of ocular aberrations. This is accomplished in basically three steps. First, a numerical method is proposed to find the distribution pattern of the microlenses in the optimized arrays. Second, the resulting arrays are fabricated. At last, they are tested in an actual optical setup.

2. OPTICAL ABERRATIONS

2.1. WAVEFRONTS

An optical aberration can be understood as a distortion in a wavefront introduced by optical components or by the propagating medium. To define it more precisely and to understand how it can affect the image quality, it is important to first introduce the concept of a wavefront.

Let L be a light beam travelling from left to right. The electrical field vector associated to the beam can be written as a combination of specific plane waves (DE LIMA MONTEIRO, 2002; HECHT, 2002). In a general form, the electrical field vector $\boldsymbol{E}$ due to an electromagnetic field can be expressed as in equation 1.

$$\boldsymbol{E}(x, y, z, t) = \boldsymbol{A}(x, y, z, t) \cdot e^{i\phi(x,y,z,t)} \qquad 1$$

where x, y and z are the spatial coordinates, t is the time, $\boldsymbol{A}$ is the amplitude and ϕ is the phase (GREIVENKAMP, 1995).

The hypothetical surfaces for which all the components of the electrical field have the same phase are called optical wavefronts, as illustrated in Figure 1. The wavefront is also sometimes called a phasefront.

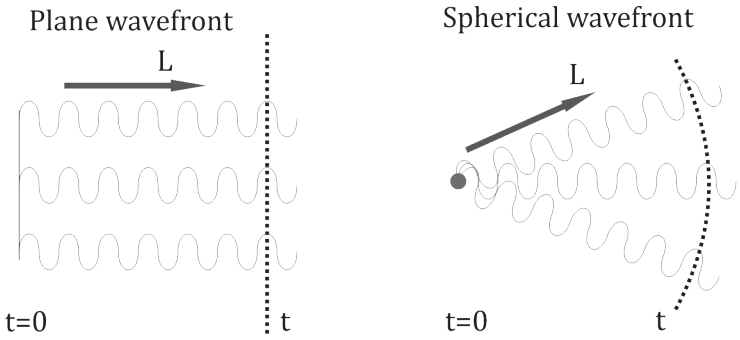

Figure 1 – Wavefronts (dashed line) for parallel and spherically divergent light beams.

A connection can be made between geometrical and wave optics, if it is taken into account that the local normal vector to the wavefront corresponds to the propagation direction of the field. Then, a wavefront can also be defined in geometrical optics as a surface that has normal vectors parallel to the light rays.

In other words, an optical wavefront can also be defined as the surface of constant optical path length (OPL) from the source (OPTICAL SOCIETY OF AMERICA, 1994; GREENAWAY and BURNETT, 2004). The OPL is given by:

$$OPL = \int_{S'}^{O} n(s) \cdot ds \qquad 2$$

where n is the index of refraction of the propagating medium, S' is the source point, O is the observation point and s describes the propagation path. If a wavefront corresponds to a flat surface, it is said to be a plane wavefront. In the same manner, if it corresponds to a spherical surface, it is called a spherical wavefront, and so on.

When the phase pattern of the electrical field of a light beam becomes distorted, the wavefront changes its shape and is hence referred to as aberrated. The distortions introduced to the wavefront can compromise a quality parameter in the information it carries. The altered parameter can be, for instance, intensity, contrast or delay, depending on the information carried being power, image or sequential signal. Often, the aberration itself is the parameter of interest, as it represents an imprint of the medium or object the wavefront has traversed – refracted or reflected, thus providing a contactless method to probe its shape or homogeneity.

2.2.ABERRATIONS

In some cases, it is useful to describe, rather than the wavefront shape, the difference between the actual wavefront and a reference one, which can be the initial or the desired wavefront. Common reference wavefronts[1] are the plane and spherical ideal wavefronts. In this sense, the wavefront aberration W can be defined as the optical path length from the reference to the actual wavefront, as illustrated in Figure 2 (YOON, 2003). In this work, the term optical aberration, or simply aberration, is used with the same meaning as the term wavefront aberration.

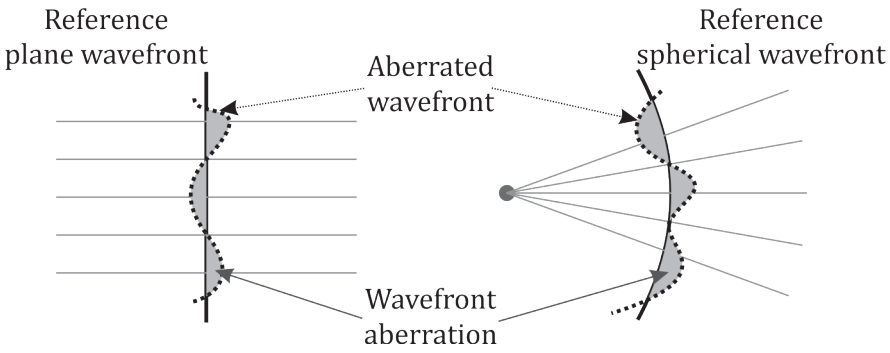

Figure 2 – Wavefront aberration.

From equation 2, it can be noted that when a wavefront passes through a medium with different refractive indices, the different rays that compose the beam will have different OPL and therefore the wavefront will no longer have the same shape, as shown in Figure 3 (DE LIMA MONTEIRO, 2002). Two parallel plane-waves, A and B, go from a to a' and from b to b', respectively, through a medium with index of refraction $n = 1$. At point P_1, both waves have the same phase ϕ_1. Between points P_1 and P_2, wave A passes through a medium of length L and index n, which introduces a phase delay in the wave. As a consequence, at point P_2, wave B has the same phase as wave A at point P_2' and wave A has the phase ϕ_3. Therefore, at a' and b', the waves are not in phase, as they were at a and b.

[1] Those reference wavefronts are for general optical systems. In ophthalmology, a convenient reference could be a sphero-cylindrical wavefront, which contains a degree of defocus and astigmatism (see section 2.3).

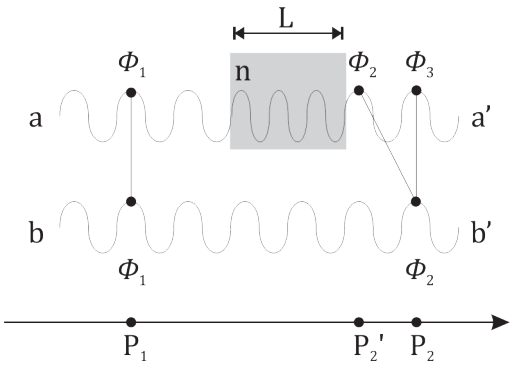

Figure 3 – Wavefront aberration introduced by a non-isotropic medium.

The fluctuations in the index of refraction through an optical path may occur for many different reasons: thermal fluctuations, gases, fog and turbulence in general.

Another situation in which the shape of a wavefront may be altered is when a light beam reaches a non-flat optical surface. It can be a surface separating two different transparent media or a reflective surface. In the former case, the aberration is introduced through refraction and, in the latter, through reflection. Figure 4 shows the aberration introduced in a plane wavefront by a lens and Figure 5, by a non-flat mirror.

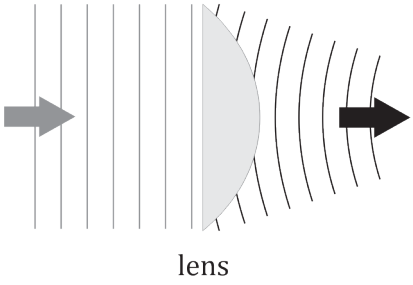

Figure 4 – Aberration introduced through refraction.

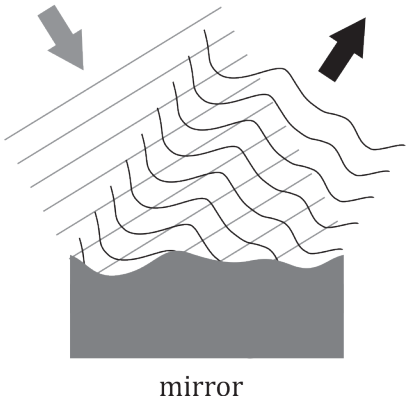

Figure 5 – Aberration introduced through reflection.

In the first case, those rays passing through the center of the lens and the ones passing close to the edges will have different OPL, once it depends on the length of the path inside the component, as can be noted from equation 2. It means that an initially plane wavefront will have the shape of the lens surface imprinted on it. The same analysis stands for when the aberration is introduced through reflection. Different regions of the deformed surface of the mirror will alter the OPL of the rays, which compose the beam. Then, a wavefront which was initially plane, for instance, will have the shape of the reflective surface imprinted on it, i.e., the wavefront will become aberrated.

It is important to note, in the lens case, that the shape of the outcoming wavefront corresponds to the lens shape with attenuated amplitude. That is due to the OPL dependency on the index of refraction (n) of the refractive element. The attenuation is proportional to $n - 1$. On the other hand, the amplitude of the aberration introduced by the mirror is twice the amplitude of the shape of the mirror. That is illustrated in Figure 6.

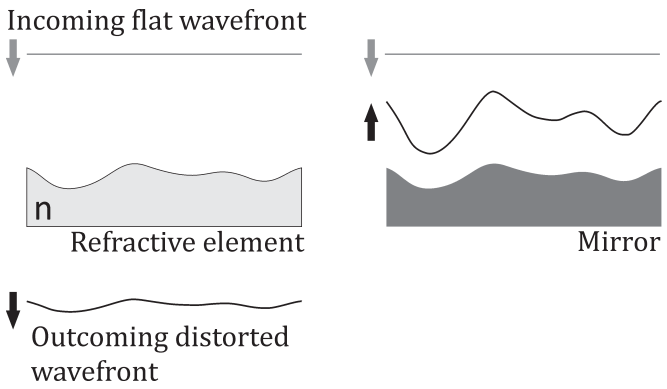

Figure 6 –Aberrated wavefronts after influenced by optical components with the same surface profile: (left) refractive, with refractive index n, and (b) reflective.

Wavefront aberrations vary with the wavelength, once the index of refraction depends on that. When several different wavelengths are present, the aberrations are said to be chromatic. In the case when only one wavelength is taken into account, the aberrations are said to be monochromatic, which is the case of the present work.

The first published systematic treatment of geometrical monochromatic aberrations was due to Seidel, who mathematically described five basic aberrations, which arise from a third-order approach of light propagation through real lenses (BORN and WOLF, 1989). The five primary Seidel aberrations are: spherical aberration, coma, astigmatism, curvature of field and distortion. They are described in the next paragraphs.

2.2.1. SPHERICAL ABERRATION

The spherical aberration can be defined as the variation of focal distance with aperture diameter (SMITH, 2007). In the geometrical optics theory, the focal distance of a spherical lens is well defined only if the light beam impinges on a small central region of the lens, what is called the paraxial approximation. Otherwise, the theory predicts a variation on the focal distance according to the position where rays impinge on the lens surface relative to the optical axis[2] (BORN and WOLF, 1989). Figure 7 illustrates the spherical aberration introduced by a simple converging lens[3]. It happens because rays (R) that impinge on the periphery of the lens are more deviated than the paraxial rays. Thus, those rays intersect the optical axis ($\overline{OA}$) before the paraxial focus (A). The distance (LA') from the paraxial focus to the axial intersection B is called longitudinal spherical aberration. When the spherical aberration is measured on the focal plane (AC), it is called transverse or lateral spherical aberration (TA').

[2] The spherical aberration can be easily observed with spherical lenses. Actually, it depends also on the lens surface. Theoretically, lenses with refractive index higher than the surrounding media and with hyperbolic surfaces do not introduce any spherical aberration. They are called aspherical lenses.

[3] In the present work, it is always assumed that the lens has a larger index of refraction than the one of the medium where it is immersed.

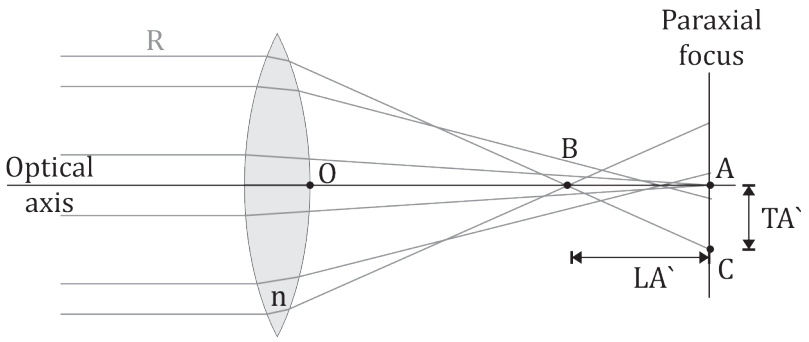

Figure 7 – The spherical aberration schematics in a spherical lens.

2.2.2. COMA

The coma aberration is due to the dependence of transverse magnification on the aperture diameter (HECHT, 2002; BORN and WOLF, 1989). It is particularly evident when the ray bundle is oblique and the image point is off-axis. This is illustrated in Figure 8, where the marginal rays, i.e. the ones that impinge on the periphery of the lens, arrive at the focal plane closer to the axis than the rays in the vicinity of the principal ray, i.e. the one that passes through the lens center. Coma also depends on the lens shape and can therefore be minimized. The shape for which coma is zero for distant objects is nearly convex-planar (HECHT, 2002). In practice, when dealing with collimated beams, as is often the case in aberrometry, it is important to guarantee that the beam impinges parallel to the lens optical axis and centered to it.

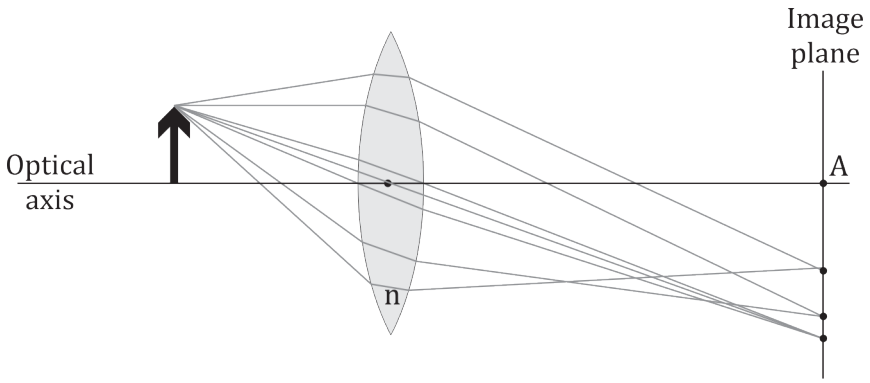

Figure 8 – Illustration of the coma aberration generated by a spherical lens.

2.2.3. ASTIGMATISM

Astigmatism occurs when tangential and sagittal rays do not focus at the same plane (SMITH, 2007), as illustrated in Figure 9. The figure shows that a distant point source is imaged as two different separate lines: the tangential and the sagittal focal lines. Between these two astigmatic foci, the image is an elliptical or circular blur. Astigmatism occurs when the lens surface presents different curvature radii in a pair of perpendicular planes (sagittal and tangential). This difference implies in distinct focal distances for the rays that impinge in both planes. In some cases, a lens may be intentionally designed to be astigmatic. Such lenses are useful to compensate for the astigmatism already present in the light beam, or assistive optical system. They are commonly called toric lenses, since their surface has the form of a toroid. Toric lenses are particularly employed in

ophthalmology to compensate for the astigmatism introduced by the cornea (see section 5.1 for a description of the human eye). In a general optical system, this correction can be achieved also with the use of mirrors, also designed with different curvature radii in different perpendicular planes.

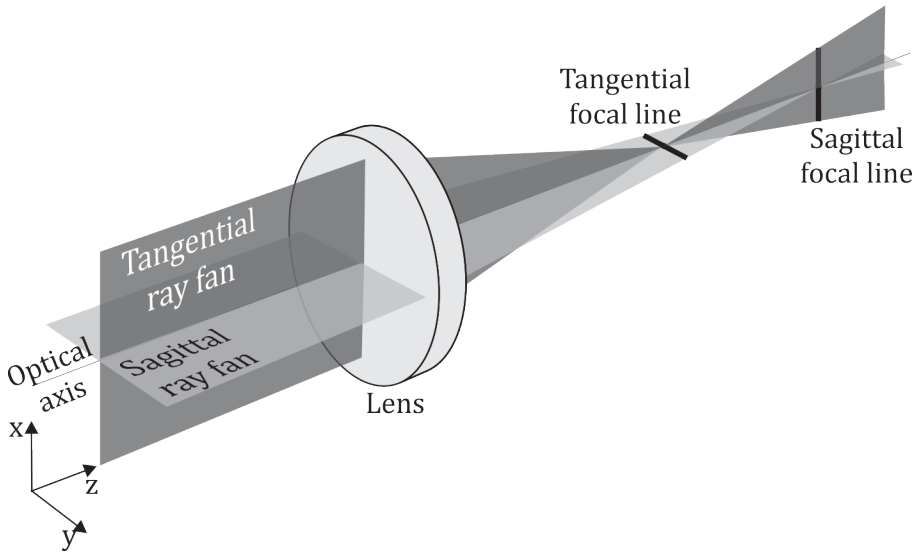

Figure 9 – Illustration of astigmatism introduced by a spherical lens.

2.2.4. CURVATURE OF FIELD

The curvature of field, also called Petzval curvature or field of curvature, is an aberration that causes planar objects to appear curved in the image. That means that the focal surface, where the image is generated, is curved instead of plane, as expected by the paraxial theory. In the absence of astigmatism, this surface is a paraboloid and is called the Petzval surface. (HECHT, 2002) This aberration is more evident for off-axis images and is illustrated in Figure 10.

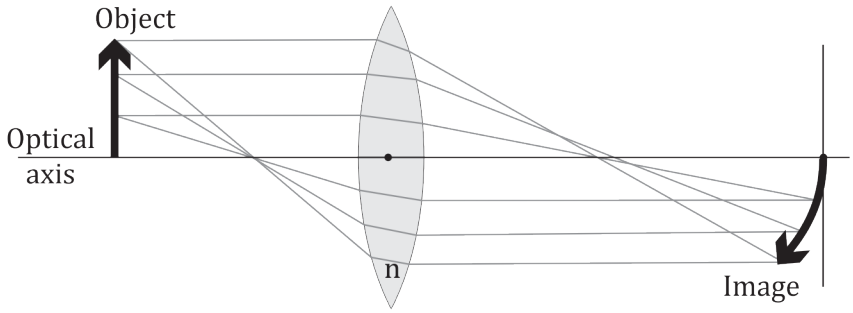

Figure 10 – Field of Curvature.

2.2.5. DISTORTION

The aberration called distortion happens when the image of an off-axis point is formed farther from or closer to the optical axis than where it is determined by the paraxial approximation. In the former case, the distortion is called pincushion. In the latter, it is called barrel (SMITH, 2007). If an object line is considered together with the absence of the other aberrations, distortion causes its image to bend inwards (pincushion) or

outwards (barrel) with respect to the optical axis. Figure 11 shows distortion in the image of a square grid. Distortion appears when the image magnification is a function of the off-axis image distance so that the realized position of each image point is different from the predicted one (HECHT, 2002). In general, all lenses introduce some degree of distortion. However, those with strongly curved surfaces present higher levels of distortion. A common and practical technique to reduce distortions in an optical system is to use compound lens system approximately symmetrical about a stop center (CHEN, SU, *et al.*, 2010).

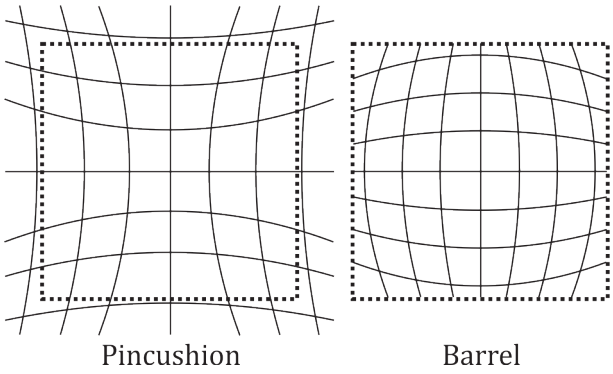

Figure 11 – Distortion aberration: pincushion (on left) and barrel (on right).

2.3.QUANTITATIVE DESCRIPTION OF OPTICAL ABERRATIONS

Once the wavefront aberrations concept is understood, as well as its effects, it is convenient to represent them mathematically. There are two methods by which the wavefront may be represented: zonal estimation[4] and modal estimation. According to Southwell (1980), the latter is superior to the former in terms of error propagation and is also computationally easier and faster. It is the one used in this work.

In the modal estimation, it is assumed that a wavefront can be described by an infinite sum expansion of orthogonal functions (CUBALCHINI, 1979). In other words, the wavefront can be represented by the weighted superposition of orthogonal two-dimensional basis functions, also referred to as spatial modes, Zernike modes or Zernike terms.

Commonly the wavefront aberrations are represented by the Zernike polynomials[5] (BORN and WOLF, 1989). Zernike polynomials are a set of polynomials defined on a unit circle and, therefore, can be easily described in polar coordinates as a product of angular functions and radial polynomials. The angular functions are the basis functions for two-dimensional rotation group, and the radial polynomials are derived from Jacobi polynomials (NOLL, 1976).

---

[4] The zonal estimation is a discrete approach to describe the wavefront shape $W(x, y) = z$ point by point in a mesh. It consists in attributing values (z), which represent the surface height, to discrete mesh points (x, y) in space. The wavefront shape may be visualized by a wire frame connecting all z points in the three dimensional space.

[5] Recently, an alternative orthogonal polynomial basis has been proposed to describe the wavefront shape: the Forbes polynomials (FORBES, 2012; FORBES, 2010).

There is no general strict correspondence between Zernike polynomials and Seidel aberrations. When only low-order aberrations are considered, spherical aberration, coma and astigmatism can be directly represented by single Zernike terms. Otherwise, aberrations such as distortion and field curvature are represented as a weighted sum of different Zernike terms.

Zernike polynomials are convinient to describe wavefront aberrations because they are orthogonal over a unit circle and most of the optical components, apertures and laser beams are circular. This set of polynomials is often used also because it is made up of terms that are of the same form as the types of aberrations often observed in optical tests (ZERNIKE, 1934 *apud* WYANT and CREATH, 1992). These terms are linearly independent and represent individually different types of aberrations. Therefore, an aberrated wavefront $W(\rho,\varphi)$ may be represented by a sum of Zernike terms $Z_j(\rho,\varphi)$ conveniently weighted through multiplication by coefficients (C_i), as shown in equation 3.

$$W(\rho,\varphi) = \sum_{j=0}^{\infty} C_j Z_j(\rho,\varphi) \qquad 3$$

It is important to emphasize that the Zernike terms are defined with amplitude ranging from -1 to $+1$ with zero average. The actual amplitude of each term in a real wavefront aberration is determined by the value of the coefficients (C_i).

There is no universal standard for Zernike terms indexation (WYANT and CREATH, 1992). Here, j is used for single-index ordering, which is convenient for numerical purposes. Different authors may however use different indexation standards. A common single-index indexation scheme is proposed by Noll (1976).

Another common way for ordering Zernike terms is to use a double index: n and m. Each of the Zernike polynomials is composed by three components: normalization factor, radial-dependent component and azimuthal-dependent component. The index n describes the highest power (order) of the radial component and m describes the azimuthal frequency of the sinusoidal component (PORTER, QUEENER, *et al.*, 2006).

Thibos *et al.* (2002) proposes a conversion standard from single- to double-index schemes and vice-versa, as shown in equations 4 and 5.

$$j = \frac{n(n+2)+m}{2} \qquad 4$$

$$n = roundup\left[\frac{-3+\sqrt{9+8j}}{2}\right] \qquad 5$$

$$m = 2j - n(n+2)$$

Zernike polynomials are defined, in polar coordinates, as in equation 6 (BORN and WOLF, 1989).

$$Z_n^m(\rho,\varphi) = \begin{cases} R_n^m(\rho)\cos(m\varphi), & m > 0 \\ R_n^{|m|}(\rho)\sin(|m|\varphi), & m < 0 \\ R_n^m, & m = 0 \end{cases} \qquad 6$$

where n and m are integers, $n > 0$, $n \geq |m|$, $n - |m|$ is even, ρ is the normalized radial distance, φ is the azimuthal angle in radians and R_n^m is the radial term, defined as in equation 7.

$$R_n^m(\rho) = \sum_{k=0}^{(n-m)/2} \frac{(-1)^k (n-k)!}{k!\left(\frac{n+m}{2}-k\right)!\cdot\left(\frac{n-m}{2}-k\right)!}\rho^{n-2k} \qquad 7$$

The polar coordinates ρ and φ are defined according to Figure 12.

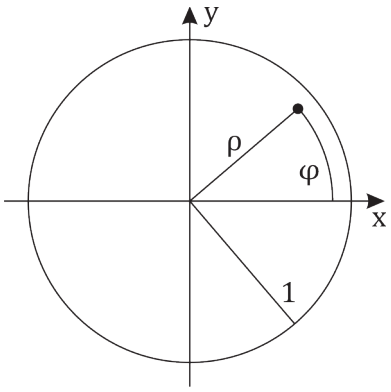

Figure 12 – Polar system coordinates.

The equations for some Zernike terms are show in Table 1. A three-dimensional representation for some terms, as well as commonly used names, is shown in Figure 13.

Table 1 – Zernike terms.

j	n	m	$Z_n^m(\rho,\varphi)$	Name
0	0	0	1	Piston
1	1	-1	$2\rho\sin(\varphi)$	y-Tilt
2	1	1	$2\rho\cos(\varphi)$	x-Tilt (Tip)
3	2	-2	$\sqrt{6}\rho^2\sin(2\varphi)$	Astigmatism 45°
4	2	0	$\sqrt{3}(2\rho^2-1)$	Defocus
5	2	2	$\sqrt{6}\rho^2\cos(2\varphi)$	Astigmatism 0°
6	3	-3	$\sqrt{8}\rho^3\sin(3\varphi)$	Trefoil
7	3	-1	$\sqrt{8}(3\rho^3-2\rho)\sin(\varphi)$	y-Coma
8	3	1	$\sqrt{8}(3\rho^3-2\rho)\cos(\varphi)$	x-Coma
9	3	3	$\sqrt{8}\rho^3\cos(3\varphi)$	Trefoil

The first Zernike term is called piston ($n=0, m=0$) and corresponds to a variation in the absolute value of the OPL for the whole light beam, i.e., it corresponds to a uniform shift in the whole wavefront along the optical axis. Therefore, the piston term does not represent an aberration, but actually an overall delay, and is generally not taken into account.

Referring to Table 1, the radial orders for $n=1$ and $n=2$ are generally referred to as low-order aberration, while the others are called high-order aberrations. However, this classification is not standardized and may vary from author to author.

The tilt terms ($n=1$) affect the wavefront by causing a shift of its center location in the focal plane. The control of the beam tilt is important in any adaptive optics system, once it can keep the light beam aligned with the optical components along the setup. In astronomical applications, for instance, the wavefront tilt is a dominant effect, which affects the wavefront estimation, once it varies rapidly during the exposure time.

Therefore, adaptive optics systems often attribute the task of correcting for wavefront horizontal and vertical tilts to a specialized tip-tilt control mirror, while the wavefront modulator (see section 5.2) is used to correct for aberrations with radial orders higher than 2 (TYSON, 1999).

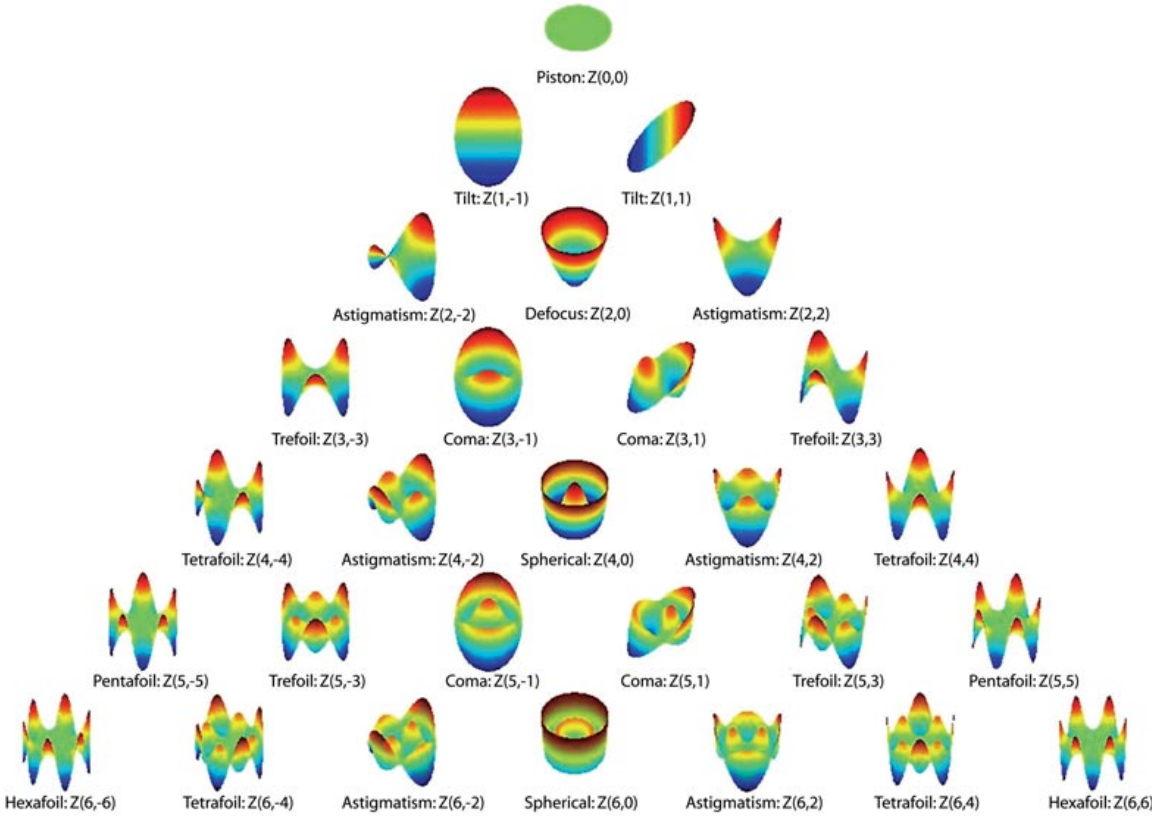

Figure 13 – 3D representation of Zernike terms.

The defocus term is commonly dominant in wavefront aberration measurement, especially in ophthalmology where the eye exhibits a considerable dioptric power when compared to the other usually occurring high-order eye aberrations. The dioptric power of a lens measures the power to which a lens can bend the propagation direction of light rays. It is defined as the reciprocal of the focal length, in meters, and is given in diopters, in the MKS unit system.

2.4.EFFECTS OF ABERRATIONS ON OPTICAL SYSTEMS

When aberrations are introduced in a beam, which carries the information of an image, the common effects are blurring, smearing and intensity/contrast reduction of the image (TYSON, 1999). An easy way to understand how wavefront aberrations introduced by an optical system can affect the quality of an image is to consider its point spread function (PSF). The point spread function is the image that an optical system forms of a point source. From the PSF information, it is possible to build the image of an arbitrary object, generated by an optical system. The image can be obtained from the convolution operation

of the system PSF and the object. Therefore, systems with poorly resolved PSF generate images of reduced quality.

In geometrical optics, a perfect system would generate a point as the image of a point source. However, in practice, even the perfect optical systems are diffraction-limited and the image observed for a point source, i.e., the PSF for such systems, is an Airy disc.

In Figure 14, it is illustrated the PSF for a diffraction-limited system. When a light beam passes through an aperture or lens, it undergoes the diffraction effect (HECHT, 2002). That means that, for a perfect lens, the observed image at the focal plane consists of a sequence of concentric rings where the center is the brightest region and the outer rings are less intense than the inner ones. The top-right inlet graph shows the light intensity distribution over the focal plane.

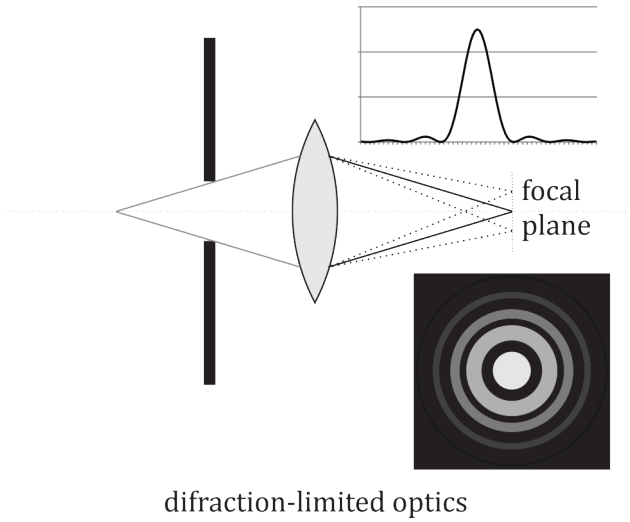

Figure 14 – Image formation of a point source for a diffraction-limited system.

The diffraction-limited system illustrated in Figure 14 can be a simplified model of a perfect human eye, for instance, where the lens[6] corresponds to the eye compound lens system (cornea and crystalline lens – see section 5.1 for a description of the human eye), and the focal plane corresponds to the retina.

Perfect systems, such as the ideal simplified model of the human eye, generate diffraction-limited images, once they do not introduce any aberration in the incoming wavefront. When the system is aberrated, i.e., when it introduces aberrations in the light beam, the PSF becomes distorted. This is illustrated below by comparing the PSF for a perfect eye (Figure 15) and for an emmetropic eye (Figure 16). In both figures, the PSF is shown for different pupil diameters, ranging from 1 to 7 mm. The pupil diameter refers to the diameter effectively used with the lens and the smaller it is, the larger the disc diameter at the focal plane.

The PSFs for an emmetropic eye demonstrate the effect of aberrations in the image of a point source to be observed at the retina. These aberrations are introduced mainly by the cornea and crystalline lens of the eye. It can be noted that the larger the pupil diameter,

[6] In this case, the lens would be aspherical with hyperbolic surface.

the stronger the effect of the aberrations. It is interesting to highlight that the pupil diameter is automatically and involuntarily controlled in the human eye according to the light intensity of the environment ranging usually from 3mm to 6mm (GUYTON and HALL, 1997)]. The larger diameters occur for darker environments, so that more light can enter in the eye. It is also important to emphasize that the aberrations not only distort the observed image, but also cause a reduction in the peak light intensity on the focal plane. All these effects caused by the presence of aberrations contribute, therefore, to a decrease in the vision quality. Any available ways of correcting or compensating for these effects would bring benefits to vision acuity. As an example, Sabesan *et al.* (2007) demonstrated the effectiveness of customized soft contact lenses to reduce significantly the high-order aberrations in keratoconic eyes[7], guaranteeing therefore a normal quality of vision to those abnormal corneal patients.

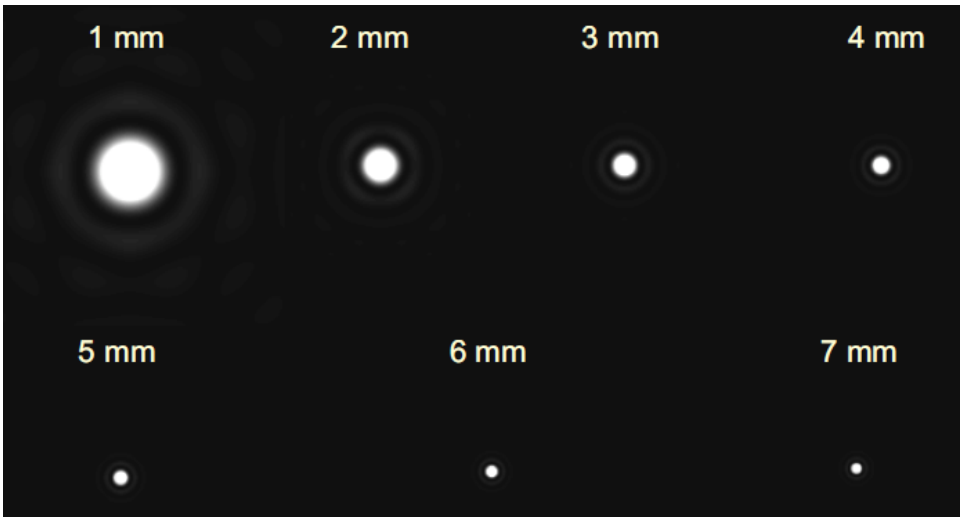

Figure 15 – Point spread function (PSF) for a perfect eye (YOON, 2003).

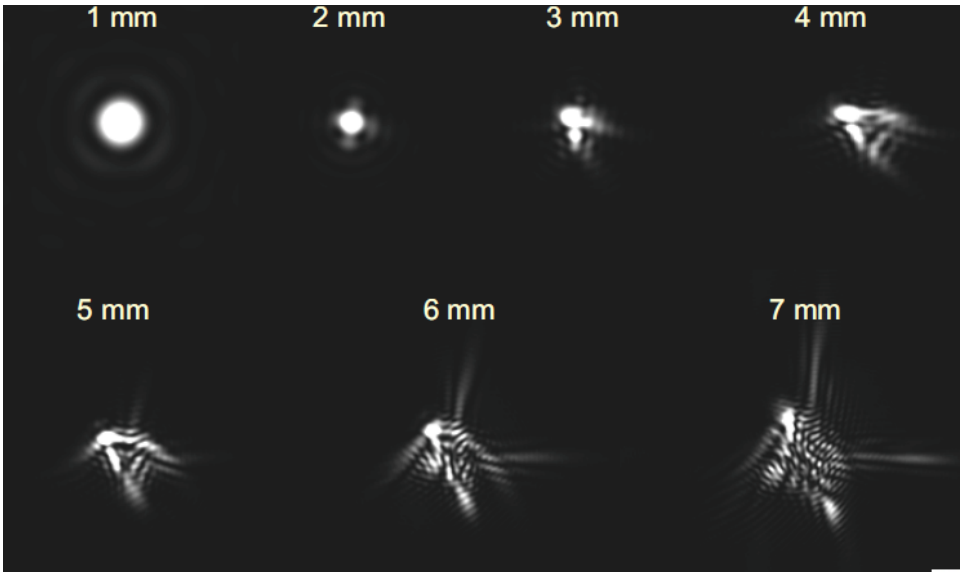

Figure 16 – Point spread function for an emmetropic eye (YOON, 2003).

[7] Keratoconus is a disorder that affects the cornea and causes it to change its shape into a conical form.

The PSF for some of the Seidel aberrations about the focal point is illustrated bellow, in Figure 17 through Figure 19.

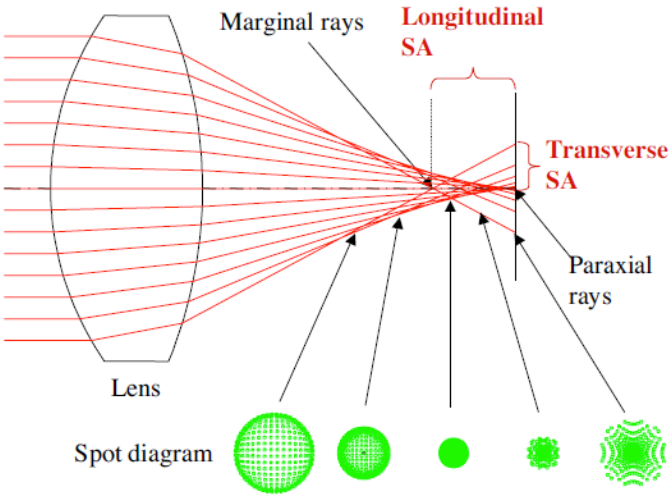

Figure 17 – The PSF and spot diagram for the spherical aberration (YOON, 2003).

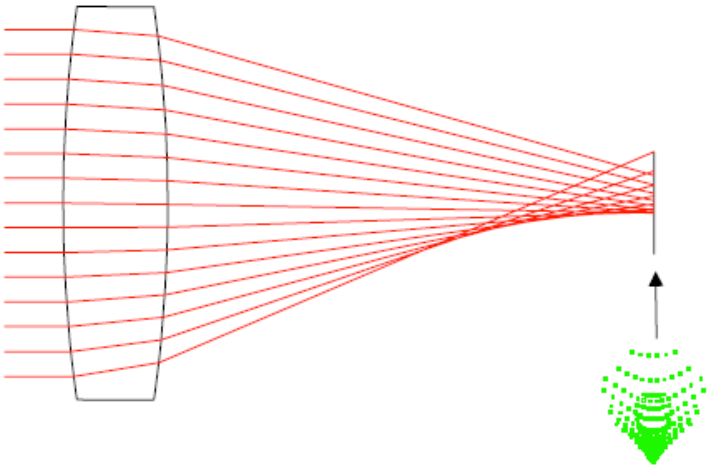

Figure 18 – The PSF for comma aberration (YOON, 2003).

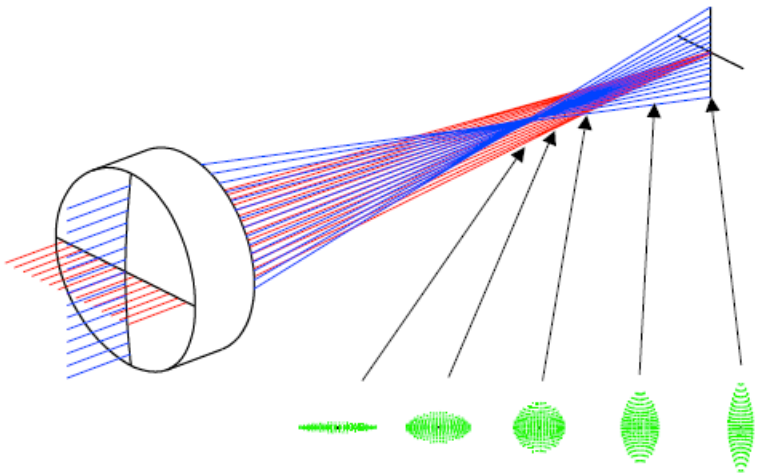

Figure 19 – The PSF and spot diagram for astigmatism (YOON, 2003).

Since aberrations can be described in terms of Zernike polynomials, it is important to realize the contribution each of the Zernike modes has to the PSF of an optical system. The PSF for each of the Zernike terms illustrated in Figure 13 is shown in Figure 20.

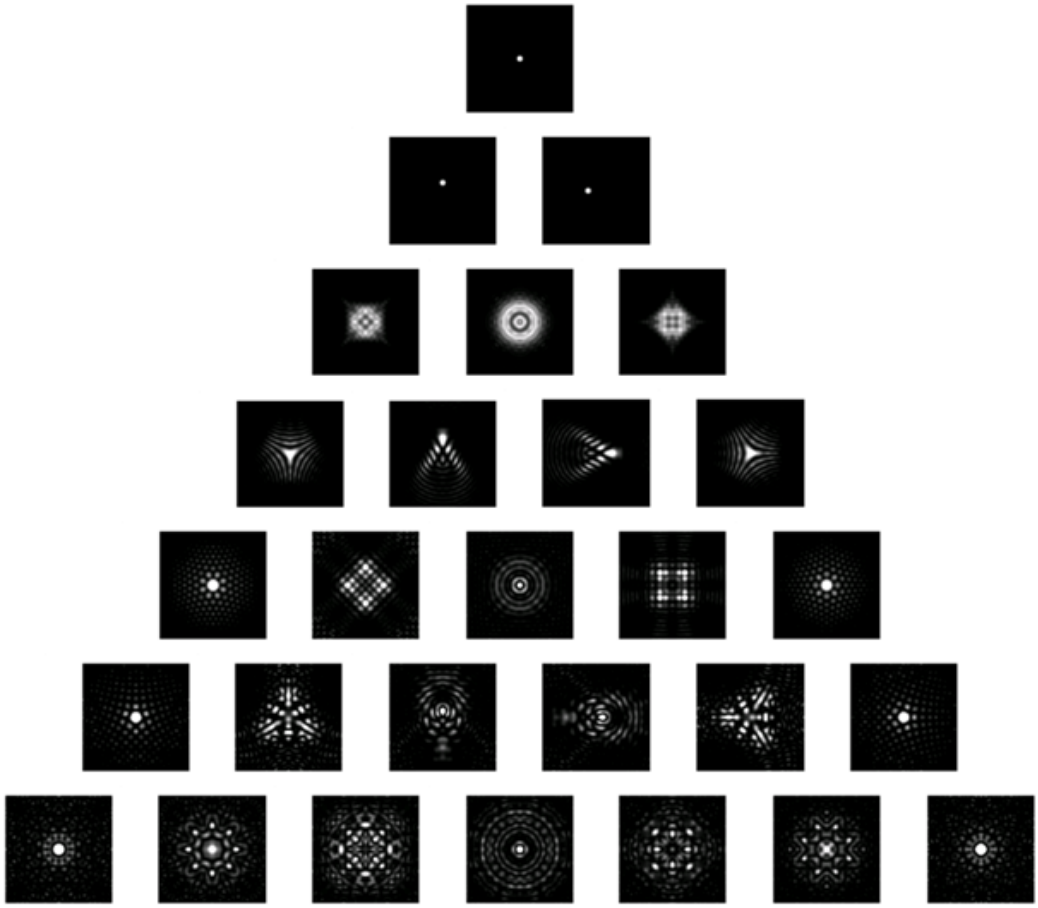

Figure 20 – Point Spread function for each Zernike term (MAEDA, 2003)

To illustrate how a wavefront aberration can affect the quality of the observed image, consider an optical system with the PSF shown in Figure 21a (the human eye lens, for example). Let Figure 21b be the object to be observed using the system. The output of the optical system, i.e., the image observed in practice, is shown in Figure 21c.

(a) (b) (c)

Figure 21 – Image formation by an aberrated optical system. (a: PSF, b: object and c: result of the convolution of a and b) (YOON, 2003)

Some other examples of images formed in human eyes with different PSFs are shown in Figure 22. The pupil diameter is 5.7 mm for all cases. The image on the left is a reference

for a perfect eye. One can still observe some blurring, but this is due to non-ideal copying and printing of the presented images.

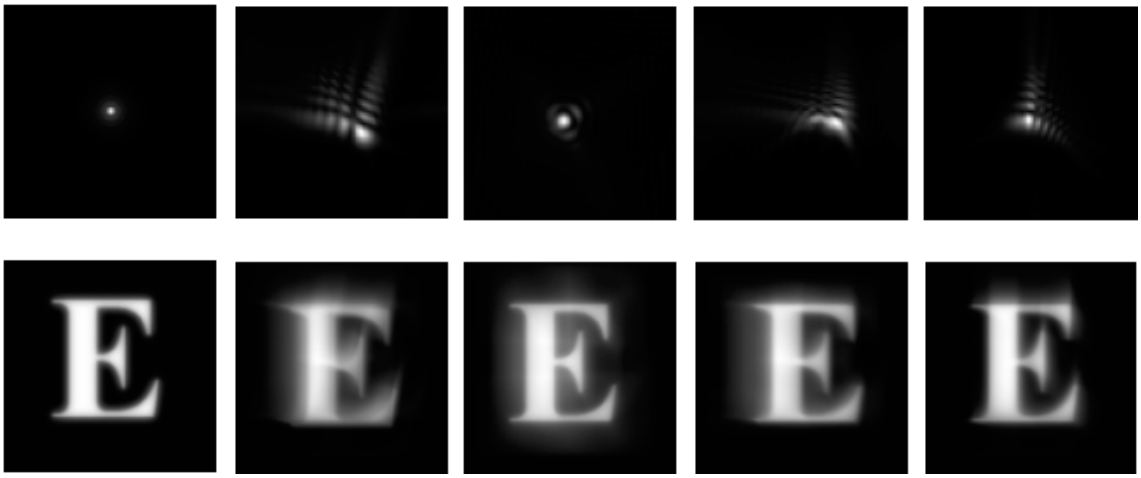

Figure 22 – Comparison of images formed in human eyes with different PSFs. (PORTER, 2003)

It is important to mention that the PSF refers to the optical system quality only from the physical point of view. Therefore, the presented images reflect how the optical system affects the image quality. However, that does not mean that the patient, whose eye presents such PSF, sees the images exactly as shown, since the point spread function does not consider the effects of the cerebral visual processing.

Concerning the influence of each Zernike term to the overall vision quality, it is also important to emphasize that the effects of high-order Zernike terms are not currently well understood. The terms for which these effects are already well known and quantified are mainly defocus and astigmatism, which are called low-order Zernike terms. More recently, spherical aberration, which is in a range of the Zernike modes that could be called mid-order terms, has been shown to negatively affect the vision quality and some of the modern intraocular lenses, for instance, have been designed to be aspherical, i.e., to compensate for the spherical aberration of the cornea. From the other mid-order terms, the coma aberration is the one that appears more frequently in recent studies about aberrometry and vision quality assessment. In general, studies indicate coma can negatively affect the vision quality and its correction through contact or intraocular lenses could represent a benefit to the patient (COX and KINGSTON, 2011). Currently, regarding high-order terms, there are no conclusive studies about their true importance on the vision quality assessment and, therefore, it cannot be stated whether the compensation for these aberrations contributes to an increase or decrease of vision quality.

3. WAVEFRONT SENSORS

A wavefront cannot be perceived, once it is a concept associated with the phase of the electromagnetic wave. That happens because it is light intensity, rather than phase, that interacts with matter. Detectors in general, including the human eye, respond to brightness levels, rather than phase differences (TYSON, 1999).

A wavefront sensor (WFS) is an instrument to measure the wavefront shape. It is responsible for determining the aberration present in the wavefront and mathematically describing it. A generic WFS is comprised of detectors, electronics, a data acquisition system and analysis software.

There are several techniques available to determine the wavefront shape, both quantitatively and qualitatively. Some of these will be briefly and qualitatively presented subsequently. The separation of the presented methods into some different categories is motivated more by didactics than by a classification according to technical aspects.

This work exploits the Hartmann-Shack WFS, which is the most used wavefront sensor worldwide (PLATT and SHACK, 2001). The Hartmann-Shack WFS is based on geometrical optics. However, due to its importance in this scope, it will be treated in chapter 4.

3.1.METHODS BASED ON INTERFEROMETRY

These methods exploit the fact that interference takes place whenever two coherent wavefronts reach the same region in an image plane. The produced pattern is called interferogram or fringe pattern and it represents a two-dimensional intensity distribution profile. Therefore, what is actually measured is light intensity, rather than wave phase; however, interference establishes a direct association between them.

An aberrated wavefront can be identified when it interferes with a reference wavefront. The resultant interferogram constitutes a basic data set, which can be analyzed to extract the information concerning the aberrated wavefront. Direct observation of the fringe pattern provides qualitative assessment of low order aberrations. With computational tools, it is possible to quantitatively describe the aberration through sinusoidal functions.

A limitation of interferometric methods is that it determines the phase profile uniquely only in the range $(0, 2\pi)$, since sinusoidal functions are periodical within this range. Therefore, interferometric methods generally require estimative algorithms to correctly describe the wavefront aberrations (DE LIMA MONTEIRO, 2002).

There are basically two methods of interference: division of wavefront and division of amplitude. The former interferes two, or more, spatially separated parts of the same light beam, as in the point-diffraction interference (PDI) WFS. The latter divides the light beam so that two parts of the beam traverses different paths, as in the Twyman-Green and Mach-Zehnder interferometers (TYSON, 2011).

The PDI WFS is a self-referencing interferometer that divides the amplitude of the light beam to produce a spherical reference wavefront. It consists of a PDI plate, which is a semitransparent disc, with a pinhole in its center. The aberrated wavefront impinges the

PDI plate and the portion of light that goes through the pinhole produces diffraction and, therefore, a spherical wavefront, which is the reference. The other portion of light passes through the plate material with a reduction in intensity, whereas maintaining the initial aberration. Both beams interfere at the observation plane. The principle of operation of the PDI WFS is shown in Figure 23.

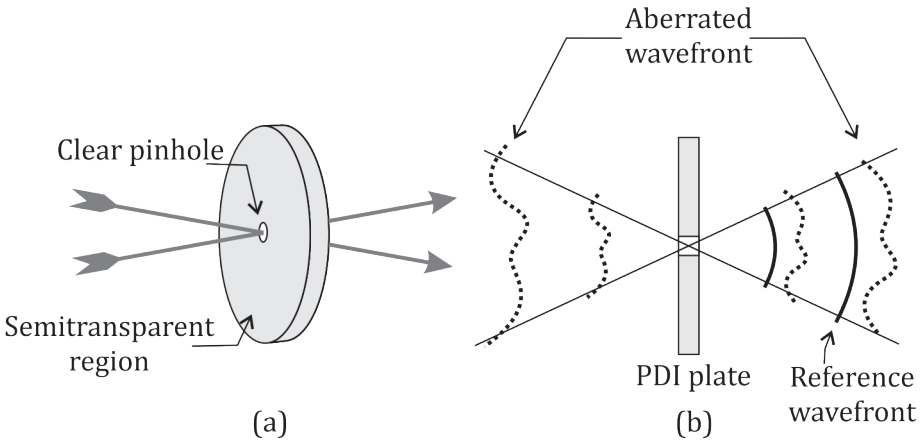

Figure 23 – PDI wavefront sensor: (a) PDI plate and (b) principle of operation.

The Twyman-Green interferometer is based on Michelson interferometer, as it uses a collimated source to form a plane wavefront (TYSON, 2011). In this system, a beam splitter divides the light beam so that part of it goes to the mirror 1 and then back to the interference plane. The other part is transmitted, reaches the mirror 2 and then is reflected by the beam splitter, towards the interference plane. A tilted inclined compensating plate is necessary to equalize the number of times each beam passes through the beam splitter glass. Figure 24 shows the Twyman-Green interferometer being used to test the aberrations introduced in the light beam by reflective and transmissive objects.

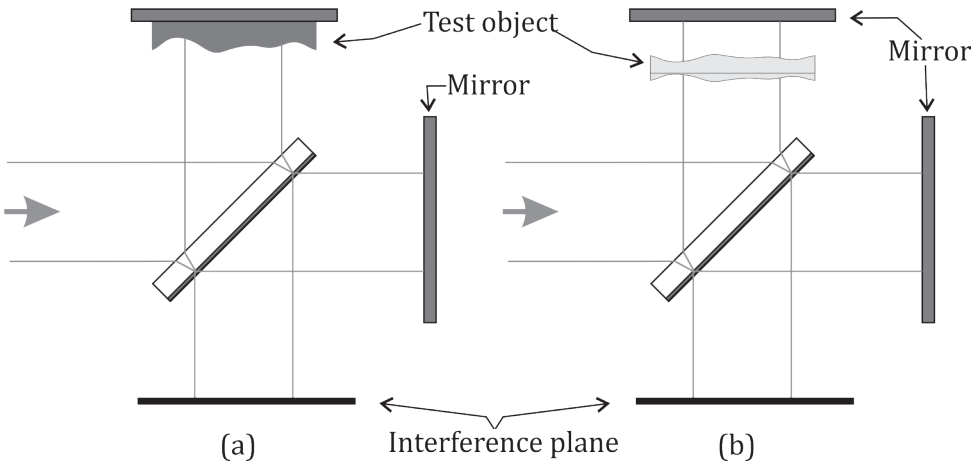

Figure 24 – Twyman-Green interferometer. This setup can be used to test either (a) reflective surfaces or (b) transmissive media.

Note that, when testing transmissive objects, the beam must pass twice through the aberrated medium. This must be taken into account in the calculations, once the measured aberration will correspond to double the real aberration introduced by the object. An

alternative to this setup is the Mach-Zehnder, in which light traverses transmissive objects just once, before reaching the interference plane.

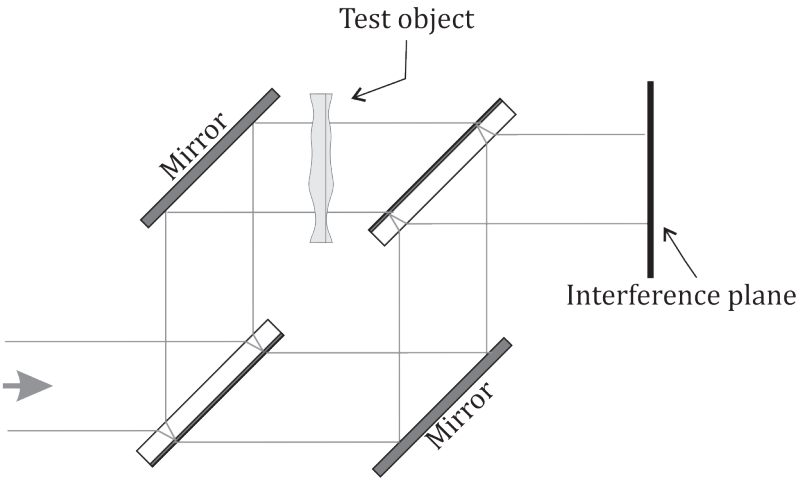

Figure 25 – Mach-Zehnder interferometer.

A modification of the Mach-Zehnder interferometer is the shearing interferometer, which consists in tilting the mirrors around their optical axis. Therefore, the beams produced in each path will not coincide at the interference plane. Instead, their center will be separated by a distance *s*, called shear distance. The resultant fringe pattern is associated to local slopes of the wavefront (MALACARA, 2007). The shearing interferometer is illustrated in Figure 26.

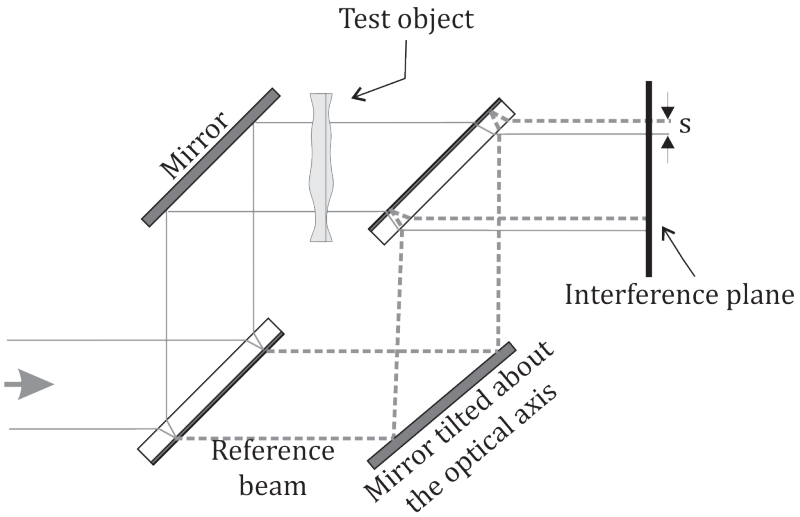

Figure 26 – Shearing interferometer.

3.2.METHODS BASED ON INTENSITY MEASUREMENT

In general, these methods consist in measuring the intensity profile in different fixed places at the propagation path. The profiles change, depending on the aberration present in the light beam. Therefore, the comparison with a reference measurement allows the determination of the aberration initially present in the light beam. Two common methods are phase-retrieval and curvature sensing.

Curvature sensing measures the local second-order derivative of the wavefront (TYSON, 2011). This is done through the irradiance density measurement at two closely separated planes. Figure 27 illustrates the use of curvature sensing to measure the defocus initially present in a light beam. Initially, plane wavefronts impinge a lens and the intensity distribution of the radiant light is measured at planes *A* and *A'*, taken symmetrically with respect to the lens focal point. As the initial wavefronts are plane, both planes are expected to produce the same results. However, if there is some degree of positive defocus in the initial light beam, then the light will converge to a point closer to the lens vertex. Therefore, the irradiance profiles at the two planes are no longer identical. The measured data can be used to solve differential equations that determine the aberration present in the light beam.

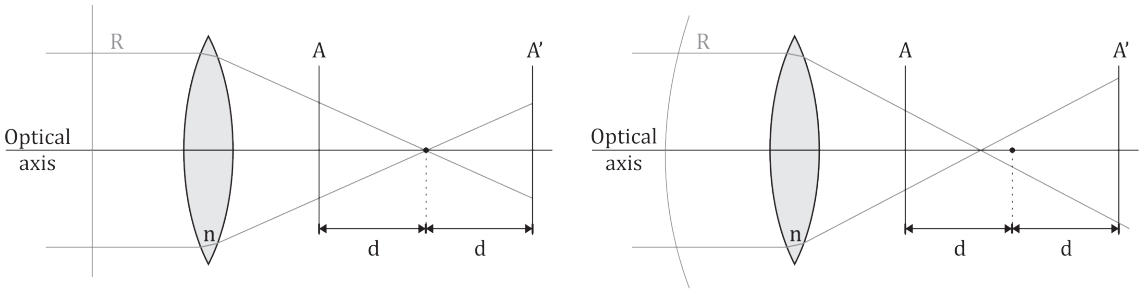

Figure 27 – Curvature sensing method. The reference measurement is shown on the left and the defocused measurement is shown on the right (TYSON, 1999).

The phase retrieval method is an iterative method, which consists in measuring both near and far-field intensity distribution maps to estimate the phase profile. The process begins with a guess of what should be the wavefront shape. The computer compares the expected far-field of the trial aberration to the actually measured. The differences between them, together with the near-field information, are used to compute a new trial aberration to be used in the second iteration. The final result is reached when the difference between the estimated and measured far-fields is minimum. A major problem associated with this technique is the uniqueness of the wavefront aberration found. It may happen that another set of aberration coefficients produces an equally close approximation. Despite this, empirically, phase retrieval produces results in agreement with other wavefront sensing methods (TYSON, 1999).

3.3.METHODS BASED ON GEOMETRICAL OPTICS

The Ronchi test measures aberrations introduced by mirror surfaces using Ronchi ruling, which is a screen with alternating opaque and clear bars. The setup consists in placing the ruling near the center of curvature of a spherical mirror, in front of an imager. The mirror is illuminated and the observed image is a superposition of the mirrored image of the ruling and the ruling itself. These images are called Ronchigrams. The aberrations introduced by the mirror change the shape of the observed image. A quantitative determination of the aberrations can be reached through computational analysis of the Ronchigrams. Figure 28 shows examples of Ronchigrams.

The Ronchi test can actually be rigorously interpreted in terms of diffraction and interference. However, when the spatial frequency of the ruling is not too high, the geometrical approach can also be used with fairly good agreement (MALACARA, 2007).

Figure 28 – Example of Ronchigrams. On left, the mirror introduces spherical aberration and on right, spherical aberration combined with astigmatism (MALACARA, 2007).

The Foucault or knife-edge test is considered a method to determine transversal aberrations and it requires spherical surfaces. Its setup is straightforward and it is simple to extract qualitative information about the aberrations present on a light beam.

Figure 29 (MALACARA, 2007) illustrates the optical setup to test a lens using the knife-edge test. It consists basically in blocking part of a convergent beam at its focus, using a razor blade. The beam is projected onto a screen placed beyond the focal point. When the beam carries no aberration the interception of the blade causes the projected image to change from illuminated to dark. Conversely, when there is aberration, the light rays are not all focused at the same point. Therefore, the interception of the blade generates a pattern on the screen of dark and bright regions, which are due to the blocked and unblocked rays, respectively.

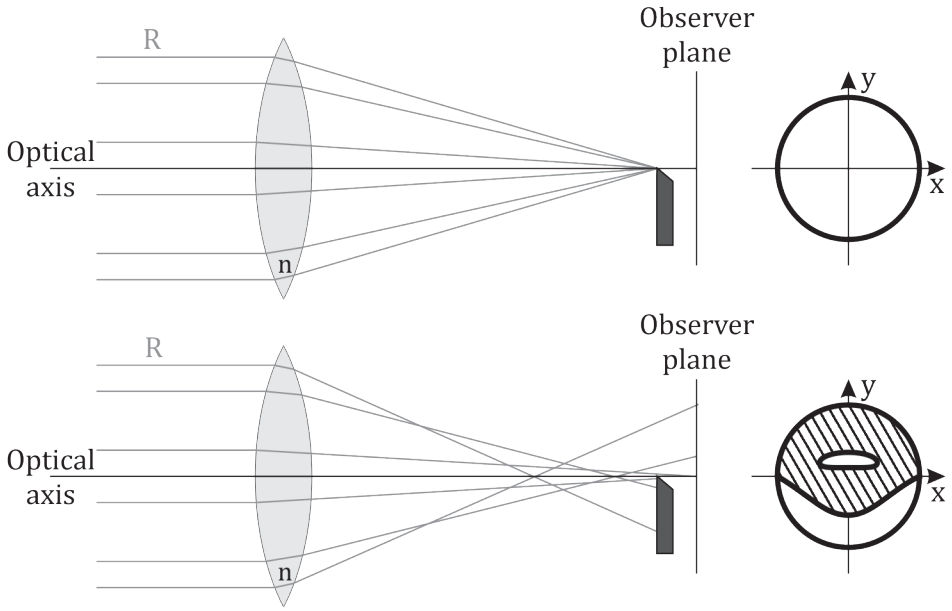

Figure 29 – Foucault or knife-edge setup to test lenses. On top, it is shown an aberration-free lens, whilst, on bottom, a lens with spherical aberration. Shaded regions represent light incidence.

The knife-edge test can also be used to find the focal point of a lens. If the blade is placed on a plane before the focus and is gently moved toward the optical axis, the shadow

observed at the screen moves at the opposite direction. Conversely, if the blade is placed beyond focus, the shadow moves in the same direction as the blade. When placed exactly on the focal point, the movement of the blade toward the optical axis causes a sudden change of bright to dark in the observed image (TYSON, 2011).

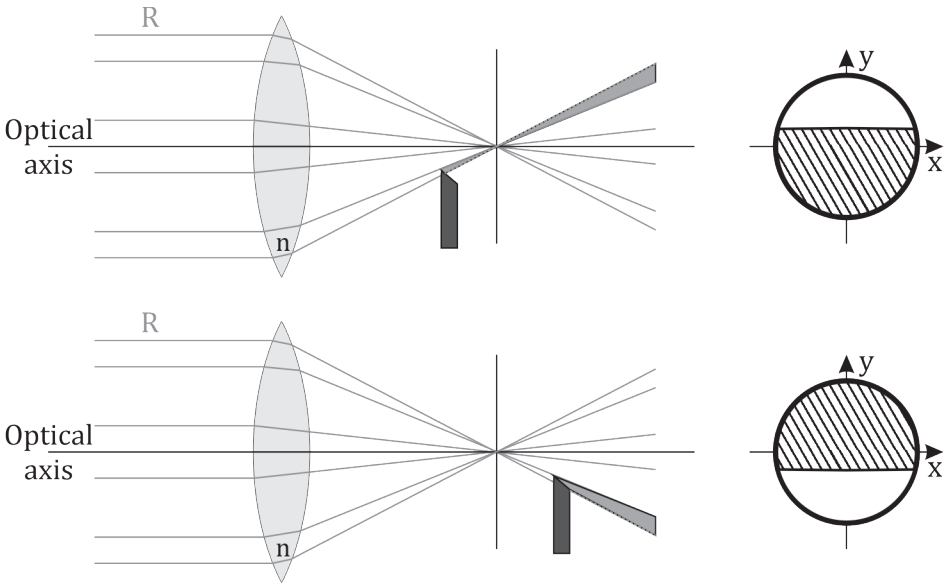

Figure 30 – Focus sensing with the knife-edge test of an aberration-free lens. Shaded regions represent light incidence.

The pyramidal wavefront sensor uses a quadrangular-pyramid prism to sample the light beam into four distinct light spots, which are projected on a detector, as illustrated. The positions in which the spots impinge on the detector change according to the aberration present in the test beam. Through the intensity measurements provided by the detector, each light spot position can be calculated. The positions of the light spots, together with their respective intensity distribution, are mathematically related to the aberration present in the light beam (TYSON, 2011).

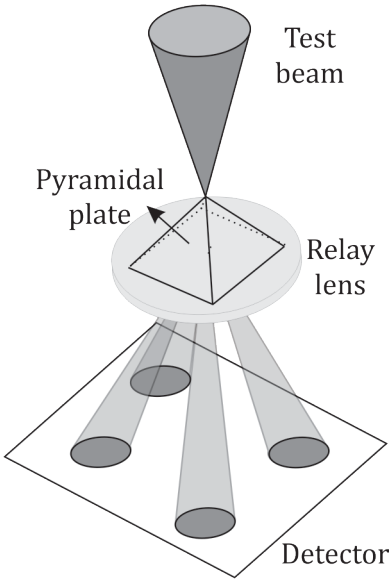

Figure 31 – Pyramidal method.

The Hartmann test was invented in the beginning of the XX century (MALACARA-DOBLADO and GHOZEIL, 2007) and uses a mask with a set of holes to test mirrors or lenses. The mask is called Hartmann screen and is illuminated by the light beam to be tested. The beam produces a pattern of light spots at the observer plane placed beyond the mask, which is called a hartmogram, as illustrated in Figure 32.

If the beam carries no aberration, the produced hartmogram can be used as a reference. Once the aberrations are present, they cause the light spots to move from the reference positions. The obtained displacements are an indirect measure of the wavefront local slopes. Therefore, they can be used to calculate the optical phase difference and, hence, to estimate the wavefront shape.

A variation of the Hartmann test is the Hartmann-Shack (H-S) wavefront sensor, also referred to as Shack-Hartmann WFS. The difference is that the H-S sensor uses microlenses instead of holes. That contributes to larger signal-to-noise ratio and greater accuracy in the determination of light-spot centroid positions, since the light energy is concentrated in a smaller spot. The Hartmann-Shack wavefront sensor is the one used in this work and will be treated in detail in the next chapter.

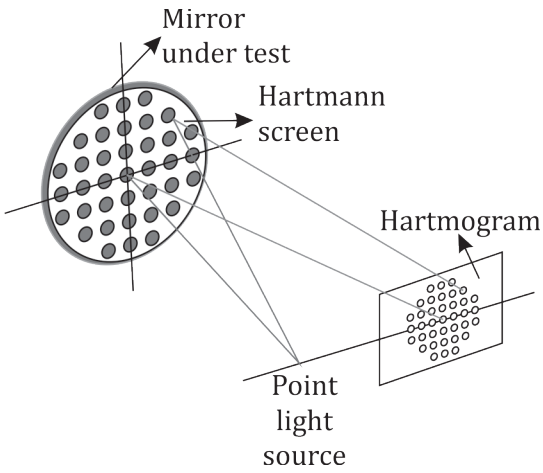

Figure 32 – Hartmann test of a mirror.

The last method described here is called Laser Ray Tracing, or simply LRT and is illustrated in Figure 33. The LRT is essentially very similar to the Hartmann test. The only difference is that, instead of a mask with holes or lenses, there is a single collimated thin laser beam, which sequentially impinges on the test object at several different predetermined points. Usually a moving mirror performs the laser scanning. At each point, the laser light traverses and reaches the detector plane, thus forming a set of reference positions. The total number of points, as well as each point position, is determined according to application requirements (NAVARRO and MORENO-BARRIUSO, 1999). The analysis of the result is done similarly to the Hartmann test. Initially, the LRT is carried out without any object test. In this case, the reference positions of the light spots are recorded at the detector plane. With the test object in place, the spot positions are again recorded and then compared to the reference ones. The set of deviations of the measured spots in relation to the reference ones is then used to reconstruct the wavefront surface in the same manner as in the Hartmann test.

LRT allows the sampling of the wavefront to be performed in a pattern comprised of as many points as necessary and with arbitrary position distribution. However the method requires moving parts. The mechanics involved is likely to contribute with a decrease in the precision with which the points are spatially determined, which affects repeatability. Moreover, the scanning process requires a longer time to run and generate the hartmogram, in comparison with the Hartmann-Shack method, which generates all the light spots of the hartmogram at a single shot.

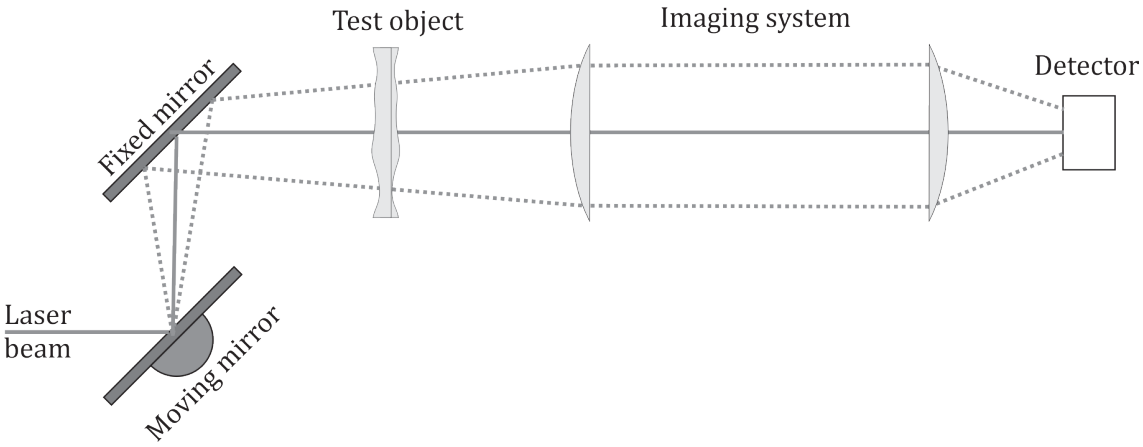

Figure 33 – Laser Ray Tracing schematics (NAVARRO and MORENO-BARRIUSO, 1999).

4. THE HARTMANN-SHACK WAVEFRONT SENSOR

The Hartmann-Shack WFS was developed in the late 1960s and early 1970s as an attempt to improve the images of satellites taken from earth. The strategy consisted in monitoring the wavefront error introduced by the atmosphere, using the H-S sensor, while controlling the exposure time to take the images. Images could only be taken if the wavefront error did not change more than $\lambda/10$ (PLATT and SHACK, 2001).

Initially, the Hartmann test was used to measure the aberrations introduced by the atmosphere. However, it presented two major difficulties: the light spots had low intensity and the measurement of the light-spot centroid was inaccurate. It is important to emphasize here that the hartmograms were analyzed using photographic plates, since the charged-couple devices (CCD) cameras appeared only in the 1980s (MANSURIPUR, 1999). To solve these problems, Dr. Roland Shack (PLATT and SHACK, 2001) proposed substituting the holes in the Hartmann mask by lenses, which would concentrate all the impinging light on a smaller spot, hence, providing a larger signal-to-noise ratio at the same time as an improvement in the accuracy of the centroid-position measurement.

The use of lenses also allowed the construction of masks with larger fill-factor[8], since the lenses could even be contiguous. A larger fill-factor allows more light energy to be collected by the mask, contributing, therefore, to the increase in the spot intensity (SHACK and PLATT, 1971).

A great advantage of the H-S sensor over interferometric method is that it does not require reference beam[9], which is not always readily available in the optical setup (MANSURIPUR, 1999). Besides, it is simpler to align and operate. It is also less sensitive to vibration, particularly because it does not use any movable components, and does not require the light beam to be monochromatic.

Since then, the H-S WFS has been used in many different applications such as ophthalmological aberrometry, adaptive optics, quality laser beam measurement, optics testing, and optical system alignment (NEAL, COPLAND and NEAL, 2002).

4.1. DESCRIPTION OF THE METHOD

The principle of the Hartmann-Shack wavefront sensor is based on geometrical optics. It measures the wavefront local slopes, rather than the optical phase difference, as in the interferometric methods. Actually, it measures the transverse aberrations at a fixed plane and these are closely related to the wavefront slopes.

It is composed of a microlens array and a 2D detector, which can be a camera or an array of optical position-sensitive detectors (PSDs). The microlenses that compose the array have all the same focal length, and are assembled in the system so that the detector plane coincides with the focal plane.

[8] Fill-factor is the ratio between the area occupied by the lenses and the total area of the sampling plane.

[9] Nevertheless, a reference beam may also be used so that the aberrations introduced by elements other than the test object are not taken into account.

To understand the principle behind the Hartmann-Shack wavefront sensor, consider a 1D case. Figure 34 illustrates the microlens array and the detector assembled together.

When an incoming wavefront reaches the microlens array, it is sampled into light spots that are projected on the focal plane. Considering the incoming wavefront is plane (which is taken here as the reference wavefront, for simplicity), each light-spot centroid position will coincide with the optical axis projection of the corresponding lens (see Figure 34a). Because the local vector normal to the wavefront corresponds to the propagation direction of the electrical field, an aberrated wavefront will cause the light spots to deviate from the reference position as shown in Figure 34b. That is the key principle of the H-S sensor, i.e., the light-spot centroid position is directly related to the wavefront slope averaged over the respective lens area (NEAL, COPLAND and NEAL, 2002).

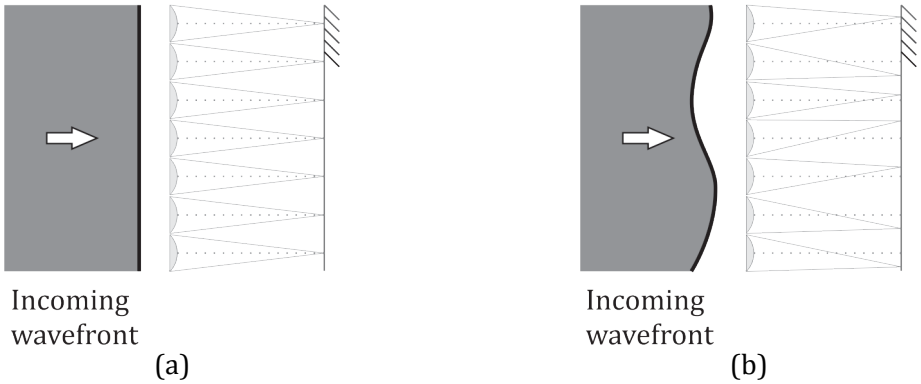

Figure 34 – 1D schematics of the Hartmann-Shack principle (a: plane wavefront, b: arbitrary wavefront).

The detector, which is placed on the focal plane of the microlenses, is responsible for generating data that allows the determination of spot-centroid positions. These data is passed to a control unit, which can be a computer or an embedded system.

If a camera is used, it produces an image of light spots, as shown in Figure 35. The control unit then, in a first step, processes the image to identify the light spots and to calculate its centroids positions. Otherwise, if an array of PSDs is used, the output signals are already directly proportional to the spot centroid position and the first step of the control unit consists only in converting these signals to position data.

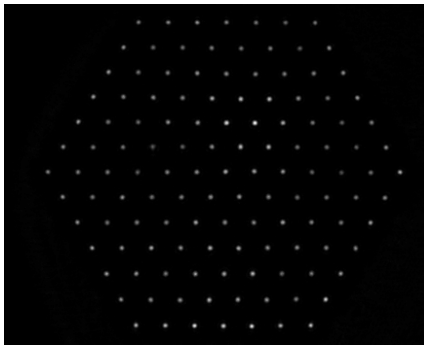

Figure 35 – Example of a hartmogram obtained in the OptMA[lab][10] using a camera and a commercial 127-microlenses hexagonal array.

[10] OptMA[lab] is the acronym for "Laboratório para Optrônica e Microtecnologias Aplicadas".

The next steps executed by the control unit depend on the application. In those cases where the main objective is to correct the wavefront error using an optical active element, such as a deformable mirror, the information regarding the wavefront shape function may not be necessary and then the control unit can be designed to directly actuate the adaptive element. Otherwise, in those cases where the wavefront must be mathematically identified, such as in ophthalmic aberrometry, the control unit must run a wavefront-reconstruction algorithm.

4.2.DETECTOR

There are basically two systems typically used as detectors in the H-S sensor: the camera and the position-sensitive photodetector (PSD) array.

Figure 36 shows an example of image analysis of a hartmogram. These pictures were produced with an algorithm built in OptMA[lab]/UFMG to run on an embedded system based on a Digital Signal Processor (DSP). The image-processing algorithm comprises pre-processing, identification of light spots, calculation of the centroid coordinate of each light spot and conversion of the position values from pixel[11] units to the chosen unit for the wavefront reconstruction algorithm. In the sequence, letter (a) shows an arbitrary hartmogram, which is taken as the test image; letter (b) shows a binary image (in the sense that it contains only two colors), obtained in an image thresholding procedure[12] (RUSS, 2007) during the step to identify the light spots; and letter (c) shows the final result, in which the light-spot centroids had their coordinates identified and represented in the image as a small black cross in the middle of a white square box.

As illustrated by Figure 36, the use of cameras in the H-S sensor requires a process capable of storing the image of the spots and calculating the spot deviations based on image analysis of both reference and test images. The chief disadvantage of using such cameras is that this process often takes too long for real-time purposes.

The PSD array is an alternative to improve the performance of H-S sensors. Is consists of a 2-dimensional array of position-sensitive photodiodes in such a geometry that each photodiode is directly associated with one microlens of the mask. There are several different approaches to build the PSDs, such as: lateral-photoeffect photodiode (LEP), chessboard-like PSDs, spiral PSD and quad-cells (DE LIMA MONTEIRO, 2002).

[11] Pixel is the smallest element of a digital image. Its value is associated with the light intensity on it.
[12] Thresholding, also called binarization, is a process to convert a 256-gray levels image into black and white.

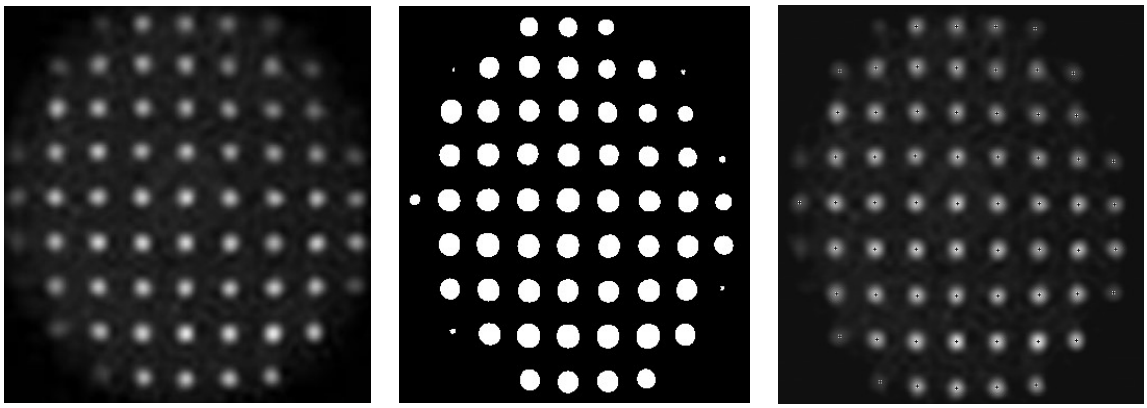

(a) (b) (c)

Figure 36 – Example of image analysis of a hartmogram to determine the spot-centroid position: (a) hartmogram, (b) binary image and (c) spots marked with a cross.

The great advantage of these sensors, in one hand, is that they provide an output signal, which is directly proportional to the displacement of the light spot. Therefore, all the process of acquiring, storing and analyzing images is not required by the PSD array. On the other hand, the geometry of PSD array determines the design of the microlens array, and vice-versa, once there is a one-to-one association between photodetector and microlens. That also imposes other limitations such as light-spot size and displacement range (DE LIMA MONTEIRO, 2002; SALLES and DE LIMA MONTEIRO, 2010).

4.3. WAVEFRONT RECONSTRUCTION

For each light spot, the deviation from the reference position is proportional to the mean wavefront tilt in the respective lens. This relation between deviation and mean wavefront local tilt is shown graphically in Figure 37 and is written in equation 8.

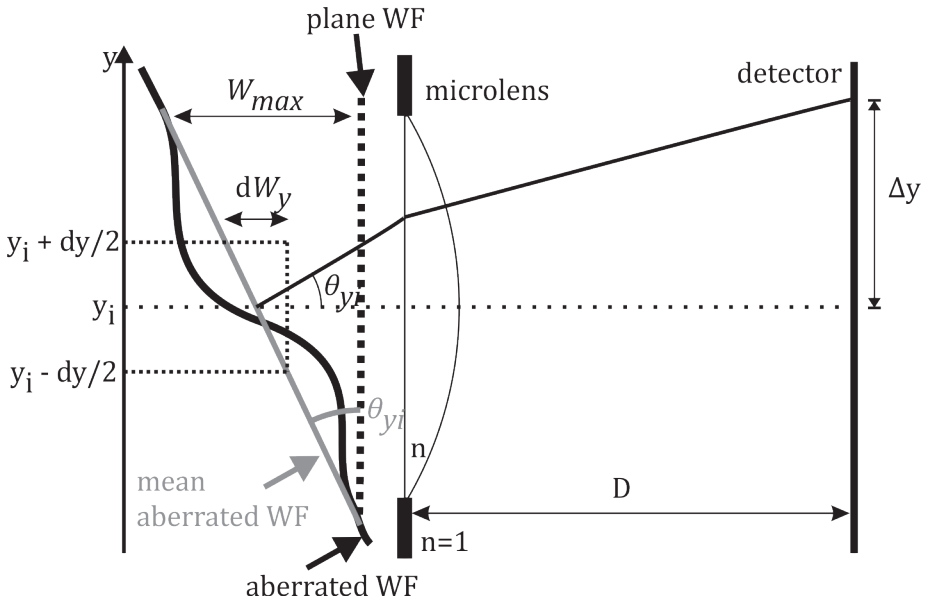

Figure 37 – Relation between the local wavefront (WF) aberration W and the ray deviation.

$$S_x = \tan\theta_{x_i} = \left.\frac{dW_x}{dx}\right|_{(x_i,y_i)} \cong \frac{\Delta x}{D}; \quad S_y = \tan\theta_{y_i} = \left.\frac{dW_y}{dy}\right|_{(x_i,y_i)} \cong \frac{\Delta y}{D} \qquad 8$$

The approximation in equation 8 is because the change in the propagation direction caused by the lens is not being taken into account in the equation, for simplicity. In practice, a corrector factor that depends both on θ and n appears multiplying Δx and Δy. See section 6.1.2 for a more complete rigorous treatment of the lens influence on the deviation measurement.

The set of light-spot deviations enables the reconstruction of the wavefront aberration through a mathematical model. Describing a wavefront aberration quantitatively means writing it in the form of equation 3. However, in practice the infinite series is unfeasible and the summation has to be truncated in the n^{th} term, as follows:

$$W(x,y) = \sum_{j=0}^{n-1} C_j Z_j(x,y) \qquad 9$$

where the $Z_i(x,y)$ terms are the Zernike polynomials, which form purposefully and conveniently an orthonormal basis. Then, in other words, describing mathematically a wavefront aberration means determining the coefficients C_i.

In this sense, equation 8 can be rewritten as:

$$S_{x_i} = \left.\frac{dW_x}{dx}\right|_{(x_i,y_i)} = \sum_{j=0}^{n-1} C_j \left.\frac{dZ_j}{dx}\right|_{(x_i,y_i)}; \quad S_{y_i} = \left.\frac{dW_y}{dy}\right|_{(x_i,y_i)} = \sum_{j=0}^{n-1} C_j \left.\frac{dZ_j}{dy}\right|_{(x_i,y_i)} \qquad 10$$

where the local tilts S_{x_i}andS_{y_i} refer to the center (x_i, y_i) of the i^{th} lenslet and n is the total number of Zernike terms. Equation 10 stands for one microlens. Considering the set of equations for all the N lenslets, the problem can then be rewritten in the matrix form:

$$\begin{pmatrix} S_{x_0} \\ S_{y_0} \\ \vdots \\ S_{x_{N-1}} \\ S_{y_{N-1}} \end{pmatrix} = \begin{pmatrix} \left.\frac{dZ_0}{dx}\right|_{(x_0,y_0)} & \cdots & \left.\frac{dZ_{n-1}}{dx}\right|_{(x_0,y_0)} \\ \left.\frac{dZ_0}{dy}\right|_{(x_0,y_0)} & \cdots & \left.\frac{dZ_{n-1}}{dy}\right|_{(x_0,y_0)} \\ \vdots & \ddots & \vdots \\ \left.\frac{dZ_0}{dx}\right|_{(x_{N-1},y_{N-1})} & \cdots & \left.\frac{dZ_{n-1}}{dx}\right|_{(x_{N-1},y_{N-1})} \\ \left.\frac{dZ_0}{dy}\right|_{(x_{N-1},y_{N-1})} & \cdots & \left.\frac{dZ_{n-1}}{dx}\right|_{(x_{N-1},y_{N-1})} \end{pmatrix} \cdot \begin{pmatrix} C_0 \\ C_1 \\ \vdots \\ C_{n-2} \\ C_{n-1} \end{pmatrix} \qquad 11$$

Equation 11 can be written as follows:

$$\boldsymbol{S} = \boldsymbol{B} \cdot \boldsymbol{C} \qquad 12$$

where $\boldsymbol{S}$ contains the local x- and y-tilts for each of the N lenslets (i.e., $2N$ elements), $\boldsymbol{B}$ is the matrix of the Zernike terms derivatives ($2N \times n$ elements) and $\boldsymbol{C}$ is the matrix of the Zernike coefficients (n elements), which is the desired solution of the equation.

When the matrix $\boldsymbol{B}$ is square; i.e., the number of microlenses is equal to half the number of Zernike terms; the calculation is direct. However, in most cases, $2N > n$ and therefore matrix $\boldsymbol{B}$ is not square, since a large number of microlenses is desirable to guarantee lower sampling errors and then it must be solved through least-squares minimization, in which the coefficients are found with the smallest error possible. Implementing the least-

squares minimization method numerically is equivalent to solving the equation (CUBALCHINI, 1979)

$$\boldsymbol{B}^T\boldsymbol{S} = [\boldsymbol{B}^T\boldsymbol{B}]\boldsymbol{C} \qquad 13$$

where $\boldsymbol{B}^T$ is the transpose of $\boldsymbol{B}$.

The solution of this equation requires the computation of the so-called Moore-Penrose pseudoinverse of $\boldsymbol{B}$ (equation 14).

$$\boldsymbol{A} = (\boldsymbol{B}^T\boldsymbol{B})^{-1}\boldsymbol{B}^T \qquad 14$$

Matrix $\boldsymbol{A}$ will be henceforth referred to as the estimation matrix. Therefore, finding matrix $\boldsymbol{C}$ reduces to solving the set of equations represented by equation 15.

$$\boldsymbol{C} = (\boldsymbol{B}^T\boldsymbol{B})^{-1}\boldsymbol{B}^T\boldsymbol{S} \qquad 15$$

When the 2D detector is a camera, the output of the sensor is an image of the light spots, which has to be processed by the control system in order to determine the centroid positions; then the deviation of each light spot needs to be estimated before reconstructing the wavefront aberration.

Another possibility is when the focal plane comprises an array of position-sensitive detectors, which can measure the x and y coordinates of light-spot centroids. In this case, each optical detector is associated to a microlens and therefore is responsible for measuring the position of the correspondent light spot. The output of each optical position detector is an analog signal proportional to the light spot deviation. These signals are then converted to digital signals, which are read and interpreted by the control system, before reconstructing the wavefront.

Once the Hartmann-Shack method is based on spatially sampling the wavefront, it is likely that errors related to the sampling process will be present. In general, these errors are closely related to the microlens array geometric parameters, such as the grid pitch, lens diameter and array geometric shape. The error also depends on the number of spatial modes, namely Zernike terms, necessary to describe the wavefront aberration.

4.4.MICROLENS ARRAY

The development of a microlens array was motivated by a problem posed by the US Air Force (PLATT and SHACK, 2001) in the late 1960s. They demanded a solution to improve the quality of images of satellites taken from Earth. The proposed idea consisted, in general terms, in controlling the exposure time of the images according to the change of the aberrations introduced by the atmosphere. The Hartmann test was initially proposed to measure these aberrations. However, two basic problems were present: inaccuracy in the light-spot centroid position and low light intensity on the detector plane. That was particularly important because the exposure time was found to be very short and, therefore, the light energy available to impress a photographic plate[13] was low.

[13] The CCD and CMOS detectors were commercially available only in the 1980s. Then, before this, both the Hartmann and Hartmann-Shack methods were carried out with photographic plates, where the hartmograms were recorded (MANSURIPUR, 1999).

According to Platt and Shack (2001), Dr. Roland Shack was the one who proposed the idea of using lenses in the place of holes, in the mask of the Hartmann test, to try to solve the mentioned problems. With microlenses in the place of holes, more light energy is directed to a smaller region and, therefore, the light spots are smaller and brighter. Currently, the H-S sensor is the most widely used WFS technology (GREENAWAY and BURNETT, 2004).

4.4.1. FABRICATION OF THE MICROLENS ARRAY

A difficulty in implementing Shack's idea was the fabrication of such microlens arrays. The lenses were required to have diameter of 1 mm and focal length of 100 to 150 mm and no one was found to fabricate them at that time.

The first microlens array, fabricated by Dr. Platt (PLATT and SHACK, 2001), consisted of cross-cylindrical lenses. Two molds with parallel grooves, such as the one shown in Figure 38, were used perpendicularly to each other. An acrylic sheet was then placed between both molds and the set was heated so that the pattern of the molds was transferred to the acrylic sheet. The first fabricated array contained 250 microlenses in a regular grid, each with area of 1 mm^2 and focal length of 150 mm (MANSURIPUR, 1999). As the lenses were contiguous, the fill factor[14] was 100%.

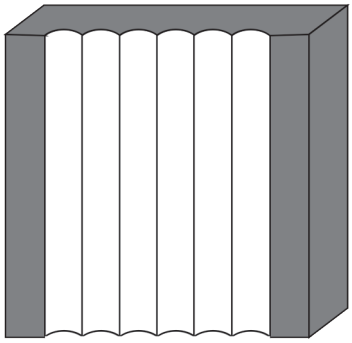

Figure 38 – A piece of the mold used in the production of the first microlens array for the H-S sensor.

Current microlens arrays contain from tens to thousands of microlenses with diameter in the approximate range of 0.2 to 2 mm. The advent and development of microfabrication techniques contributed to the diversification of the arrays characteristics, including geometry. Common commercial arrays are either hexagonal or.

A common technique used to fabricate microlens arrays is thermal reflow (LIN, YANG and CHAO, 2003), which was initially proposed by Popovic *et.al.* (1988). It is a method fully compatible with integrated circuits (IC) fabrication and, despite its simplicity, provides microlenses of excellent quality (POPOVIC, SPRAGUE and CONNELL, 1988). Several variations of this technique have been proposed since then to match the requirements of specific applications (LIN, YANG and CHAO, 2003).

[14] Fill factor is the ratio of the area occupied by lenses to the total array area.

Thermal reflow consists basically in forming cylindrical posts of photoresist[15] using standard photolithography[16] and then melting them onto a substrate. Surface tension effects on the photoresist surface provide the hemispherical shape of the lenses (DALY, STEVENS, *et al.*, 1990). The process is illustrated in Figure 39. In the sequence, the photoresist layer is exposed to light through a mask. The exposed regions become soluble and are removed by the photoresist developer. The set is then heated and the remaining unexposed regions of photoresist are melted until they form hemispherical shapes.

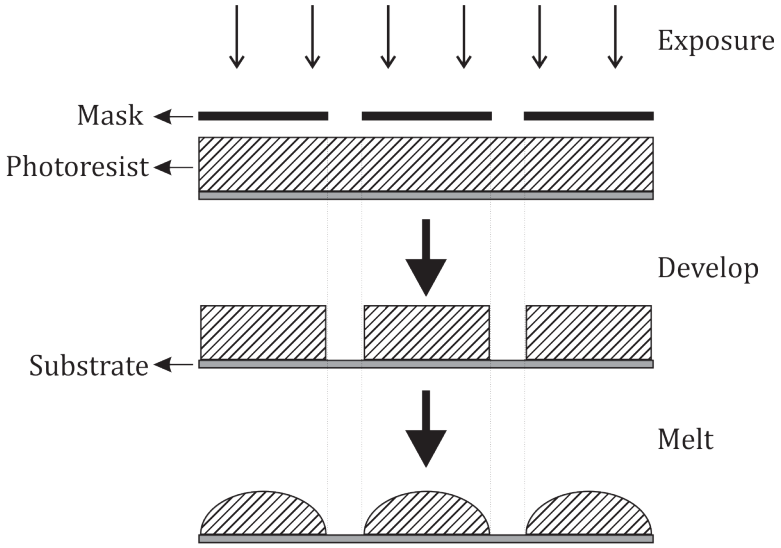

Figure 39 – Illustration of the thermal reflow process to build microlens arrays (DALY, STEVENS, et al.*, 1990).*

Using this technique, Popovic *et al.* (1988) built arrays of microlenses with diameters as small as 30 μm.

Several other different techniques were proposed to fabricate microlens arrays, such as ink-jet processes (BIEHL, DANZEBRINK, *et al.*, 1998), hot embossing (PAN, WU, *et al.*, 2008; ONG, KOH and FU, 2002), lithography (KUNNAVAKKAM, HOULIHAN, *et al.*, 2003), laser machining (ZIMMER, HIRSCH and BIGL, 1996), precision diamond grinding (BORRELLI, 1999) and precision glass molding (HUANG, HSIAO, *et al.*, 2011). Each has its advantages and specificities regarding the required technology. The appropriate technique must be chosen taking into account the specific application of the microlens array, its characteristics and the available technology. A detailed description of some common fabrication methods can be found in Borrelli (1999).

The fabrication technique used in this work was initially discovered and evaluated by Kendall *et al.* (1994) and later proposed by De Lima Monteiro *et al.* (2005) for use in wavefront sensors. This method consists in building a mold in silicon using anisotropic

[15] Photoresist is a light-sensitive material. When exposed to light it becomes soluble or insoluble (depending on the specific material) to the photoresist developer, which is a substance used to remove the photoresist from the substrate. It is used mainly to form patterns on the substrate surface.

[16] Photolithography is the process in which patterns are transferred to the photoresist through a mask. The mask contains the pattern and is placed above the photoresist layer. After light exposure, those regions that became soluble to the photoresist developer can be removed while the regions that were insoluble continue in the substrate, forming the desired pattern.

KOH (potassium hydroxide) etching and then replicating the array using a UV-curing polymer. It is a flexible technique that also enables the fabrication of aspherical optical surfaces (DE LIMA MONTEIRO, AKHZAR-MEHR, *et al.*, 2003).

The mold fabrication consists in a bulk-micromachining process and exploits the fact that KOH etches silicon in an anisotropic way, i.e. the etching rate depends on the crystalline plane[17] exposed to the solvent. Consider a silicon wafer, placed horizontally, with (100) orientation. That means that the crystalline plane with Miller index (100) is oriented upwards and the (111) plane forms an angle of 54,74°[18] with the horizontal. Suppose that the entire silicon surface is protected with SiO_2 (silicon dioxide), except for a small arbitrary region, in which the SiO_2 is etched by hydrofluoric acid (HF). When in contact to a solvent, it etches only the unprotected area. The plane (100) starts being etched and exposes the (111) plane, which is also etched, but at a slower rate. The final result is an inverted pyramid, such as illustrated in Figure 40. Depending on the etching time, the formed pyramid may be complete or truncated.

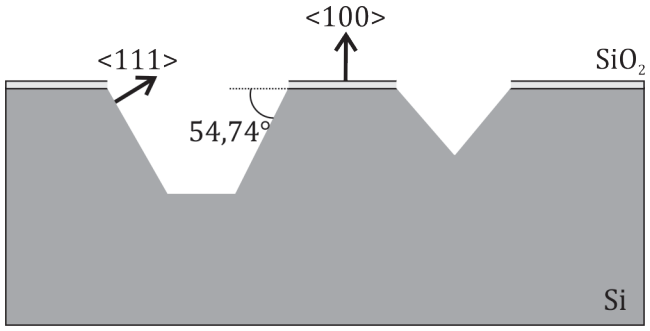

Figure 40 – Bulk micromachining of silicon.

An interesting effect happens when a silicon wafer, with some inverted pyramidal structure, is submitted to KOH etching without the protection of the SiO_2. The corner of the pyramid is etched and then it exposes another crystalline plane, the (411), which is etched faster than (111) and (100) planes. The successive etching of the crystalline planes evolves into a nearly spherical cavity. For a given KOH concentration, the final diameter D of the spherical cavity depends on the initial pyramid base size (d_0) and on the etching time (DE LIMA MONTEIRO, AKHZAR-MEHR and VDOVIN, 2005).

[17] A crystalline structure is formed by a specific arrangement of atoms or molecules. A set of these elements, arranged in a certain way, comprises a pattern, which is repeated periodically all over the material. The position of each atom or molecule constitutes a point of the lattice. A plane containing different lattice points is a crystalline plane. These planes are identified by Miller indices, which form a set of three numbers, written within parenthesis, that identifies the plane. If the numbers are written within chevrons, they identify the vector perpendicular to the plane. A complete explanation is found in Ashcroft and Mermin (1976).

[18] This angle is determined by the silicon crystalline structure.

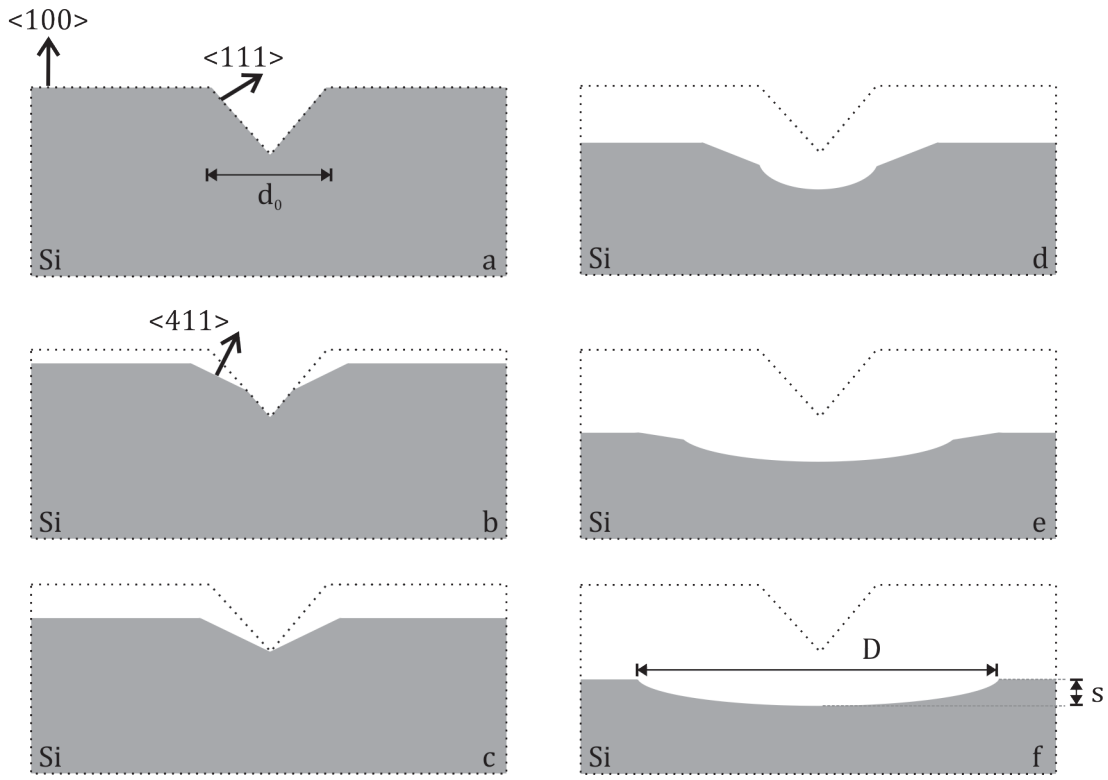

Figure 41 – Spherical shape formed by anisotropic KOH etching of silicon (DE LIMA MONTEIRO, AKHZAR-MEHR, et al.*, 2003).*

The cavity diameter D and sagitta s can be project appropriately so that it constitutes a mold for the desired microlens. The values of D, d_0 and h, which is the etching depth are related through equation 16 (OLIVEIRA COSTA, 2010).

$$h = d_0 \cdot \left(\frac{D}{7.8 \cdot d_0}\right)^{1/0.58} \qquad 16$$

Several inverted pyramidal openings can be built along the silicon wafer surface. From each pyramid, a rounded cavity is formed. The final result is then the microlens array mold. Note that the cavities to mold all lenses of the array are formed simultaneously during this etching process step.

An important aspect of this fabrication technique is that it does not limit the microlens-array geometry. The distribution pattern of the microlenses in the array is determined basically by the position of the inverted pyramids, which, incidentally, are set with high precision, by means of lithography.

4.4.2. MICROLENS-ARRAY GEOMETRY

Soloviev and Vdovin (2005) have discussed about the influence of the geometry of a Hartmann-Shack microlens array on the wavefront reconstruction error, which indicates the accuracy with which the reconstructed wavefront matches the exact shape of the original one. They propose the use of a randomized array geometry, which doubles the number of correctly reconstructed Zernike modes, adding no additional computation time and providing a smaller reconstruction error. That was verified in the article for up to 40 modes.

In their paper, Soloviev and Vdovin (2005) propose a general mathematical model to describe the modal wavefront reconstruction, depending neither on the choice of the basis functions nor on the statistics used to describe the wavefront. This model demonstrates the mathematical dependency of the reconstruction error on the array geometry.

Using the frequency domain, they propose an expression that describes how the array samples a wavefront in terms of size and position of the microlenses. Due to finite size, the microlenses act as a low-pass filter, since it senses high-frequency terms as low frequency ones (aliasing). Besides, medium- to high-frequency terms, which are properly sampled frequency-wise, are presented with attenuated amplitude, being the attenuation proportional to the size of the microlens. In their paper, the influence of the array geometry is discussed in terms of the Fourier spectrum of the microlens arrays. Random and regular arrays also present different frequency spectra, as can be seen in Figure 42. The regular spectrum results in significant aliasing. Refer to Soloviev and Vdovin (2005) for a detailed description.

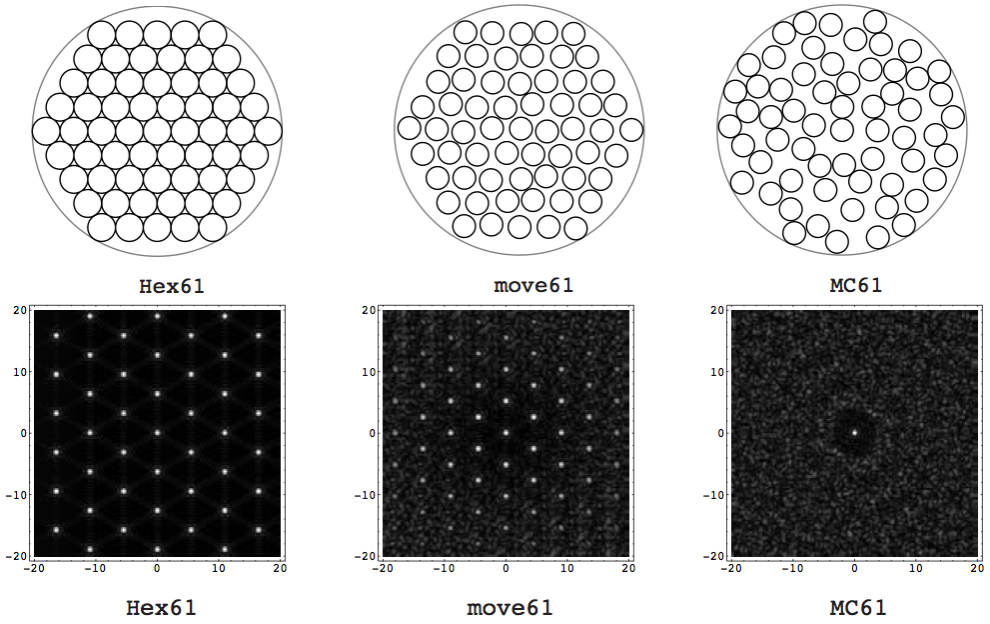

Figure 42 – Frequency spectrum of different microlens arrays. 'Hex61' stands for regular hexagonal array; 'move61', for hexagonal with small random displacements in the center position of each microlens; and 'MC61' stands for random array generated by Monte Carlo simulation. All masks contain 61 microlenses (SOLOVIEV and VDOVIN, 2005).

Soloviev and Vdovin have carried out numerical tests with microlens arrays of different geometries and compared the reconstruction error in each case, using Zernike polynomials with coefficients generated by a statistics for the description of the atmospheric turbulence (NOLL, 1976). Arrays with randomly distributed microlens centers generated better results than the regular ones, especially when the number of Zernike terms increased to more than 40, situation in which the regular arrays experience a catastrophic growth of the aliasing error.

They have also demonstrated that the optimal number of Zernike terms that can be correctly reconstructed by the Hartmann-Shack method is always less, or of the same

order, than the number of microlens (WANG and SILVA, 1980). Moreover, they have shown that it is possible to increase the number of Zernike terms, maintaining the same reconstruction error, just by randomizing the microlens positions.

Navarro, Arines and Rivera (2009) also worked on the comparison of performance of arrays with different distribution patterns of microlenses. Their results corroborate with the ones of Soloviev and Vdovin (2005).

Since it has been demonstrated that random arrays can generate smaller reconstruction errors than regular ones, two interesting questions can be formulated:

a) Given a certain statistics describing the wavefront aberrations in some context, is it possible to specify the best microlens array geometry, i.e., the one that will generate the smallest reconstruction errors? This would allow the production of more precise equipment based on Hartmann-Shack method.
b) Considering this statistics, is it possible to reduce the number of microlenses in the array, while maintaining the same reconstruction error, just by changing the array geometry? This would represent a benefit, for instance, for real-time systems, in which the processing time of measured data is a critical parameter, because less microlenses would generate also less data to be processed.

These two questions can be summarized by the problem of finding an optimal microlens array geometry for a given application, such as ophthalmology or astronomy. By geometry, it is meant distribution pattern of microlenses and also number of microlenses in the array. Hereinafter, the problem of finding an optimal microlens array geometry will be referred to as optimization of the microlens array.

The optimization of the microlens array was also suggested in the work of Diaz-Santana, Walker and X-Bará (2005), which presents a mathematical model to compare the performance of arrays with different geometries. Their model requires input information such as array parameters, statistics of the wavefront aberrations and sensor noise. They applied their mathematical model to different array geometries considering an aberration statistics of human eyes, as a case study. They studied square, hexagonal and different polar geometries and concluded that polar patterns produced smaller reconstruction errors. However, Diaz-Santana, Walker and X-Bará did not test any random pattern. They propose that the problem of optimizing the microlens array to a given aberration statistics is a potential work.

As already mentioned in the last paragraph of section 1, the present thesis discusses the optimization of microlens arrays through numerical methods to find an optimal array to be applied to the ophthalmic context. The optimal array found is later fabricated and tested in an optical bench.

5. APPLICATIONS OF THE HARTMANN-SHACK WFS

In this chapter, two of the main uses of the Hartmann-Shack wavefront sensor are discussed: aberrometry and adaptive optics systems. These techniques are broadly applied to the ophthalmic context in tasks such as diagnosis and treatment. Some examples of these applications are described. The benefits an optimized microlens array could bring to each specific application are also highlighted.

5.1.ABERROMETRY

Aberrometry, also called wavefront sensing, consists in measuring wavefront aberrations in an optical system. In particular, it is commonly used in ophthalmology, where the aberrations introduced by the optical parts of the human eye are measured by an aberrometer. The first commercially available clinical aberrometer was the COAS (Complete Ophthalmic Analysis System) From AMO Wavefront Sciences, released in 2000 (FAULKNER, 2011). Although the Hartmann-Shack method is commonly used in aberrometers since its advent up to now, there are currently several other methods also being used in such equipment.

It was already discussed that wavefront aberrations can be introduced in a light beam when it traverses a transparent medium. The human eye is therefore also prone to introducing aberration in the light that passes through its optical structures. These aberrations deteriorate the quality of the image formed in the retina, what may represent a loss of vision accuracy.

The anatomy of the eye is illustrated in Figure 43(a). The first transparent structure of the eye is the cornea, which is responsible for most of the total dioptric power of the eye. Behind the cornea, there is an aqueous medium called aqueous humor, which is in contact with the crystalline lens. The crystalline lens, or simply lens, is a deformable, gradient-index lens. It is responsible for the accommodation capability of the eye. Its deformation alters its dioptric power to correctly place the focused image exactly on the retina. Behind the lens, there is another aqueous medium called vitreous humor, which is in contact with the retina. In the retina, there are photosensitive cells, which are responsible for light perception, processing and, together with other different underlying cells, generation of signals that reach the brain.

In its way towards the retina, light passes through cornea, aqueous humor, lens and vitreous humor in this sequence, as illustrated in Figure 43(b)[19]. Any modification of these transparent media can introduce aberrations in the light beam; however, in general, aberrations are mainly due to cornea and lens (TAN, 2011).

[19] In practice, light also passes through a tear film before the cornea.

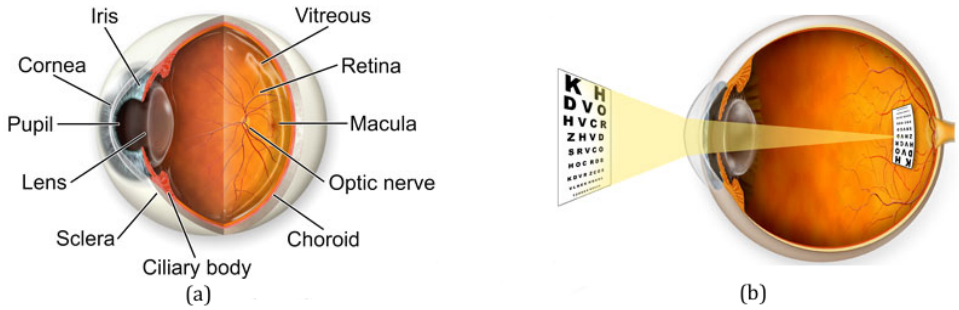

Figure 43 – Human eye anatomy (a) and optics (b).

In the aberrometers based on the Hartmann-Shack method, the eye is initially illuminated with a thin laser beam, generating a small laser spot on the retina[20]. This spot is projected onto the retina and then reflected back, as shown in Figure 44. The small projected spot behaves as a light point source and emits spherical wavefronts. The reflected light passes through the optical media of the eye and then reaches the Hartmann-Shack wavefront sensor. The sensor retrieves the quantitative information about the measured optical aberrations. In this method, light passes through the entire optical path of the eye, which means that all the optical components of the eye contribute to the measured aberration and their individual contributions cannot be separated. Another possible arrangement consists in illuminating the cornea and measuring the aberrations in the reflected beam. In this arrangement, the contribution of the cornea to the overall eye aberration can be separately measured. Moreover, the percentage of reflected light in the cornea is larger than that of the light reflected by the retina, which contributes to an improved signal-to-noise ratio on the wavefront sensor. Due to reflection, the measured aberration exhibits twice the amplitude of the aberration introduced by the cornea, which may represent an advantage since the light-spot displacements are larger and, therefore, low amplitude wavefronts may be measured more precisely as high amplitude ones.

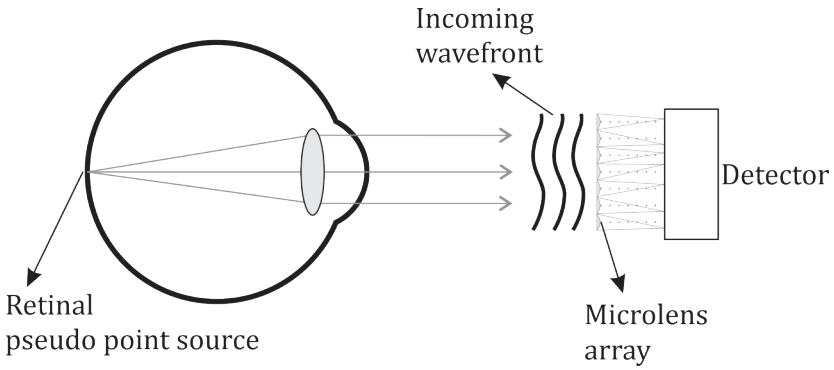

Figure 44 – Hartmann-Shack aberrometer used in ophthalmology.

Aberrometry is now applied to many different procedures in ophthalmology. One of the main uses of this technique is in customized laser eye surgery. In this procedure, the cornea is submitted to an excimer laser[21] to correct for the myopia, hyperopia,

[20] The laser spot is small in order to approximate a point source when the retina reflects the incident light. Therefore, the reflected wavefronts are as close as possible to spherical.

[21] Excimer laser uses light in the ultraviolet region. In laser eye surgery, the used wavelength is commonly 193nm, since it was believed to produce precise cuts with minimum thermal influence on adjacent tissues (BAGAYEV, RAZHEV and ZHUPIKOV, 1998). Nevertheless, recent studies

astigmatism and also for high order aberrations. This correction is achieved by reshaping the corneal surface so as to counterbalance for the aberration present in the optical system of the eye. Among the pre-operative procedures of this technique, aberrometry is used to map the aberrations of the eye (WANG and KOCK, 2005). With this information, the surgery can thus be planned and the laser equipment configured to ablate the corneal surface.

Aberrometry can also be used in the diagnosis of several diseases associated to the human vision, such as keratoconus, early cataract, lenticonus, pellucid marginal degeneration and several others (MAEDA, 2009).

Keratoconus is the modification of the corneal surface resulting in a conic shape, which leads to several impairments to vision quality (LAWLESS, COSTER, *et al.*, 1989). The patterns of high order aberrations change with the evolution of the disease, especially because of an increase of vertical coma aberration (MAEDA, 2009). Aberrometry can therefore be used to early diagnosis of keratoconus, as well as to grade the severity of the disease, as proposed by McMahon *et. al.* (MCMAHON, SZCZOTKA-FLYNN, *et al.*, 2006).

Lenticonus is a conical projection of the crystalline lens surface (anterior or posterior) and is associated to irregular astigmatism and, therefore, also causes decrease in the vision quality. Aberrometry may help in the diagnosis of lenticonus, since a high degree of spherical aberration is commonly associated to lenticular astigmatism in eyes with lenticonus (NINOMIYA, MAEDA, *et al.*, 2002).

Cataract is a very common eye disease associated to age. It is the principal cause of blindness in the world. The crystalline lens becomes progressively opaque and scatters light, the contrast sensitivity. When it seriously impairs the vision, the only effective solution is surgery to remove the natural lens and replace it with an artificial intraocular lens. In early stages, cataract progressively changes the wavefront aberration pattern of the lens, probably because of localized refractive index changes (PESUDOVS and ELLIOTT, 2003). Thus, Kuroda *et al.* (2002) suggest the use of Hartmann-Shack aberrometer to quantitatively analyze the progression of cataract by quantifying the wavefront aberrations of the eye.

Aberrometry may also help in the analysis of progression of pellucid marginal degeneration. The disease is characterized by a thinning of the cornea, typically in the inferior region. It results in a highly irregular astigmatism and decrease of vision acuity (KAMIYA, HIROHARA, *et al.*, 2003). Kamiya *et al.* (2003) report changes in the corneal aberrations in a patient with pellucid marginal degeneration and associate these changes to progression of the disease over the years.

The use of aberrometry to measure high-order aberrations of the eye also enables personalized correction of refractive errors. Customized contact lenses and intraocular lenses can be fabricated under demand to correct exactly for the specific patient's aberration profile.

---

propose different wavelengths as alternatives with a series of advantages (RAZHEV, ZHUPIKOV, *et al.*, 2009).

5.2.ADAPTIVE OPTICS SYSTEM

The first adaptive optics (AO) systems were initially developed specifically for applications in defense and astronomy, to overcome turbulent effects of the atmosphere (TYSON, 1999). Figure 45 illustrates the comparison of the observed images from an astronomical object generated by a telescope in two cases: when light passes through turbulent air and when there is no turbulence at all (hypothetical).

Although it is impossible to avoid the introduction of aberrations in the images when light passes through the atmosphere, it is feasible to compensate for these aberrations, using a deformable element in the optical system. Basically, in practice, the system must be capable of detecting the deformation present in the image, quantifying it and converting the results into information useful to actuate the deformable element. A requirement is that all this has to be continually performed in a loop and in real-time. Hence, an optical system like this would constantly adapt itself to the atmospheric turbulence, therefore compensating for the deformations present in the observed images.

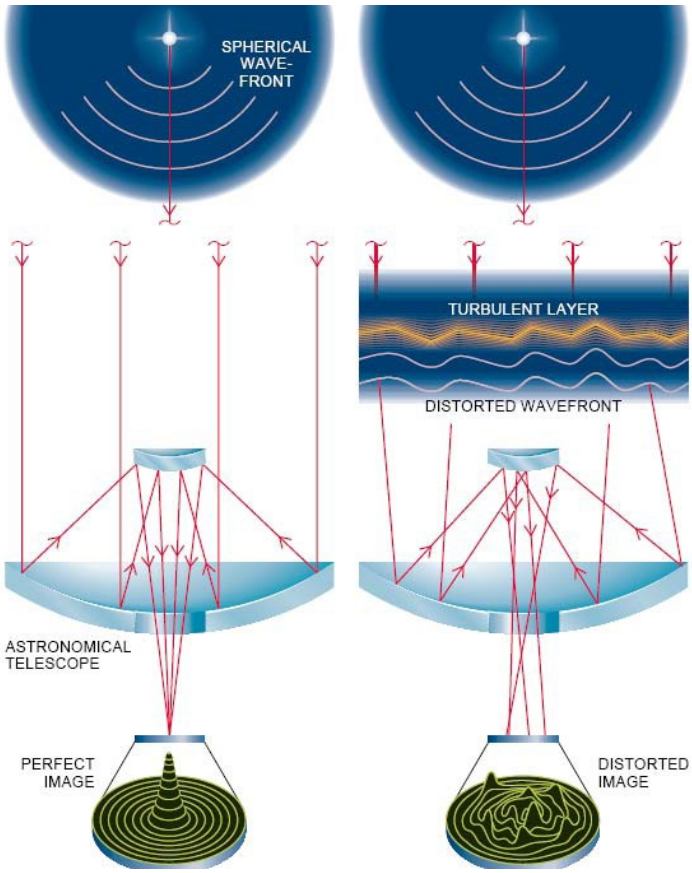

Figure 45 – Illustration of the effect of turbulent atmosphere on astronomical images (HEIN, 2005).

It was only in the past 25 years that non-military and non-astronomical applications of AO started to be developed. During this period, the interest in developing compact, low-cost and lightweight components and systems has been increasing significantly (GREENAWAY and BURNETT, 2004). As a consequence, the variety of applications that use AO systems has also been increasing in many different fields of knowledge.

In general, AO systems are used for basically two purposes (GREENAWAY and BURNETT, 2004):

a. improving the quality and the capabilities of optical systems, by compensating for distortions that affect light waves as they travel from the source to the imaging system, or
b. introducing a particular aberration in an optical system, so as to generate a particular output.

Adaptive optics systems are found in applications in many different areas. Some examples are listed below.

a. Astronomy: to improve image quality in optical and infrared astronomical telescopes and to compensate for laser beam distortion through the atmosphere (TYSON, 1999). It is also used in precision astrometry (CAMERON, BRITTON and KULKARNI, 2009).
b. Military defense: to increase accuracy in pointing and focusing airborne laser weapons to the intended target (U.S. DEPARTMENT OF DEFENSE, 2009).
c. Ophthalmology: to improve image quality in ophthalmoscopy, through measuring and correcting the high order aberrations of the human eye (ROORDA, ROMERO-BORJA, *et al.*, 2002; ZHANG, POONJA and ROORDA, 2006; CARROLL, GRAY, *et al.*, 2005).
d. Laser industry: to improve beam quality through compensating for the optical aberrations introduced during the amplification step in high-power lasers (OUGHSTUN, 1981; WELP, HEUCK and WITTROCK, 2007).
e. Laser-based materials processing: to increase reliability in processes such as welding, cutting, laser forward-transfer and other, through precise control of the shape of the intensity profile of the laser beam (ARNOLD and MCLEOD, 2007; JESACHER, MARSHALL, *et al.*, 2010).
f. Free-space communication: to increase reliability through compensation of the optical aberrations introduced in the laser beam by the propagating medium (ARNON and KOPEIKA, 1997; ARNOLD and MCLEOD, 2007).
g. Biomedical applications: to improve signal intensity and image quality in optical microscopy for medical imaging of tissues (WRIGHT, POLAND, *et al.*, 2007; GIRKIN, POLAND and WRIGHT, 2009).

The examples just listed illustrate how adaptive optics can be applied to many different areas. The increasing interest in a broad range of applications is confirmed by the papers recently published, which focus more on low-cost, robust, compact and lightweight complete systems and components, rather than on complex and expensive systems (VDOVIN, DE LIMA MONTEIRO, *et al.*, 2004). Such technological advances are crucial to expand the range of applications of adaptive optics.

Moreover, the growing interest in applications using adaptive optics is also confirmed by the volume of scientific literature in the field. The number of papers published referencing AO has increased from about 50 per year during the 1980s to about 500 in 2003 (GREENAWAY and BURNETT, 2004).

However, the interest in the development of AO applications is not only scientific. The evolution of the number of patents referring AO in the last decades reveals a growing commercial interest in the area. From the beginning of the 1980s to 2003, the number of granted patents per year referring AO has risen by a factor of four. Ophthalmology is the area with the largest number of patents referring AO (GREENAWAY and BURNETT, 2004).

All these aspects suggest that AO is a promising field for scientific and commercial investments, especially in medical and industrial areas. To ensure the feasibility of commercial applications, it is important to focus on the development of low-cost, compact and reliable systems and also of components that can be easily integrated, so as to guarantee the standardization and the possibility of series production.

All adaptive optics systems must perform two general tasks: wavefront sensing and wavefront correction (HEIN, 2005). In this sense, a general AO system is basically composed of three subsystems: wavefront sensor (WFS), such as Hartmann-Shack WFS; wavefront modulator and control system.

Figure 46 illustrates how the three subsystems are assembled together.

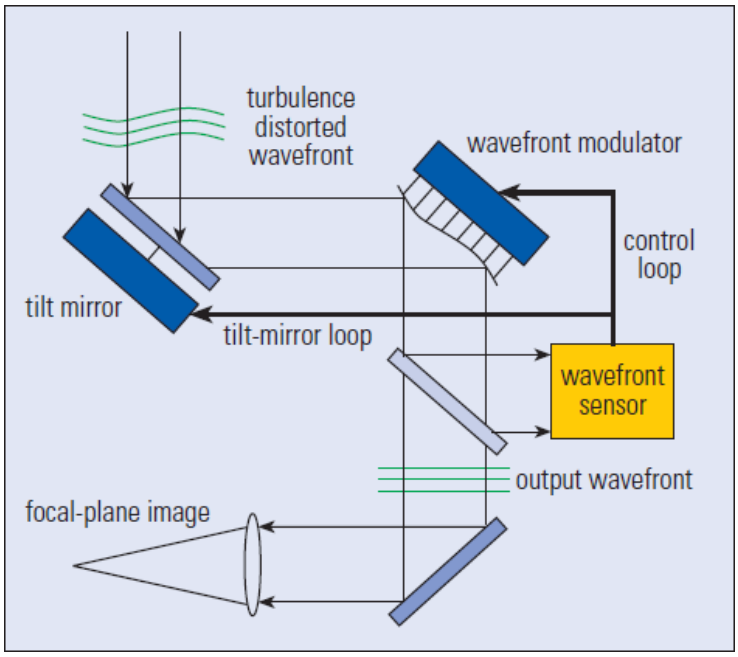

Figure 46 – AO system (GREENAWAY and BURNETT, 2004).

The wavefront modulator is responsible for modifying the wavefront shape appropriately, so as to correct for the aberrations present in the light beam A specialized tip-tilt control mirror is commonly used to compensate for the wavefront tilt, which offloads the modulator from the requirement of large strokes to compensate for such low-order aberration.

There are different types of wavefront modulators, which can actuate either through refraction or reflection. Some examples are: liquid-crystal phase modulators, continuous or segmented mirrors and bimorph mirrors (GREENAWAY and BURNETT, 2004).

The most widely used wavefront modulators for adaptive optics are the deformable mirrors. A deformable mirror can change its surface shape to match the phase distortions measured by the wavefront sensor (TYSON, 1999).

There are basically three types of deformable mirrors: segmented, bimorph and membrane. The segmented mirror surface is composed of small reflective parts, which can be individually actuated through mechanical mechanisms. The bimorph mirror makes use of PZT material, which deforms when voltage is applied to it. The membrane deformable mirror exploits electrostatic forces, electromagnetic coils (HAMELINCK, ROSIELLE, *et al.*, 2007), piezoelectric rod extension or thermal expansion (VDOVIN and LOKTEV, 2002; VDOVIN, LOKTEV and SOLOVIEV, 2007) to deform a flexible reflective surface. More details about it are given bellow. Greenaway and Burnett (2004) present a detailed description of other mirror types.

The micromachined membrane deformable mirrors (MMDM) consist of a silicon nitride membrane, metallically coated, built and anchored on a silicon chip. This structure is mounted on top of a PCB holder, which also contains the electrodes and the corresponding wiring. Figure 47 illustrates the mirror.

Through application of DC voltage to the electrodes, the mirror surface is pulled down due to electrostatic attraction. Each electrode deflects the mirror surface locally. When the electrodes are conveniently actuated, the local deflections are superimposed so as to form the desired shape. Therefore, different regions of the mirror surface will alter individually the optical path length of different parts of an impinging aberrated wavefront, so as to compensate for deformations present before. Figure 48 illustrates the correction of an aberrated wavefront using a MMDM.

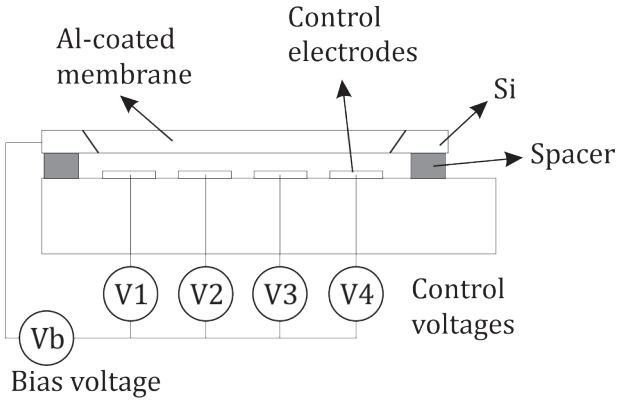

Figure 47 – Micromachined membrane deformable mirror (OKO TECHNOLOGIES, 2006).

Since the electrodes actuate only through surface attraction, the electrodes can be biased to a nominal voltage, so that the membrane can be deflected during the operation either downwards or upwards therefore compensating for both convex and concave distortions.

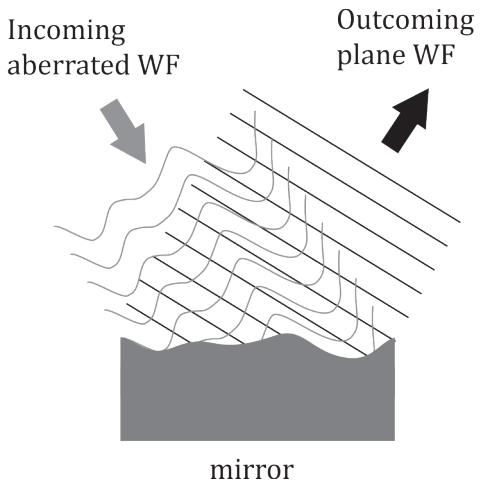

Figure 48 – Representation of a reflective surface correcting for wavefront aberration.

The mirror requires an electronic driver, responsible for applying the correct voltages to each electrode, according to the commands of the control system (PC board, for example). It also demands a high-voltage amplifier, which converts the output signals of the control system into the DC high-voltage that is applied to the electrodes. Usual voltages can be as high as 300V.

The control system is responsible for interpreting the output information of the wavefront sensor and generating signals for the wavefront modulator operation. In general, the control systems comprise a computer and peripherals, such as analog/digital converters and voltage amplifiers. The control task reduces then to writing algorithms capable of generating output signals to drive the mirror in order to compensate for the wavefront aberration.

A great deal in generating the output signals for driving the mirror refers to converting the wavefront aberration information into voltage signals. It depends on mirror characteristics, such as possible modes that can be reproduced and the influence functions Influence functions describe how the operation of each electrode alters the mirror surface. They can be determined with a H-S wavefront sensor. By actuating each electrode at a time, the set of measured spot deviations, which are associated to the aberration introduced by the mirror in a reference beam, corresponds to the influence function of the respective electrode.

Once the influence functions of the mirror are determined, it can be used to compensate for some wavefront aberration. The procedure consists in relating the light-spot deviations of the test aberration to the voltages applied to the mirror. In this case, the wavefront aberration is not described in terms of Zernike polynomials. Instead, the basis used consists of the influence functions of the mirror. Therefore, the Zernike derivatives in matrix $\boldsymbol{B}$ of equation 12 are replaced with the measured spot deviations that describe the influence functions. The result of equation 15 is matrix $\boldsymbol{C}$ which, in this case, contains the square of the voltages to be applied to the mirror, rather than the Zernike coefficients (DE LIMA MONTEIRO, 2002). The voltage information is then sent to the hardware interface, which will actually apply, according to the control commands, the specified voltages to each of the actuators.

Figure 49 and Figure 50 compare images obtained in systems with and without adaptive optics in two of the main applications: astronomy and ophthalmology.

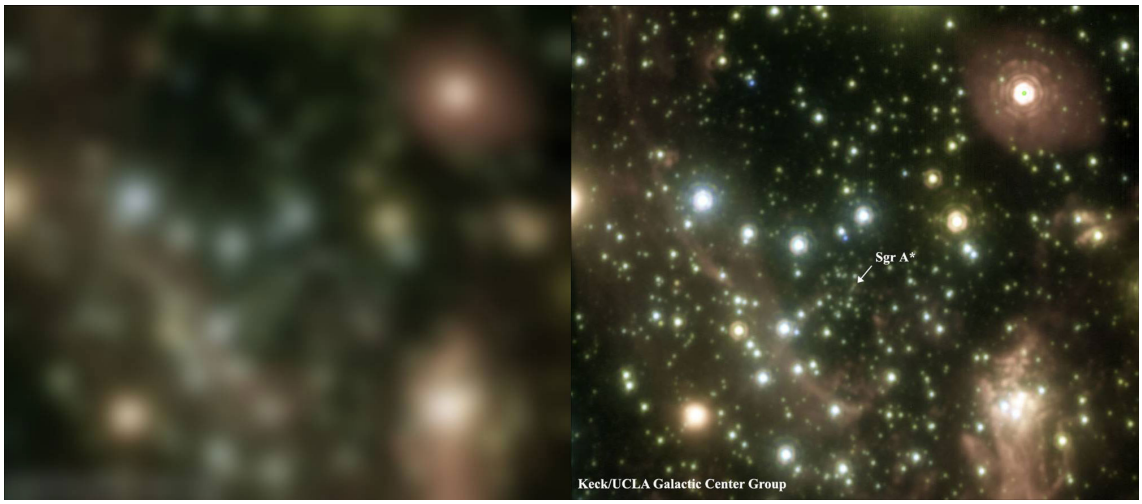

Figure 49 – Astronomical images taken with (right) and without (left) AO (KECK OBSERVATORY; UCLA GALACTIC CENTER GROUP, 2007/2008).

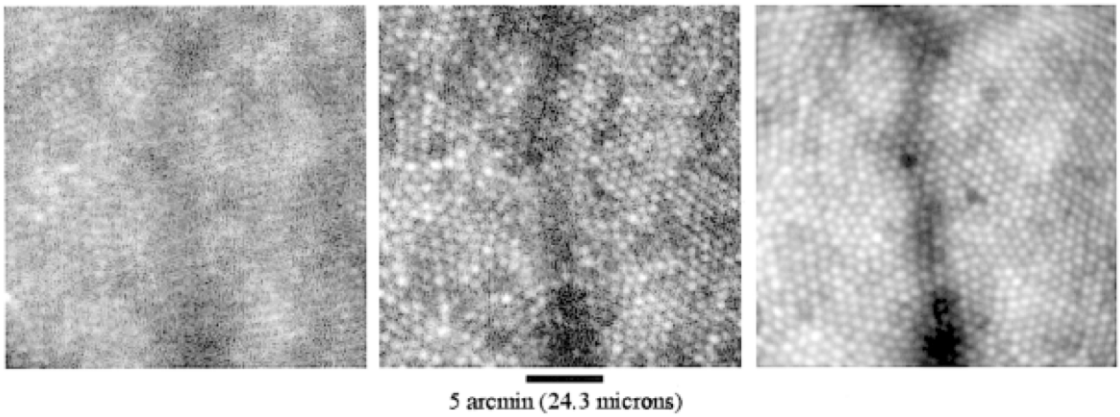

Figure 50 – Retinal image with (center and rightmost) and without (leftmost) AO for the right eye of a living human subject. The image in the center is just a snapshot while the image on right is an average of 61 frames (ROORDA, 2000).

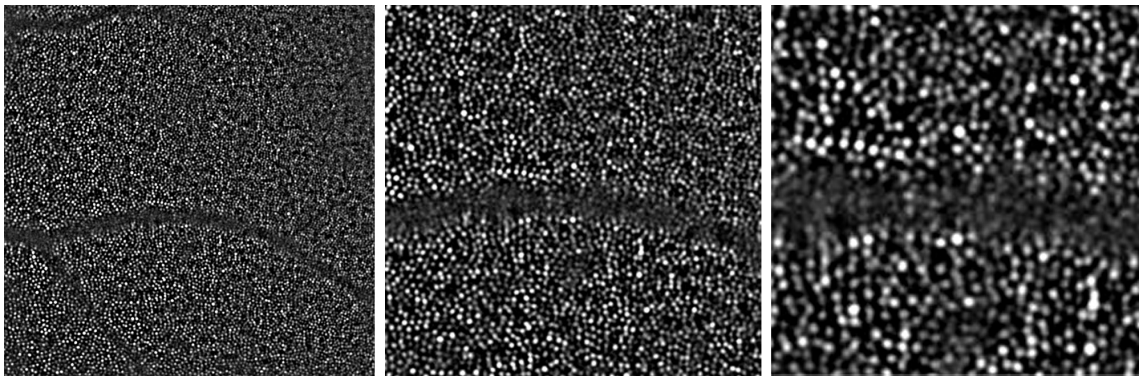

Figure 51 – Series of images showing how cones can be imaged in detailed using AO (IMAGINE EYES SA).

In all real-time adaptive optics systems, such as the examples shown, any improvement that provides reduction in processing time is of great importance, since it contributes to a higher operational frequency. In some contexts, the propagating medium changes very quickly and therefore causes the aberrations to fluctuate at high frequencies. For instance, that is the case of thermal fluctuations in the atmosphere or saccadic movements of the human eye. In such situations, AO systems must operate at compatible frequencies to appropriately compensate for the aberrations. Therefore, processing time is a critical aspect in these cases. In this sense, the optimized microlens array may play an important role if the number of microlenses can be reduced without any prejudice to the wavefront error. Since the number of light spots to be analyzed is smaller, the volume of data regarding spot deviations is also reduced and, therefore, the necessary time to interpret this data and convert it into data to drive the deformable mirror is also smaller.

6. METHODS, RESULTS AND DISCUSSIONS

6.1.MICROLENS ARRAY OPTIMIZATION FOR APPLICATION IN OPHTHALMOLOGY

The wavefront sampling is influenced by the microlens distribution pattern, lens contour and size, number of microlenses and fill factor. As discussed before, studies demonstrate that random patterns provide smaller reconstruction errors than regular ones. This work aims at finding the microlens distribution pattern in the array that minimizes the reconstruction error in a Hartmann-Shack wavefront sensor for ocular aberration statistics.

The aberrations introduced in a light beam depend on characteristics of the medium. This set of characteristics that describe the medium impose that the aberrations it introduces in a light beam contain similarities. In other words, typical aberrations are associated to each medium. To each of these contexts, i.e. set of characteristics that describe a medium, an appropriate statistical model can be associated to describe the typical aberrations it introduces in a light beam. For example, aberrations introduced by the atmosphere are generally described by the Kolmogoroff model (NOLL, 1976). Aberrations introduced by the human eye can be described by models based on the measurement of aberrations in a large population (PORTER, GUIRAO, *et al.*, 2001). Another context refers to the aberrations introduced by underwater environments, due to water turbulence, temperature and salinity variations, what can affect significantly the quality of underwater imaging (YURA, 1973; HOLOHAN and DAINTY, 1997).

In this work, the wavefront aberrations used were generated by the statistical model for ocular aberrations described in section 6.1.3. Therefore, the microlens array will be optimized for ophthalmological purposes, although the proposed methodology can be carried out with any other wavefront-aberration statistics.

The importance of specifying an optimal array for ophthalmology is expressed in the words[22] of Llorente *et al* (2007):

> *The determination of a sampling pattern with the minimum sampling density that provides accurate results is of practical importance for sequential aberrometers, since it would decrease measurement time, and of general interest to better understand the trade-offs between aberrometers. It is also useful to determine whether there are sampling patterns that are better adapted to typical ocular aberrations, or particular sampling patterns optimized for measurement under specific conditions.*

It is important to emphasize that Llorente *et al* use laser ray tracing, instead of Hartmann-Shack, which is used in this work (see description in section 3.3). Nevertheless, his comments are applicable for both techniques, because the LRT requires a sampling pattern in the same manner as the H-S. The difference is that in the H-S, the sampling pattern is defined by the array geometry, whilst, in the LRT, it is defined by the

[22] Just to match vocabulary, the word “samples” stands for “microlenses” and the term “sampling pattern” stands for “microlens array”.

predetermined positions in which the laser beam impinges in the test object. In the H-S method, the light-spot pattern is generated at once, while, in the LRT, it is generated spot by spot. The final light-spot patterns of each method are then comparable, and so is the final result (MORENO-BARRIUSO, MARCOS, *et al.*, 2001).

Note that, besides determining an optimal microlens array for a specified number of microlens, it is also desirable to determine arrays with a smaller number of microlens, preserving the reconstruction error magnitude. Both aspects are exploited in this work.

The process to find an optimal microlens array is carried out numerically. In this work, the used optimization method was the genetic algorithm (GA), which is treated in detail in section 6.1.4. In order to search for the best microlens array, it is necessary to specify an objective function, independently of the choice of the optimization method.

Generally speaking, an objective function is a function associated to an optimization problem, which is maximized or minimized through some numerical optimization method. The objective function describes analytically or numerically, as in the present case, the problem to be optimized. Its input data consist of the variables of the modeled problem while its output is an optimization parameter, which is the value that should be minimized or maximized. In other words, the numerical optimization method seeks for the set of values for the variables of objective function that minimizes or maximizes the value of the optimization parameter.

In the present context, the inputs to the objective function are the microlens array and the wavefront aberration. Its output is the reconstruction error, i.e., the parameter to be minimized (See Figure 52).

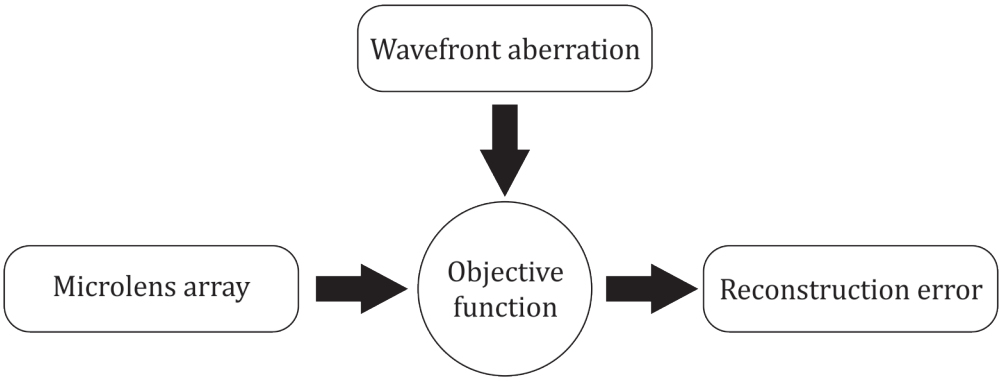

Figure 52 – Objective function for the microlens-array optimization.

As mentioned before, the reconstruction error measures how inaccurate the reconstructed wavefront matches the original wavefront shape. The sources for this error include wavefront sampling, microlens imperfection, numerical round-offs, misalignment of optical components, detection of light spots, misalignment between microlens and PSD arrays, noise in the electronic circuitry for readout of the output of the wavefront sensor and sampling of the electrical signals.

The objective function must represent the whole Hartmann-Shack method. As in this case the purpose is to assess the performance of microlens array, the emphasis is on the reconstruction error due to the wavefront sampling process. Therefore, an algorithm was

used to simulate the Hartmann-Shack method, including the steps of generation of an incoming wavefront, input to a specified microlens array, wavefront sampling, calculation of light-spots deviation, wavefront reconstruction and calculation of the reconstruction error. The detection step is not taken into account and is, in practice, performed by a camera or a 2D array of position-sensitive detectors.

Once the objective function is defined, one must specify an optimization method, which will be responsible for trying to find the microlens array that minimizes the reconstruction error. Therefore, the input to the optimization method will be the reconstruction error and its output will be the microlens array. Figure 53 illustrates the relation among optimization method and objective function.

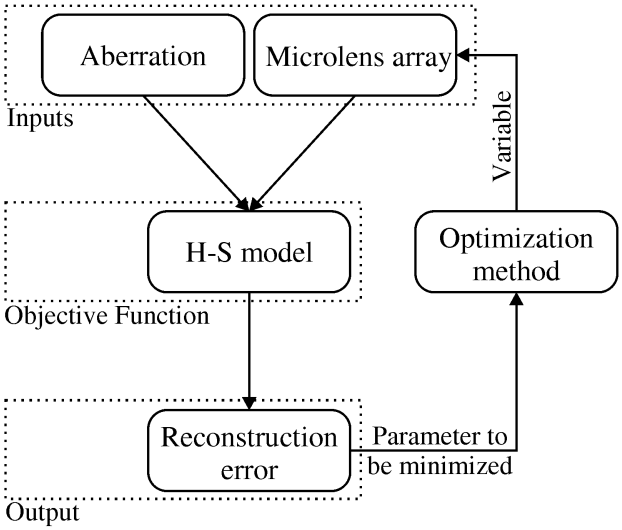

Figure 53 – Schematics of the optimization function operation.

To provide the wavefront aberration input to the objective function, an algorithm must be built for generating the aberrations according to the desired statistics.

The next sections will treat in detail the algorithm to simulate the Hartmann-Shack method and the chosen optimization method.

6.1.1. NUMERICAL MODEL OF THE HARTMANN-SHACK METHOD

An algorithm built in C++ language was adapted from a source code initially developed at the Electronic Instrumentation Lab/TU-Delft/The Netherlands by G. Vdovin, D. W. de Lima Monteiro and S. Sakarya to simulate a Hartmann-Shack system. As previously stated, the detection of the light-spots positions is not taken into account here, since the focus is on the reconstruction error generated by different microlens arrays.

Figure 54 below shows a block-diagram of the algorithm. Steps 1 and 2 are used to initialize the algorithm by setting the values of all global parameters needed in the calculations. Steps 3 and 4 comprise the input of two externally generated variables: microlens array and incoming wavefront aberration. In step 5, the aberration is sampled by the microlens array. Steps 6 and 7 are for the reconstruction of the wavefront aberration from the information generated by the sampling process. Finally, in step 8, the reconstruction error is calculated. More detailed comments on each step are given below.

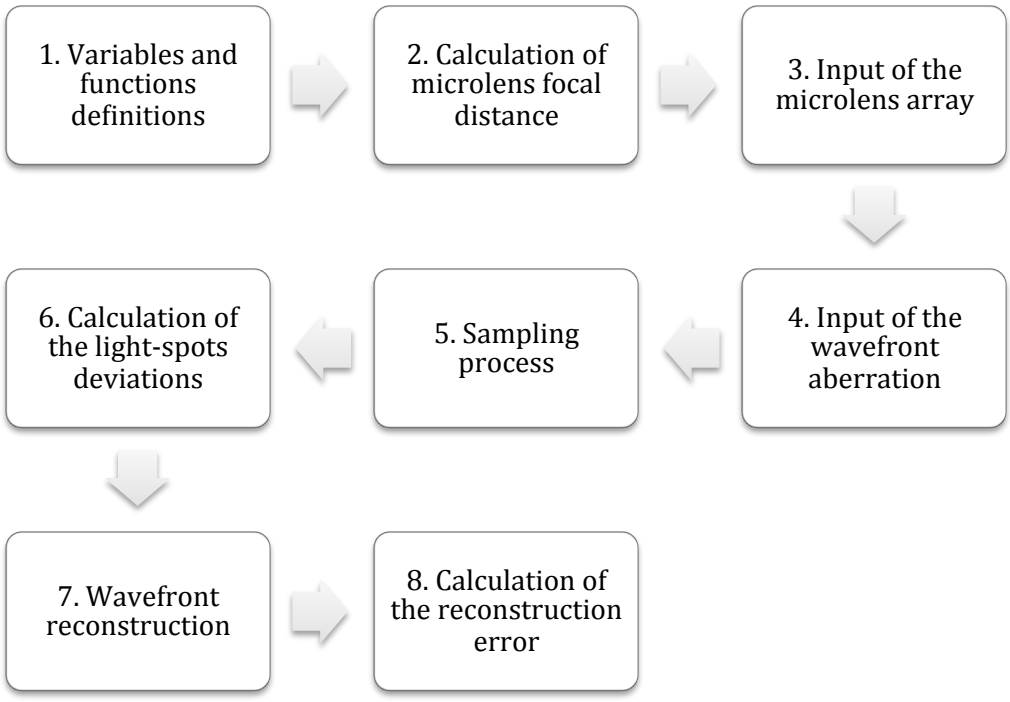

Figure 54 – Block-diagram of the Hartmann-Shack numerical model.

In step 1, all the global variables and functions used in the algorithm are declared and initialized. Values such as number of Zernike terms, lateral size of the microlens array and number of microlenses in the array are set in this step. Moreover, some microlens characteristic parameters, such as diameter, index of refraction and curvature radius, are also set in step 1.

The index of refraction of the microlens was set to 1.4, to match the commercially available materials for lenses fabrication (PMMA, for instance). A reasonable focal distance (4cm) is compliant to the minimum curvature radius of 16,000μm, achievable with the microlens-array fabrication constraints of our clean room lithographic equipment and etching method (DE LIMA MONTEIRO, AKHZAR-MEHR, *et al.*, 2003; DE LIMA MONTEIRO, AKHZAR-MEHR and VDOVIN, 2005). These values have been set so to later guarantee the possibility of fabrication of the specified microlens array.

The microlens array was chosen to feature a square perimeter with a lateral dimension of 6mm. The microlens are circular and the starting number of microlens in the array is 36, where all lenses are plano-convex and have the same diameter. In this case, the maximum possible diameter for the microlens is 1,000μm, in which case the only feasible configuration is the rectangular one. To guarantee some degree of freedom for the lens-position randomization, the microlens diameter must be smaller than 1,000μm. The initially chosen diameter was 750μm. The used wavelength was 633nm.

Once the curvature radius and the index of refraction of the microlens are specified, their focal distance can be calculated, in step 2, using the simplified Lens-Marker's formula (HECHT, 2002) and assuming there is air on both sides (equation 17).

$$f = \frac{R}{n-1} \qquad 17$$

In step 3, the microlens array configuration is passed to the algorithm, which is prepared to receive this data through two different ways. In one of them, the coordinates of each microlens are written manually and directly on the source code. It can be used when many simulations are carried out with the same microlens array, as in the regular case. In the other way, the coordinates are written in an external text file, which is read by the algorithm. The text file containing the microlens distribution in the array is written by the optimization algorithm.

The wavefront aberration is passed to the algorithm in step 4, also through a text file. An external module (see section 6.1.3) is responsible for generating the wavefront aberration and writing the respective Zernike coefficients in a '.txt' file. The Hartmann-Shack algorithm then accesses this file and reads the coefficients values.

In step 5, the wavefront is sampled by the microlenses. For each microlens, the algorithm takes 45 points and calculates the derivative of the wavefront aberration for all of them. The number of points was chosen arbitrarily. Then, the mean derivative is calculated and stored in a variable correspondent to that microlens. The output of step 5 is, therefore, the tilt measurements for all the microlenses.

The tilt data has to be converted into deviation measurements before the wavefront reconstruction. This is done in step 6 through a mathematical model for lenses, which is described in section 6.1.2.

The wavefront reconstruction is performed through the solution of equation 13:

$$\boldsymbol{B}^T\boldsymbol{S} = [\boldsymbol{B}^T\boldsymbol{B}]\boldsymbol{C}$$

where $\boldsymbol{S}$ is a vector containing the deviations measurements, $\boldsymbol{B}$ is a matrix of the Zernike terms derivatives, $\boldsymbol{B}^T$ is its transpose, and $\boldsymbol{C}$ contains the coefficients to be found.

The system of linear equations is solved through the use of Gauss elimination with partial pivoting and back-substitution algorithm (PRESS, TEUKOLSKY, *et al.*, 1992), in step 7. The output of this step is vector $\boldsymbol{C}$, which contains the Zernike coefficients.

Finally, in step 8, the root-mean-square (rms) reconstruction error between the reconstructed and original wavefronts is calculated. The algorithm finishes by writing this error value in an external text file.

It is important to note that the reconstruction error generated by Hartmann-Shack algorithm includes basically two sources of errors. One is due to the wavefront-sampling step. The other is related to numerical round-offs, which take place in the wavefront reconstruction step. What is pursued in this work is to minimize the wavefront-sampling error. However, it is not possible to separate it from the numerical errors. Therefore, what is called reconstruction error from here on in this work actually refers to sampling plus numerical errors.

To close the loop, the optimization algorithm accesses this file and generates, based on the reconstruction error value, a new set of microlens coordinates, which will serve as input to step 3 in the next iteration.

6.1.2. MATHEMATICAL MODEL OF LENSES

To convert the wavefront local tilts onto each microlens into deviation measurements on the focal plane, a model describing how plano-convex lenses influence the propagation direction of light should be used. The model developed here is quite rigorous, so as to be sufficiently general to include thick lenses. To describe the model, consider the following definitions on Table 2.

Table 2 – Definition of variables to describe the lens model.

Symbol	Name
C	Curvature center
R	Curvature radius
n	Index of refraction of the lens material
n'	Index of refraction of the external medium
d	Sagitta
D	Lens diameter
A	Output point of the light beam
m	Distance between point A and the focal plane
V	Lens vertex and input point of the light beam
l	Distance between the lens and the focal plane
f	Focal distance
Δx	Deviation of the light beam from the optical axis measured on the focal plane
r	Distance between the input and output points
δ	Distance between the optical axis and the exit point A
θ	Input incident angle
$\omega, \gamma, \beta, \alpha$	Angles

Figure 55 illustrates a light beam reaching a lens. From the geometrical representation of the system, relations can be built between various angles and distances, so as to find the beam deviation from the optical axis Δx. The equations derived from the geometrical representation of Figure 55 are the following:

1. Snell's Law;

$$\sin\theta = n \cdot \sin\alpha \quad (18)$$

$$n \cdot \sin\beta = \sin\gamma \quad (19)$$

2. Sine's Law (triangle CÂV);

$$\frac{R}{sin(180-\alpha)} = \frac{R-d}{\sin\beta} = \frac{r}{\sin\omega} \quad (20)$$

$$R \cdot \sin\beta = (R-d) \cdot \sin\alpha \Rightarrow \sin\beta = \frac{R-d}{R} \cdot \sin\alpha \quad (21)$$

3. Geometrical description of the system;

$$\omega = \alpha - \beta \quad (22)$$

$$r \cdot \sin\alpha = R \cdot \sin\omega = \delta \quad (23)$$

$$m = (l+d) - r \cdot \cos\alpha \Rightarrow m = f - \frac{R \cdot \sin\omega}{\sin\alpha} \cdot \cos\omega \quad (24)$$

$$\Delta x = m \cdot tan(\gamma+\omega) + \delta \quad (25)$$

$$(R-d)^2 + \left(\frac{D}{2}\right)^2 = R^2 \quad (26)$$

$$f = l + d \quad (27)$$

4. Lens'-makers equation for a plano-convex lens in air (equation 17).

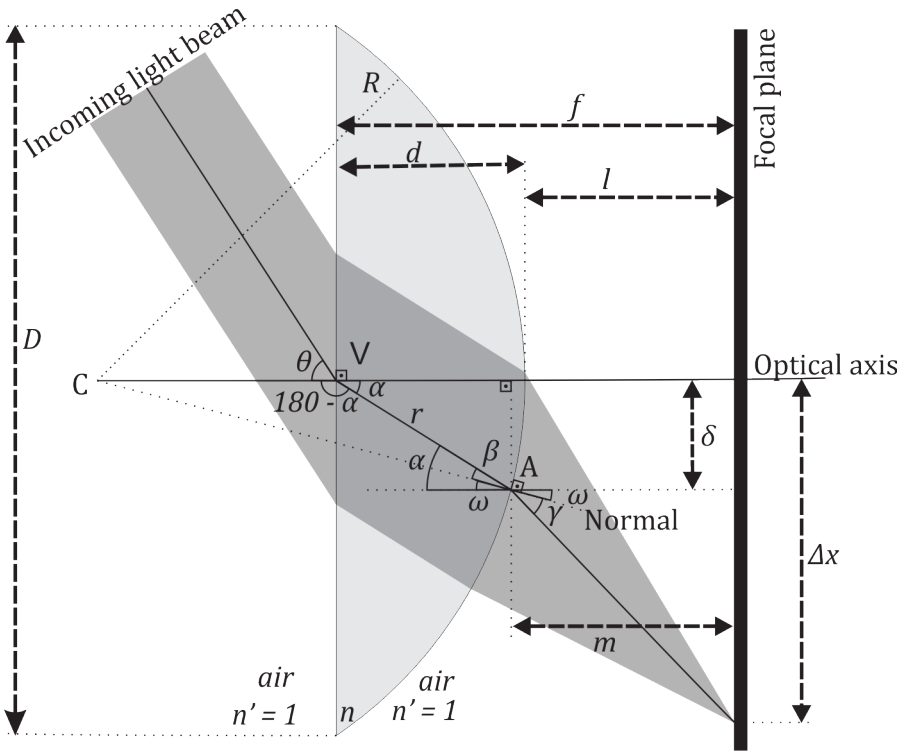

Figure 55 – Geometrical representation of the optical system.

The calculation of Δ*x* is done through the following steps: (in the bottom of each box, the necessary inputs to the respective current step, as well as the generated output are highlighted).

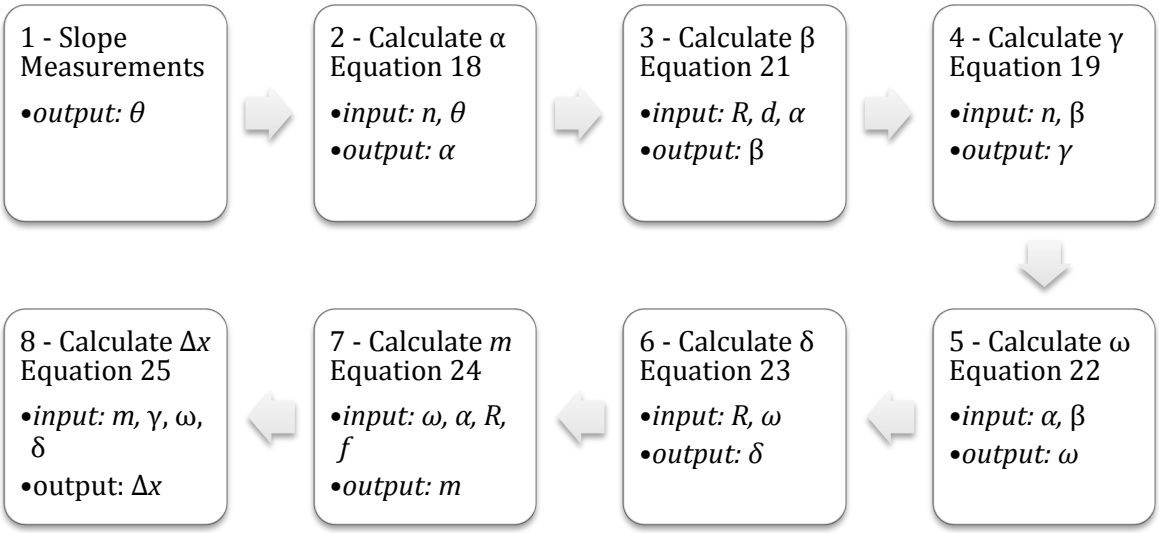

Figure 56 – Steps for calculating the light beam deviation after passing through a plano-convex lens.

6.1.3. WAVEFRONT ABERRATIONS GENERATOR

The algorithm to generate wavefront aberrations was developed based on statistics of ocular aberrations according to Porter *et al.* (2001) who listed the typical mean values and spread of the Zernike coefficients for a mean pupil diameter of 5.7 mm. They have

measured the wavefront aberrations of both eyes of 109 normal human subjects and analyzed the aberration distribution in the population, describing it in terms of 18 Zernike coefficients, what corresponds to the fifth Zernike order (piston and tilt are not considered). After computing and plotting the mean values and corresponding standard deviation of all Zernike coefficients, they present the results through a graph of error-bars centered in their mean values.

This data was used in this work as a basis for writing the wavefront-aberration generator algorithm. The idea is to generate wavefront aberrations that belong to a statistical description based on real measurements, so as to simulate a real application. To do that, Gaussian probability distributions (equation 28) were associated to each of the Zernike coefficients.

$$f(x) = \frac{1}{\sqrt{2\pi\sigma^2}} e^{-\frac{(x-\mu)^2}{2\sigma^2}} \qquad 28$$

In equation 28, μ stands for the mean value of each coefficient and σ, for the standard deviation. The values of μ and σ for each Zernike coefficient are taken from the data reported by Porter *et al.* (2001). As the results are reported in the article only through a graph, the mean values and corresponding standard deviations were assessed visually from the graph scale.

To demonstrate accordance between the results generated by the simulation algorithm and the ones actually measured by Porter *et al.* (2001), 10,000 wavefront aberrations were generated. The mean value and the standard deviation for each Zernike coefficients were computed and plotted. The result is shown in Figure 57. This graph reproduces exactly the result found by Porter *et al.* (2001, p. 1796), which is based on the real measurement of wavefront aberrations of 218 human eyes.

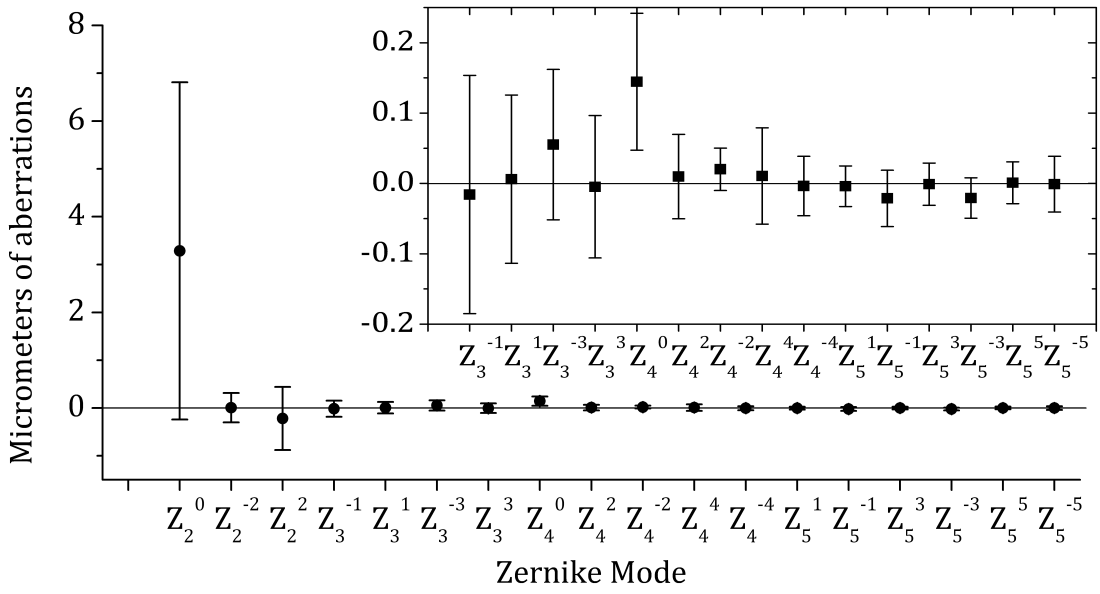

Figure 57 – Zernike coefficients distribution generated by the algorithm.

In this work, the simulations use the first 20 Zernike modes, once that is the maximum number of modes with available statistics in the work of Porter *et al.* (2001). Moreover, De

Lima Monteiro *et al.* (2006) states that optical aberrations in the human eye are significant only to the first 14th Zernike modes, including tip and tilt. However, tip, tilt and defocus were not considered, so that the microlens array could be optimized to provide a more precise sampling of higher order Zernike terms. More reconstruction modes could be used, if they were known by the statistics. It is relevant to comment here also that a larger number of reconstructions modes can also be used to eliminate aliasing from the measurement with non-regular arrays, as described in De Lima Monteiro *et al.* (2006) and referred to as undermodeling (WANG and SILVA, 1980). The idea consists in reconstructing the aberrated wavefront using more than the M terms of interest and then discarding the highest-order supposedly unnecessary coefficients, which are responsible for the main aliasing error included in the first M modes.

It is important to emphasize that the statistics used in this work is not complete to generate statistically robust ocular aberrations, once it was derived directly from the final results presented by Porter *et al.* (2001) in which the measured Zernike coefficients for each member of the analyzed population are not available. Because of this limitation, one cannot generalize the obtained results. However, as more complete statistical models are available, the whole procedure can be repeated and a new optimized array can be specified. Therefore, the used statistics is to be understood as an example of application and as a first approximation for ocular aberrations.

6.1.4. OPTIMIZATION ALGORITHM

The optimization problem treated in this work consists in minimizing the reconstruction error of a Hartmann-Shack sensor by means of an optimal distribution pattern to the microlens array.

A requirement of the present problem, that affects the choice of the optimization method, is that the objective function that describes the problem cannot be written in an analytical form. That is because the simulation of the Hartmann-Shack method includes several recursive independent operations on the input variables, which cannot be translated together into an analytical function. Therefore, the optimization method to be used should access only the input variables to the Hartmann-Shack simulation and its output result, independent of how the simulation operates the input to generate the reconstruction error as an output.

The fact that the objective function cannot be analytically described is imposed mainly because of the available ocular aberrations statistics, which does not contain a detailed description of the individual aberration measurements performed in each eye. If they were available, a mathematical model could have been used to estimate the wavefront reconstruction error without the need to simulate the whole H-S method. This model was proposed by Diaz-Santana *et al.* (2005) and consists of analytical expressions to calculate the reconstruction error for a known statistics. The expressions require the measured Zernike coefficients for each member of the statistics population in order to evaluate the correlation between Zernike terms. This is not available in the statistical data by Porter *et al.* (2001) used here.

Another limitation is that the present objective function presents many local minima, mainly due to the large number of variables in the problem. It is called a multi-modal function.

Considering these aspects, the optimization method chosen was the Genetic Algorithm (GA) – refer to (MITCHELL, 1999) for a detailed study about GA. The GA is a method to solve both constrained and unconstrained optimization problems and is based on natural selection, the process that drives biological evolution. The genetic algorithm repeatedly modifies a population of individual solutions. At each step, the genetic algorithm selects individuals from the current population to be parents and uses them to produce the children for the next generation. This selection is based on a probability distribution in which the best individuals have larger probability to be chosen. Over successive generations, the population "evolves" towards an optimal solution. GA can be applied to solve a variety of optimization problems that are not well suited for standard optimization algorithms, including problems in which the objective function is discontinuous, non-differentiable, stochastic, or highly nonlinear (THE MATHWORKS, INC., 2010).

The software MatLab© (R2008a) contains a toolbox (OPTIMTOOL – Optimization Toolbox 4.0) for optimization problems using several different methods, including GA.

The following steps summarize how GA works (THE MATHWORKS, INC., 2010):

a. Initially, the algorithm creates a random initial population. The population comprises individuals, which correspond to the coordinates of different microlens arrays. The toolbox can generate this initial population by itself; however, if restrictions are present a function has to be written to generate the individuals. In the present problem, the arrays have a restriction: the minimum distance between two microlenses cannot be less than the microlens diameter; otherwise adjacent lenses become superimposed. Therefore, a numerical function had to be written to generate the initial random population.
b. The algorithm then creates a sequence of new populations. At each step, the algorithm uses the individuals in the current generation to create the next population, through the following steps:
    i. Scores each individual of the current population by computing its fitness value (a value associated to the wavefront reconstruction error, in this case), i.e., the output of the objective function.
    ii. Order the individuals of the current population according to a specified criterion. The rules for ordering the individuals can be chosen in the algorithm. A standard procedure consists in organizing them according to an ascending order of their fitness values.
    iii. Selects individuals, called parents, to generate new individuals, called children. Here, the selection is based on the fitness value. Therefore, parents and children are also sets of microlens coordinates.
    iv. Some of the individuals in the current population that have higher fitness values, i.e. smaller reconstruction error, are chosen as elite. The elite individuals are passed to the next population.
    v. Produces children from the parents. Children are produced either by making random changes to a single parent (mutation) or by combining the

vector entries of a pair of parents (crossover). More details about the children generation are given below.

vi. Replaces the current population with the children and elite individuals to form the next generation.

c. The algorithm stops when one of the stopping criteria is reached. The criterion can be a minimum difference in the fitness value among the individuals of the population, or a maximum number of generations, or a specified minimum value for the fitness function, etc.

The new generation is then composed of three types of children: elite, crossover and mutation. Figure 58 illustrates how each type is created from the correspondent parent.

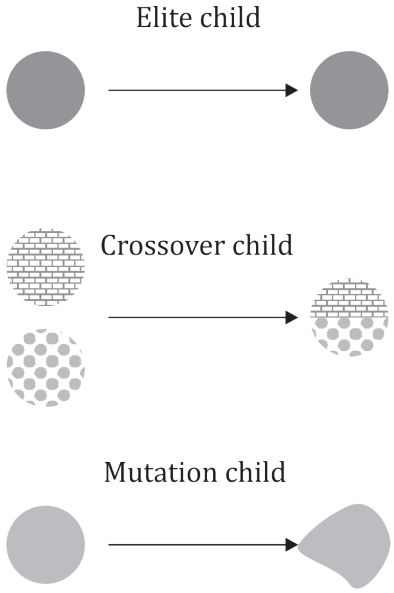

Figure 58 – The three types of children in a new generation.

The elite children are passed to the next generation without any changes. They correspond to the individuals of higher fitness value in the present generation. The number *e* of elite individuals in each generation has to be set in the algorithm. Once this number is defined, the other individuals will be generated either through crossover or mutation. In this work, the elite operation means that the *e* microlens arrays that have generated the smallest reconstruction errors are simply repeated in the next generation, without any changes.

The fraction of the population that will be generated through crossover has to be set in the algorithm. The others are therefore generated by mutation.

The mutation operation consists in making small random changes in the individuals of the population. Mutation guarantees genetic diversity to the algorithm. That means that the search for the optimal solution will occur in a broader space of possible solutions. In the present context, the mutation consists in causing small changes to the microlenses coordinates of an array.

The crossover children are generated by a combination of a pair of parents. There are different functions to control the combination. One of them consists in taking a randomly weighted average of the pair of parents. In the present problem, the crossover operation

means mixing two different microlens arrays: *A* and *B*. The combination may consist, for instance, in selecting some microlenses from *A* and some others from *B* and then putting them together to form the new array. It may also consist in averaging, for each microlens, the coordinates given by both arrays, so as to build the new children. The way the pair of parents is combined is specified in the algorithm.

The operations of mutation and crossover are controlled by specific operator algorithms, which are already included in the toolbox to be selected by the user. The operators chosen in this work are described in section 6.1.5.

6.1.5. METHODOLOGY

This section discusses how to approach the microlens randomization problem using the optimization tools available.

Before discussing the methodology itself, it is very important to emphasize one aspect: the objective function has many local minima. This makes the problem very difficult to solve, in terms of finding a global minimum and also proving it is actually the global one.

An important fact to consider is that the optimized, supposedly random, array has to yield an error lower than that of the regular lens array at least for the majority of incident wavefront aberrations. The number of possible wavefront aberrations, according to the ocular aberrations statistics, is infinite. Therefore, a possible approach to the problem would be to select some wavefront aberrations and then find the optimal array for each of these aberrations. The arrays found would then be averaged so that one single array could be specified as the optimized array (mean array, in this case).

However, that approach would not lead to significant results, because the mean array is very similar to the rectangular one. The problem is that the arrays can be very different from one optimization process to the other, due to not only the different input aberrations, but also the undetermined number of local minima. Therefore, in the average, the microlens coordinates tend to be those of the rectangular array. Moreover, trying to find the best array through some kind of mathematical manipulation of the arrays previously found can lead to catastrophic results, since the objective function is very sensitive to small changes in the microlens positions and because there is a restriction that two microlens centers cannot be closer than one microlens diameter.

The methodology developed for optimizing the microlens array is summarized in the following outline:

1. Five different aberrated wavefronts were generated based on the statistics by Porter *et al.* (2001): four aberrations randomly produced by the wavefront generator algorithm and one aberration featuring mean-valued Zernike coefficients. For a given microlens-array geometry, the H-S model computes the reconstruction error for each of these five aberrations, from which an average error is obtained. The average error is the parameter to be minimized by the GA. This set of five aberrations is fixed and is used in all the tests performed.
2. The genetic algorithm creates the first generation of arrays with random distributions of microlenses. For each array, it computes the average error over

the five aberrations mentioned above. The error values are used by the algorithm to define the expectation with which each array can be selected as a parent, so that the array with the smallest error is more likely to be chosen. Based on these values, the GA selects arrays to be used in the creation of the next generation, through the operations of elite, mutation and crossover. This step is done successively, until the average variation of the error over the 10 last generations is smaller than $1.58\times10^{-11}\lambda$. Then, the final result consists of the array that generated the smallest average error, which corresponds to a minimum in the objective function.

3. The previous step was executed 10 times. Each of them generated a microlens array associated with a local minimum of the objective function. Therefore, the final result consists of 10 different microlens arrays.
4. Each of these arrays was subjected to a comparison test with a rectangular 6x6 array. Both the rectangular and the optimized arrays have a square perimeter with 6mm side and share the same microlens characteristics. The test consisted in estimating and comparing the reconstruction error for an arbitrarily fixed set of 2,000 different aberrated wavefronts within the chosen ocular statistics. This number was chosen arbitrarily, but it is assumed to represent the whole population. It may be important to emphasize that the original paper, which generated the statistical data for ocular aberrations, analyzed 109 human cases (PORTER, GUIRAO, *et al.*, 2001), what is considered a large population in ophthalmological studies. The optimized arrays are then compared to rectangular arrays in terms of:
    a. how smaller the reconstruction errors they produce are and
    b. the percentage of wavefront aberrations for which the optimized array produces a smaller reconstruction error.
5. The array that generates the best results, according to the criteria above, is considered as the best array found.

Although it cannot be concluded that this is the best array that can ever be found for this statistics, it is better than the rectangular one and, as a matter of fact, it is also better than at least other nine non-regular arrays. In practice, however, the obtained array is of great importance, once it can be readily fabricated and used in the optical setup to reduce the total reconstruction error introduced by the system. Whenever a new scenario has to be studied, the optimized array can be specified for the new statistics that describe the typical optical aberrations of interest.

The genetic algorithm configuration used to solve the problem is:

a. Number of elite individuals: 2 out of 250.
b. Crossover fraction, i.e., the fraction of the total population (minus the elite individuals), which will be generated by the crossover operation: 70%.
c. Crossover function: intermediate, which creates children by a random weighted average of the parents.
d. Mutation function: adaptive feasible, which starts with a large mutation possibility in the beginning of the optimization, what means a larger changes in the microlens positions, and then sets it smaller as the process converges to the final solution.

As an additional goal, more than just finding the array geometry that produces smaller reconstruction errors, the work also aimed at searching for arrays with smaller number of microlens that can still generate reasonably small reconstruction errors. Therefore, the whole optimization process just described was carried out for arrays with 10, 16 and 36 circular, plano-convex microlenses, all with the same diameter and building characteristics.

It is important to emphasize that, when 20 Zernike terms are used, the minimum possible number of microlenses in the array is 10. This limitation is imposed by the implementation of the least-squares method in the modal reconstructor, which requires the computation of the Moore-Penrose pseudoinverse of the $2N \times n$ reconstruction matrix $\boldsymbol{B}$ (equation 14). The condition to calculate the pseudoinverse is that the number of Zernike modes (n) and the number of microlenses (N) are related as $2N \geq n$ (WANG and SILVA, 1980).

One may find informative to know about the computation times. The optimization process for one array takes about 37 hours in a computer with an Intel Core2Quad Q6600 processor and with 3GB of RAM Memory. The processing time to find one of the 10 optimal arrays is about 3h40'. The test step for comparison with the rectangular array takes approximately 2h50' for each of the 10 optimal arrays. Therefore, the whole time to generate results to a given number of microlenses is about 2 days and 17 hours. There are many possibilities for improving this time, including code and methodology optimization and the use of C-language GA packages, which are considerably faster than the used toolbox from MatLab©. Those alternatives were not exploited for a matter of focus of the work. That means that the large computation time was not a big problem in itself. In practice, the computation time is not relevant, since the optimized microlens array for each application or wavefront aberrations statistics can be found after running the methodology just once.

Other optimization algorithms could also have been researched and compared in terms of performance and final results. However, also because of a matter of focus, this was not exploited in the present work.

6.1.6. RESULTS AND DISCUSSION

The optimization methodology just described was applied to three cases: arrays with 10, 16 and 36 microlenses. In each case, the output is a group of ten arrays, which are compared to the rectangular one. The choice of the best microlens array among the ones obtained for each optimization process was based on two parameters:

a. The average (over 2,000 wavefront aberrations) percent difference in wavefront reconstruction errors generated by optimized and the rectangular arrays.
b. The percentage of the tested wavefront aberrations for which the optimized array generated a lower reconstruction error than the rectangular.

For each of the three cases, a graph was built to confront the number of wavefront aberrations (among 2000), for which the optimized array generated lower reconstruction errors than the rectangular one, and the average percent difference in the reconstruction error generated by the rectangular and optimized arrays.

The average percent difference $\%x$ is calculated as in equation 29:

$$\%x = \frac{1}{2000} \cdot \sum_{i=1}^{2000} \left(\frac{E_{rect}^{i} - E_{opt}^{i}}{E_{rect}^{i}} \right) \cdot 100 \qquad 29$$

where E_{rect}^{i} is the reconstruction error generated by the rectangular array for the ith aberration and E_{opt}^{i} is the reconstruction error generated by the optimized array for the same aberration.

For example, consider the point marked as a large gray circle in Figure 59, which shows the performance of 10 optimized arrays with 10 microlenses. Its coordinates are $x = -6\%$ and $y = 65\%$. It means that its respective optimized microlens array generated lower reconstruction error for 1300 the 2,000 tested aberrations (65%) and in the average, the reconstruction errors are 6% higher than those generated by the rectangular array. The best array is that represented by a symbol closest to the upper-right corner in the graph.

The point in the graph that corresponds to the larger values in both axes was chosen as the best result found during the optimization process. When there is no point with maximum values in both axes simultaneously, the choice considers first the larger value in the vertical and then in the horizontal axis, in this order. In the case of Figure 59, the point marked as a large gray circle was chosen as the best result. The array corresponding to this point is shown in Figure 60.

For all the other cases (16 and 36 microlens), the best results are also marked as large gray circles in the graphs and the correspondent optimized array is shown immediately below. Results are shown in Figure 59 through Figure 64.

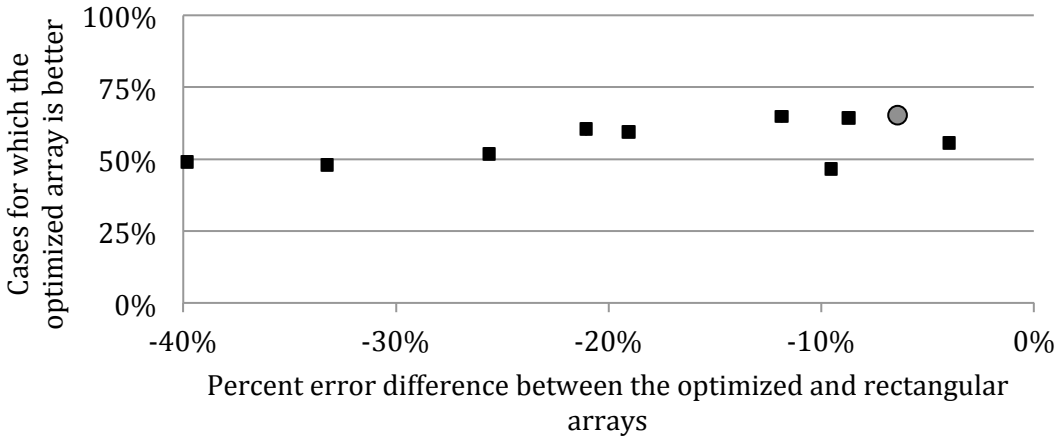

Figure 59 – Performance of the 10 optimized 10-microlens arrays.

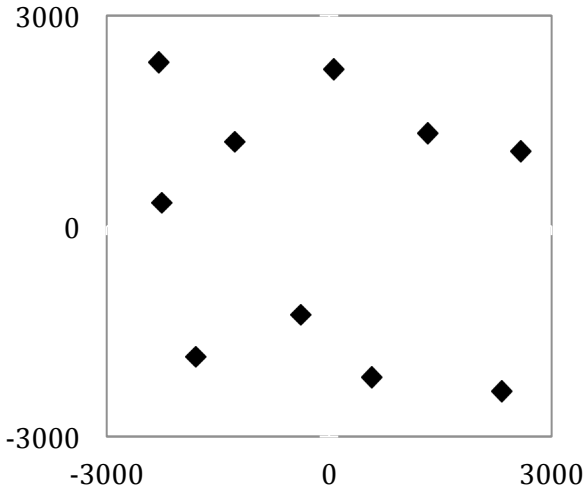

Figure 60 – Optimized 10-microlens best array. Units of the axis values are micrometers.

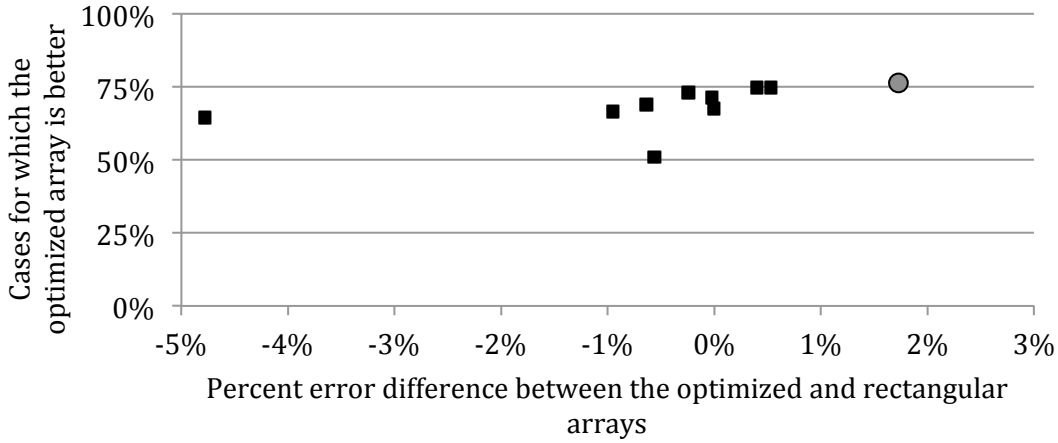

Figure 61 – Performance of the 10 optimized 16-microlens arrays.

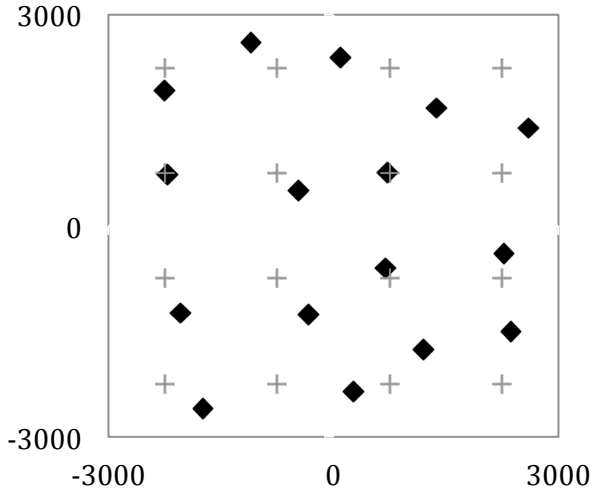

Figure 62 – Optimized 16-microlens best array (black diamond) and rectangular 16-microlens array (gray cross). Units of the axis values are micrometers.

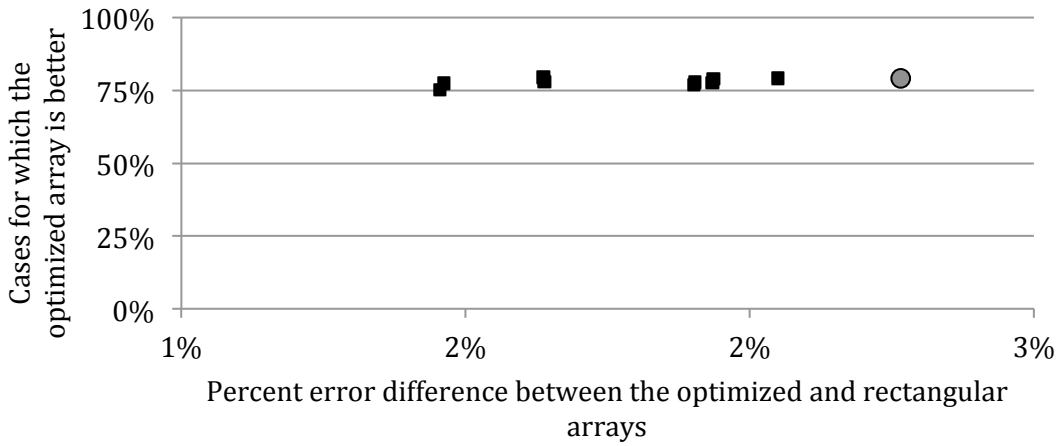

Figure 63 – Performance of the 10 optimized 36-microlens arrays.

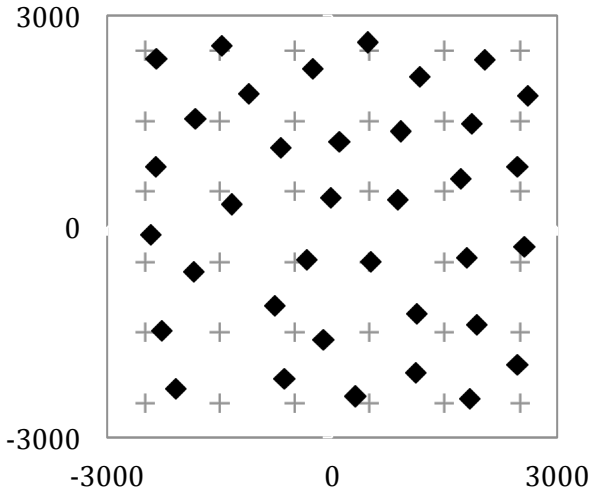

Figure 64 – Optimized 36-microlens best array (black diamond) and rectangular 36-microlens array (gray cross). Units of the axis values are micrometers.

Comparing the best optimized array from each case with the rectangular ones is also of great importance. The 25-microlens rectangular array was also submitted to the test with the 2,000 wavefront aberrations for a matter of comparison of final results. In Table 3, λ is the wavelength (633nm in the present case) of the light beam.

Table 3 – Reconstruction errors generated by optimized and rectangular arrays over 2,000 wavefront aberrations ($\lambda = 633nm$).

Number of microlenses in the array	Average RMS reconstruction error	Standard deviation
10 (optimized)	$1.32\times10^{-8}\lambda$	$2.84\times10^{-8}\lambda$
16 (optimized)	$1.33\times10^{-8}\lambda$	$2.85\times10^{-8}\lambda$
36 (optimized)	$1.36\times10^{-8}\lambda$	$2.90\times10^{-8}\lambda$
16 (rectangular)	$7.37\times10^{-2}\lambda$	$3.80\times10^{-8}\lambda$
25 (rectangular)	$1.36\times10^{-8}\lambda$	$2.91\times10^{-8}\lambda$
36 (rectangular)	$1.37\times10^{-8}\lambda$	$2.93\times10^{-8}\lambda$

These results can also be compared through a graph, as shown in Figure 65.

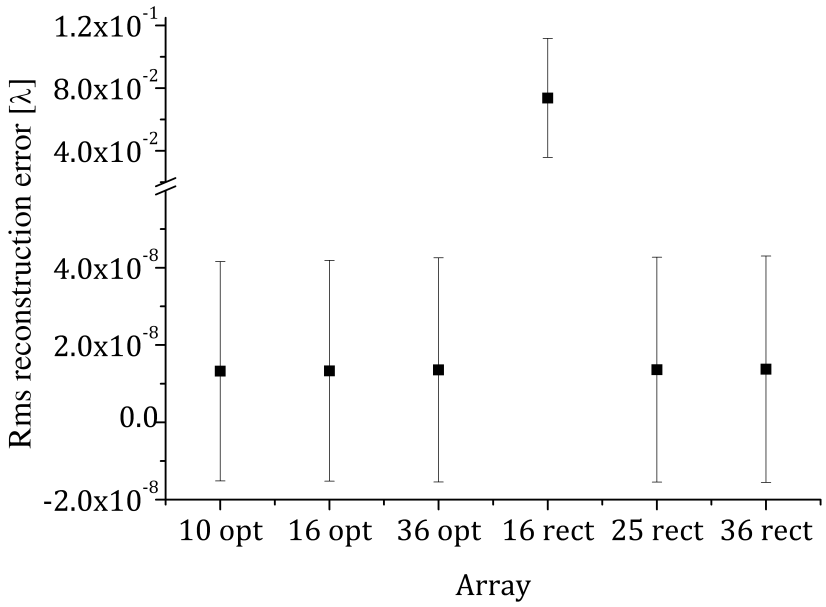

Figure 65 – Comparison of the performance of different microlens-array geometries (OLIVEIRA and DE LIMA MONTEIRO, 2011).

The results show that an optimized array can afford fewer microlenses, maintaining a low reconstruction error. As observed before, the reconstruction error comprises both sampling and numerical errors. Strikingly, through this optimization procedure both the reconstruction error and the number of lenses can be concomitantly reduced. The reduction of the reconstruction error through optimization can be clearly noted in the 16-microlens array. The same order of reduction could not be observed in the optimization of the 36-microlens array, since the rectangular array is already capable of reconstructing the aberrated wavefront with a very low sampling error.

Yoon (2006) present a graph that indicates that the maximum number of Zernike terms that can be reliably reconstructed is approximately the same as the number of microlenses in a regular array (see Figure 66). That means that if 20 Zernike terms need to be calculated, as it is the case in the present work, at least 20 microlenses are required for a reliable reconstruction. Using more than 20 microlenses may decrease the sampling error and, therefore, the reconstruction error, at least until the numerical errors become of the same order as the sampling error. In this sense, a rectangular 16-microlens array cannot reliably reconstruct a wavefront aberration described by 20 Zernike coefficients.

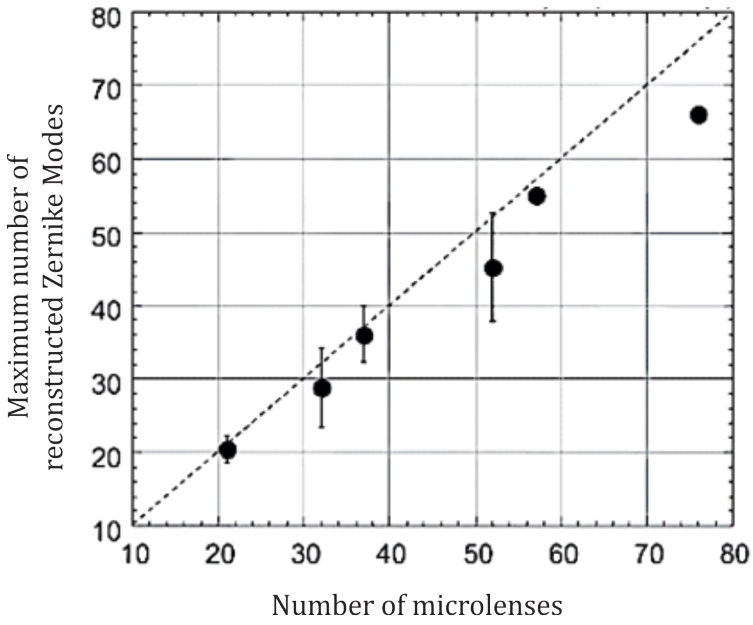

Figure 66 – Maximum number of Zernike terms (or modes) that can be reliably reconstructed for a given number of microlenses using rectangular arrays (YOON, 2006).

The optimization results demonstrate that it is possible to specify the distribution pattern of the 16 microlenses in the array so that it can generate reconstruction errors as low as the ones generated by the 25- and 36-microlens rectangular arrays and moreover, that arrays with even fewer microlenses, such as 10, can also be used to generate small reconstruction errors as the 25- and 36-microlens rectangular arrays.

An array with fewer microlenses yields less data from the wavefront sensor, reducing processing time and round-off errors. Also, for a fixed array area, the microlens diameter can be maximized, improving the signal-to-noise ratio in the photodetection step and reducing the sizes of the resulting spots at the lenses foci. Using the fabrication process proposed by D.W. de Lima Monteiro *et al.* (2003), even for non-regular lens centers, a 100% array fill factor can be maintained. Nevertheless, any modification of lens diameter and perimeter can alter the array performance and needs to be carefully assessed. The size of the microlens does not affect the sampled spatial-frequency spectrum, but influences the modulation transfer function (MTF) of the array, i.e. how accurately the amplitude of each frequency component is reproduced.

Arrays with fewer microlenses can also produce benefits when an array of PSDs is used as detector. Since the number of PSDs is the same as the number of microlenses, the unused area surrounding each PSD on the silicon wafer is larger, and can be used to:

a. accommodate larger integrated processing electronics per PSD, to be used to improve response uniformity among detectors of the same chip and/or increase the signal-to-noise ratio; and
b. allow the use of larger light spots, so that microlenses with larger focal distance could be used, what makes the design of the microlens array more flexible, considering the etching technique used in the fabrication process (DE LIMA MONTEIRO, AKHZAR-MEHR, *et al.*, 2003).

It is also important to compare the arrays considering their impact on the numerical calculation of the pseudoinverse of the reconstruction matrix $\boldsymbol{B}$ (equation 14). This matrix is directly affected by the microlens positions in the array, since it contains the first derivatives of the Zernike functions evaluated at the respective sampling regions. The pseudoinverse calculation requires the inversion of the square matrix $\boldsymbol{B}^T\boldsymbol{B}$, which should be well conditioned. As pointed out by Navarro *et al.* (2009), the 2-norm condition number[23] can be computed to check the numerical stability of the inversion of a matrix. If the inverse of the condition number is used, it is always between 0 and 1. A condition number close to 1 means the matrix is well conditioned. Moreover, Navarro *et al.* (2009) states that the rank[24] of the matrix to be inverted must equal the number of Zernike terms M to guarantee the matrix is not singular, i.e. $Rank(\boldsymbol{B}^T\boldsymbol{B}) = 20$. In this work, the condition number and the rank of the matrix $\boldsymbol{B}^T\boldsymbol{B}$ were calculated for the 10-, 16- and 36-microlens optimized arrays and for the 16- and 36-microlens rectangular arrays, using the software MatLab© (R2008a). The results are shown in Table 4.

Table 4 - Condition number and rank of the matrix $\boldsymbol{B}^T\boldsymbol{B}$.

Number of microlenses in the array	Condition number	Rank
10 (optimized)	8×10^{-4}	20
16 (optimized)	2×10^{-3}	20
36 (optimized)	7×10^{-3}	20
16 (rectangular)	2×10^{-17}	18
36 (rectangular)	1×10^{-2}	20

The rank of the 16-microlens rectangular array was 18, what means that matrix $\boldsymbol{B}^T\boldsymbol{B}$ is singular or close to singular for this case. This indicates that this array is not appropriate to sample Zernike polynomials. On the other hand, the rank of the other arrays, including the 16-microlens optimized array, was 20, which equals the total number of used Zernike terms. This guarantees that the matrix is not singular when these arrays are used and therefore the matrix $\boldsymbol{B}^T\boldsymbol{B}$ can be inverted. The values of condition numbers of all the arrays, except for the 16-microlens rectangular one, indicate the respective matrices are well conditioned. That guarantees the optimized arrays preserves accuracy and numerical stability in the wavefront reconstruction (NAVARRO, ARINES and RIVERA, 2009).

Another important study is the analysis of the influence of rotation on the sampling performance of the arrays. This is particularly important in practice, since the relative orientation of the array with respect to the aberration is often unknown.

---

[23] The 2-norm condition number associated to a system of linear equations of the type $Ax = b$ describes the rate at which the solution x changes due to a small change in b. Therefore, a large condition number means that a small error in the calculation of b may cause a large error in the estimation of x, which is given by $x = A^{-1}b$. In this work, the calculation of the 2-norm condition number was performed with the software MatLab© (R2008a), with a built-in function to this purpose.

[24] The rank of a matrix is an estimate of the number of linearly independent rows or columns of a matrix. If the rank is equal to the number of variables, then the linear system $Ax = b$ is determined and, therefore, admits solution, provided that matrix A is not singular nor nearly singular. Otherwise, the linear system admits no solution or various solutions. In this work, the calculation of rank was performed with the software MatLab© (R2008a), with a built-in function to this purpose.

To test the influence of rotation over the reconstruction error generated by each array, an algorithm was written to rotate the array, about its central point, in steps of 10° and calculate the reconstruction error over the set of 2,000 aberrations for each angle. The mean reconstruction errors were calculated and are shown in Figure 67.

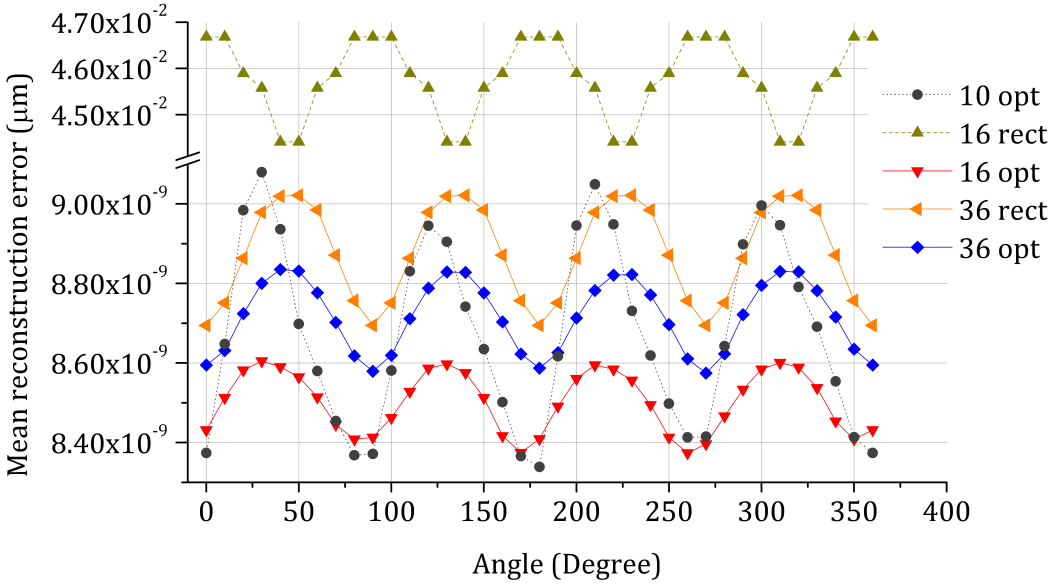

Figure 67 – Influence of rotation of the microlens arrays on the mean reconstruction error for each array. In the legend, the numbers represent the number of microlenses in each array and the letters represent the array geometry: 'rect' stands for rectangular and 'opt', for optimized.

The error bars are not shown in Figure 67 for a matter of scale. If they were shown, it would not be possible to see the variation that occurs in the mean values, as they are themselves of the same order of magnitude as the corresponding average values. An equivalent graph, containing the error bars is shown in Figure 68.

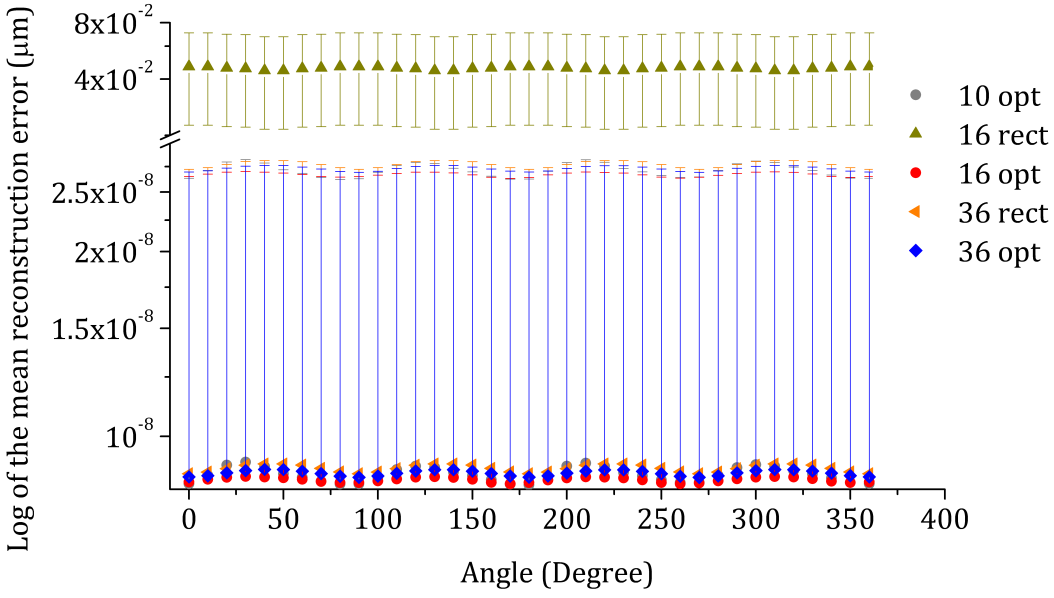

Figure 68 – Influence of rotation of the microlens array on the reconstruction error calculated in a set of 2,000 wavefront aberrations.

It can be noted in the graph of Figure 67 that the variation in the mean reconstruction error is smaller than $1\times10^{-3}\lambda$ ($\lambda = 633nm$) for each array, except for the 16-microlens rectangular array. Therefore, it can be concluded that the performance of the optimized arrays are not significantly affected by rotation.

The oscillations observed in the mean reconstruction errors for each array suggest the problem has a certain degree of symmetry of 90°, since the errors are minimum for angles multiple of 90°. This symmetry is perfect for rectangular arrays. Actually, the oscillations are observed because the Zernike terms present symmetry to rotation, which can be easily seen in Figure 69. Most of the used Zernike terms can be obtained by a 90°-rotation of another one. It is the case of the pairs Z_3^{-3} and Z_3^3, Z_3^{-1} and Z_3^1, Z_5^{-1} and Z_5^1, Z_5^{-3} and Z_5^3 and Z_5^{-5} and Z_5^5. Some other pairs are obtained by 45°-rotation of the terms, as, for example, the terms Z_2^{-2} and Z_2^2.

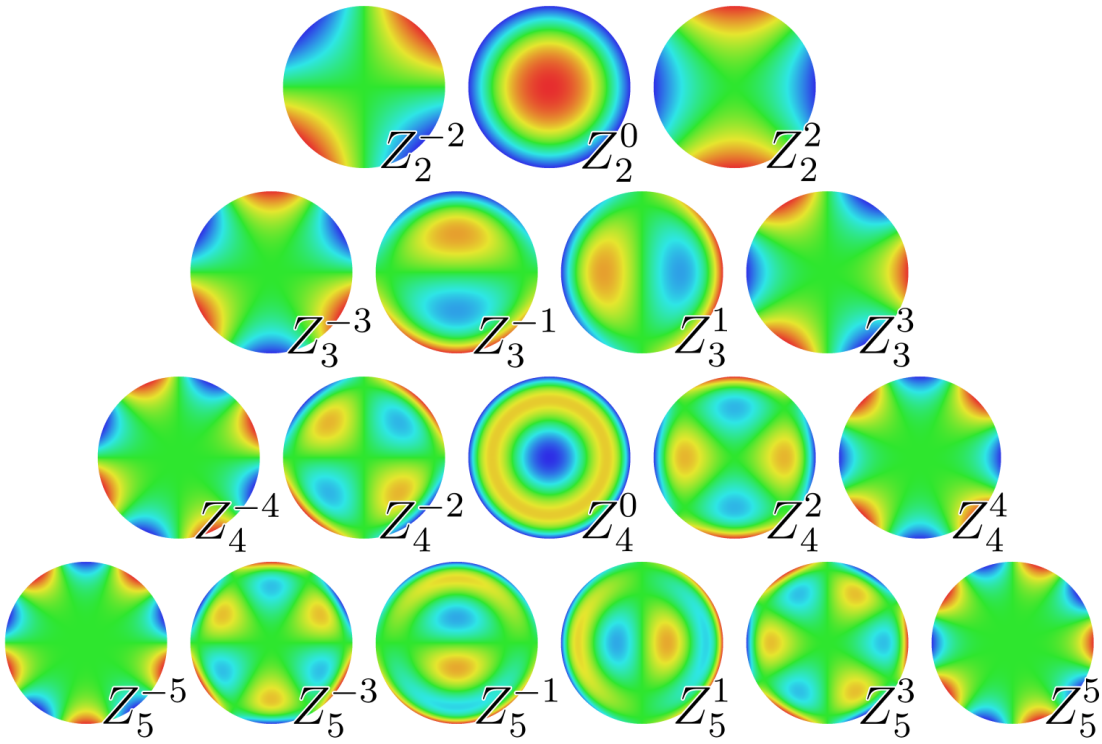

Figure 69 – Plane view of Zernike terms. The piston, tip, tilt (not shown) and defocus terms were not taken into account in the optimization.

6.2.FABRICATION OF MICROLENS ARRAYS

After finding the optimized geometries for the microlens arrays, they were fabricated using the method proposed by (DE LIMA MONTEIRO, AKHZAR-MEHR, *et al.*, 2003) and described in section 4.4.1. The arrays were fabricated in the clean room of the Physics Department of the Federal University of Minas Gerais.

Before fabricating the arrays, a rescaling had to be performed. The initial purpose was to model the array dimensions according to the human eye pupil diameter commonly used in aberrometry procedures, which is 6mm. The array should be inscribed into the light-beam

transversal section and should have, therefore, a lateral dimension of 4,242.6μm. Nevertheless, the lateral dimension of the arrays was erroneously set to 6mm. The light-beam diameter was automatically calculated in the H-S algorithm to circumscribe the microlens array. Hence, the presented simulation results were carried out with a light-beam diameter of 8,485.28μm, which was eventually different from the planned 6mm.

The dimensions of the arrays and microlenses were rescaled to a factor of $\sqrt{2}$. Therefore, the new array dimension is 4242.6μm and the new microlens diameter is 530.3μm. The microlens diameter and center positions were rescaled in the same manner. As both light beam diameter and array dimensions were rescaled, the expected results were not affected.

The fabrication of the microlens arrays consists of two basic steps: fabrication of the silicon mold and replication of the molds on photopolymer by casting. The chosen silicon wafer, illustrated in Figure 70, is a standard microelectronic-graded polished (100) wafer, with a thickness of 524μm and a diameter of 4 inches. The wafer contained a 400nm thick layer of silicon nitride (SiN) on its bottom and another 120nm thick layer of silicon dioxide (SiO_2) placed on the upper side and on the bottom side, between the SiN layer and the wafer. The SiN layer is of great importance because it protects the bottom side of the silicon wafer from being etched by the potassium hydroxide (KOH) and by HF used to transfer the aperture pattern from the photoresist to the SiO_2. The SiO_2 on the bottom of the wafer is used to promote adhesion of the SiN. On the other hand, the SiO_2 on the upper side plays an important role when the inverted pyramids are created, as will be described below.

Figure 70 – Illustration of the silicon wafer used in the fabrication of the microlens array.

Three 15x15mm samples were obtained by cutting the silicon wafer with a diamond-point pen. In each of these samples, the molds for the 10- and 16-microlens optimized arrays and 16- and 36-microlens rectangular arrays were organized in a 2x2 grid. The three samples were submitted to exactly the same process to produce three equal molds.

Before any procedure can be done, the samples need to be cleaned. This is done in a 4-step process. Initially, the samples are immersed in acetone, to remove organic impurities. Then the acetone residues are removed by dipping the samples in isopropanol (isopropyl alcohol). The isopropanol is then removed by immersion in deionized water. Finally, the samples are dried in a hot plate for 10 minutes at 115°C. All the three immersion steps are carried out under ultrasound for 5 minutes each.

The first step to fabricate the molds consists in producing the inverted pyramids with KOH etching, as described in section 4.4.1. The positions of each pyramid are determined by the

lithographic pattern, which describes the desired microlens-array geometry. This pattern is first transferred to the SiO_2 layer, through HF etching, forming openings in the exact position of the microlenses. The remaining SiO_2 layer protects the silicon surface from KOH etching. Therefore, when the silicon wafer is immersed in KOH solution, only those regions under the openings are etched. The final result is the desired set of inverted pyramids.

Initially, a layer of positive photoresist[25] is deposited on top of the SiO_2. The used photoresist was Microposit S1813. This is done with the use of a spinner, which rotates the sample for 5 seconds at 900rpm (rotations per minute) and then at 4500rpm during 40 seconds to form a homogenous layer with thickness of the order of 1μm. Then, the photoresist must undergo a curing step, which consisted of placing the sample in a hot plate for 1 minute at 114˚C.

The lithography was performed using a laser writer (LW 405 – Microtech). The laser writer is used to write the desired pattern on the photoresist layer, without the need for any mask to determine the regions that must be exposed to light and the ones that must not. The equipment uses a translational system to scan the sample and expose precisely the determined regions with a GaN laser (wavelength of 405nm). The desired pattern is produced in a computer algorithm, which was developed by D. W. de Lima Monteiro. This algorithm produces an image file containing a map of the points where the laser must impinge and also returns the necessary lateral dimension of the inverted pyramid (d_0) to form the round cavity with the desired diameter (D). In this case, the obtained value was $d_0 = 8.75\mu m$ for a $D = 530.3\mu m$.

The sample with the photoresist layer was then placed inside the laser writer and the whole exposition process was carried out automatically. It took slightly more than 1 hour for the equipment to complete the process for one sample. After the exposure, the sample was developed through immersion in the Microposit MF321 developer for 60 seconds. As the resist is positive, those regions that were exposed to the laser become soluble in this developer. Therefore, the final result is a pattern of filled circles on the resist. Each circle corresponds to an opening that gives access to the SiO_2 layer. Figure 71 shows a photo of one of the samples right after the development step. The opening diameter was approximately 10μm, which was slightly larger than the originally planned one: 8.75μm.

To transfer the pattern from the photoresist to the silicon dioxide layer, the sample must undergo an etching step to remove SiO_2. The photoresist protects the silicon dioxide layer from etching. Therefore, only the regions determined by the openings are etched. The etching step of the SiO_2 was performed by immersing the sample in HF buffer solution for 2 minutes (OLIVEIRA COSTA, 2010). After etching the silicon dioxide, the remaining photoresist layer has to be removed. This was done through immersion of the samples in the Remover PG (Microchem), which is a photoresist remover, during 5 minutes. Then the samples were submitted to acetone, isopropanol and deionized water, in this exact sequence for also 5 minutes each. All this process was carried out under ultrasound.

[25] A positive photoresist is a light-sensitive polymer that becomes soluble in photoresist developer when exposed to light.

Figure 71 – Pattern transferred to the photoresist layer. The lateral dimension of the opening is about 10µm.

After removing the photoresist layer, the samples are ready for being submitted to anisotropic KOH etching, which is responsible for generating the inverted pyramids. Only those regions corresponding to the openings of SiO_2 are etched. The samples were then immersed in a KOH 33% aqueous solution during 4 minutes. This is done at 92°C with magnetic agitation. The result is shown in Figure 72. The lateral dimension of the pyramid is of the order of 11µm. It is important to emphasize that the pyramid basis is square, although the opening has a circular contour. This circular shape of the opening is important because the inverted pyramids are always formed with one side parallel to the plane (110).

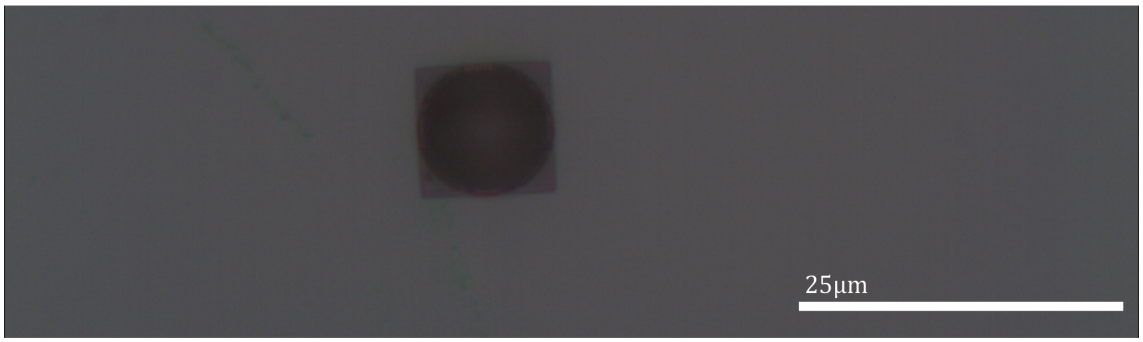

Figure 72 – Inverted pyramid formed after KOH etching.

After forming the inverted pyramids, the remaining SiO_2 was removed using again an HF solution. To guarantee no residues were left behind, the samples were immersed in the HF solution for 5 minutes. Then the samples were washed in deionized water.

The last step in producing the molds consists in the KOH etching of the unprotected silicon surface. As already described, KOH etches the planes (100), (111) and, at a faster rate, the plane (411), along with other high-Miller-index planes, which might be the mechanism responsible for rounding the profile of the pyramids. The sample was immersed in a KOH 33% solution during 2 hours and 47 minutes. This time was calculated based on the etching depth (h) of the substrate and etching rate (r) of plane (100). The required etching depth is 300µm and was obtained through equation 16 and the values of d_0 and D used in this work. The etching rate of the (100) plane is approximately 1.8µm/min. The ratio between h and r gives the total etching time mentioned. This etching is also performed at 92°C with magnetic agitation.

Figure 73 shows some photographs of the molds produced in this work. Some patterns comprising significantly smaller cavities can also be observed in the images. These

patterns were designed to allow visual inspection of each array perimeter and also to mark the orientation of the arrays.

Note that the final diameter of the cavity (795μm) was larger than the planned diameter for the microlenses (530μm). It can be noted, for instance, in Figure 73b that there was a superposition of the microlenses in the array with 36 microlenses. Besides this difference, it was also observed some imperfections in the molds (as in the bottom left corner of Figure 73d and e) and a variation in the diameters of the cavities, which range typically from 600μm to 850μm.

Several reasons may be associated with these problems. One of the main causes can be associated to configuration and/or calibration problems of the laser writer. Note in Figure 71 that the lateral dimension of the opening was about 10μm and it was expected to be 8.75μm. There are many different variables that must be set in the laser writer and a small variation in one of them may cause unexpected results. For instance, a deviation in the focus adjustment of the equipment increases the light spot size that impinges in the sample, exposing therefore an area larger than planned. Thus, the openings obtained after photoresist development are also larger.

Another possible problem may be related to the KOH etching, especially during the formation of the rounded cavities. Variations in the solution concentration, for instance, cause the etching rate of the different planes to change and consequently alter the final result for the same etching time. The etching rate can also be affected by insufficient solution agitation and variations in temperature, which, incidentally, must be very well controlled in the range of $\pm 1^{\circ}C$.

In general, it is very difficult to point out one exact cause for the deviations in the final results, since the number of variables in the whole process is very large. Now, that the whole procedure has already been carried out once, some limitations and critical steps have been mapped. It is left as a prospective work to elaborate, based on these results, a control procedure to identify all possible error sources during the fabrication process.

The last step to produce the microlens arrays is to replicate the fabricated molds. In general terms, a liquid photopolymer is placed on top of the mold and then is cured in ultraviolet (UV) light. Then the polymerized material is detached from the molds and constitutes the final microlens array.

Initially, the molds are coated with a PMMA (Poly Methyl Methacrylate) layer. The used PMMA is the 950K-C2 from Microchem. A spinner rotates the mold with a drop of PMMA at 600rpm during 7 seconds and subsequently at 3000rpm at 40 seconds. According to the resist datasheet, the resultant PMMA film must have a thickness of about 200nm. The reason for using this PMMA film was to reduce adhesion of the photopolymer to the silicon mold, so that it required smaller strength to be detached and hence the surface quality could be preserved.

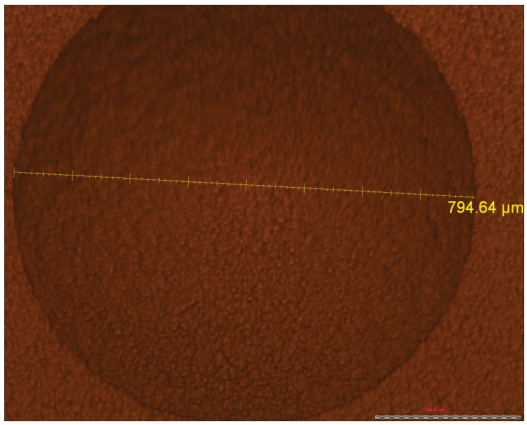

(a) A round cavity with diameter of ~795µm

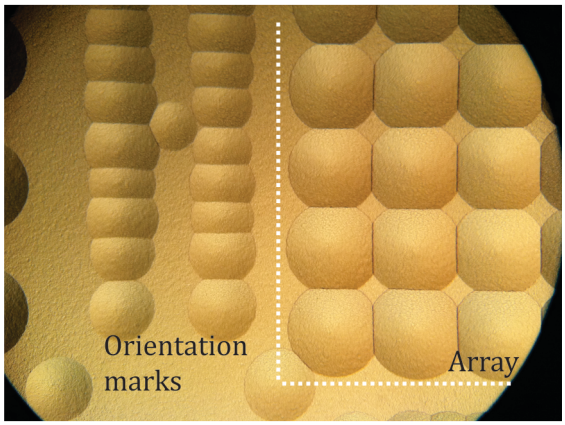

(b) 36-microlens rectangular array

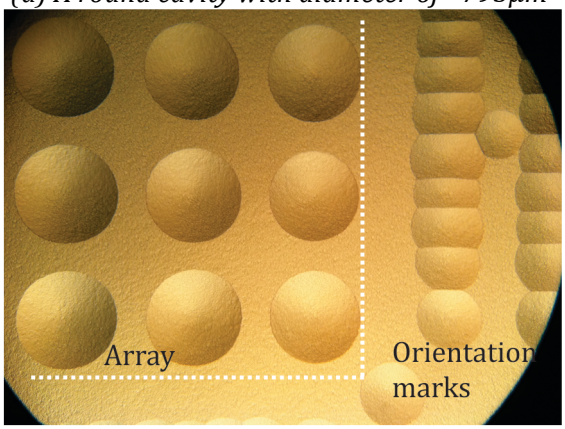

(c) 16-microlens rectangular array

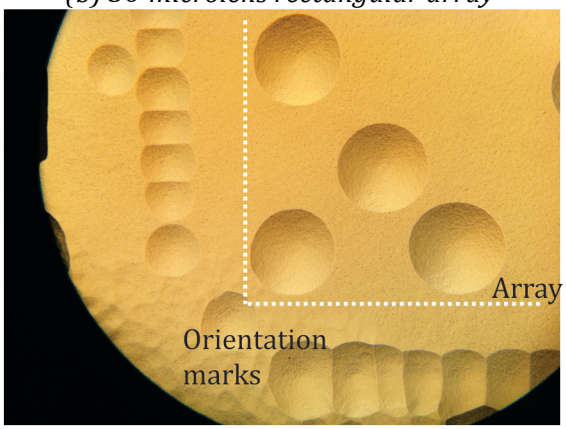

(d) 10-microlens optimized array

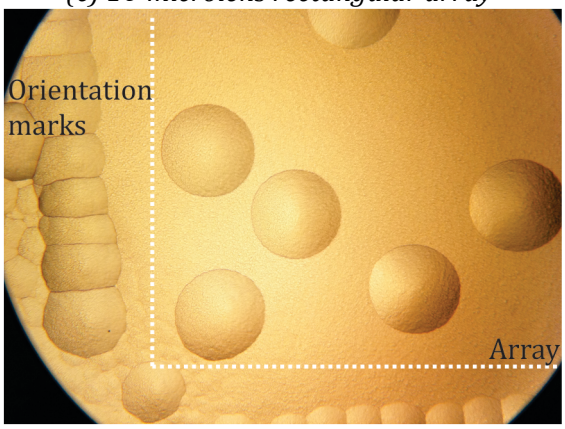

(e) 10-microlens optimized array

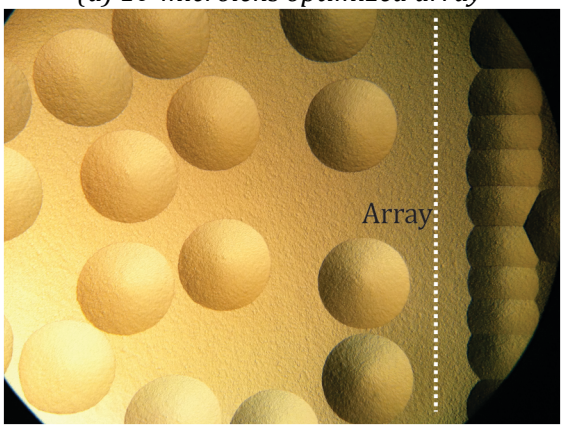

(f) 16-microlens optimized array

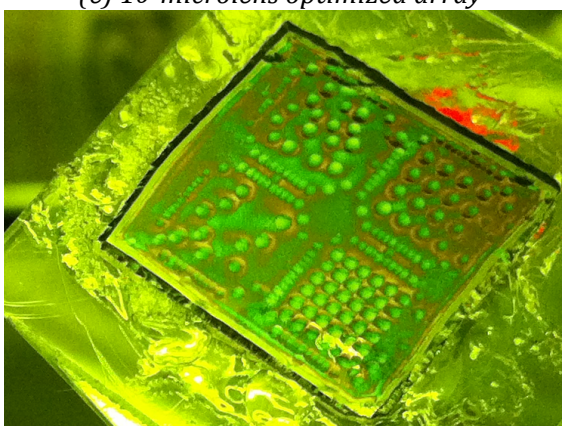

(g) Sample with the 4 arrays

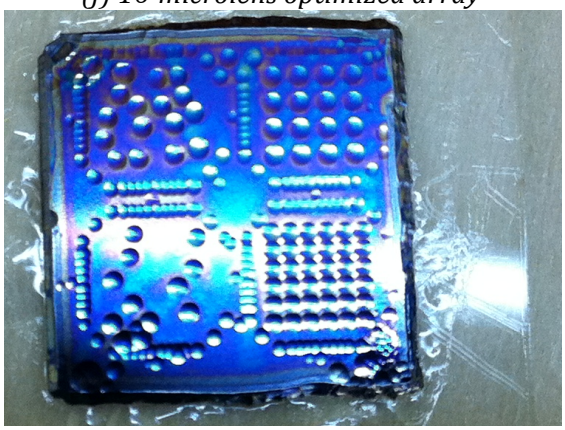

(h) Sample with the 4 arrays – another view

Figure 73 – Microlens-array molds produced.

After the PMMA coating, the molds surface were covered with a liquid photopolymer. The one used in this work was the NOA Optical Adhesive 61, from Norland Products Inc. This is a liquid, colorless photopolymer curable under UV light. Its refractive index is 1.56. After covering the molds with the optical adhesive, a cover glass (the same commonly used with microscopes) was placed on top without pressure.

The molds were then submitted to UV light during 20 minutes (illustrated in Figure 74a). After this time, the photopolymer became rigid. The cover glass was then carefully detached from the mold and the microlens array pattern was transferred to the optical glass. The used UV light was the model BONDWand, from Electro-Lite Corporation, with an output of 10mW/cm² at 350nm.

Figure 74b shows the process of detachment of the cover glass together with the optical adhesive, where the array pattern is recorded. Note that a defined approximately circular area is formed in the center of the mold. This corresponds to a region where the optical adhesive is still in contact with the silicon mold. In the whiter area, the detachment has already occurred. This process was carried out slowly and carefully.

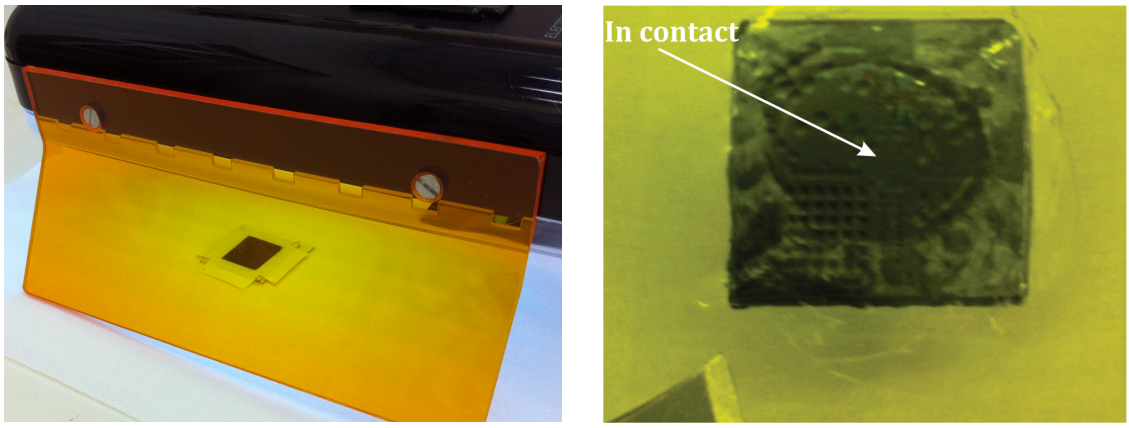

(a) *(b)*

Figure 74 – Replication of the microlens arrays: a) UV curing of photopolymer and b) detachment of the cover glass with the optical adhesive.

Figure 75 shows some photographs of the fabricated microlens arrays seen from the microscope. Figure 76 show some pictures of the fabricated microlens arrays obtained through Scanning Electron Microscopy (SEM). These images were produced at the Microscopy Center of the Federal University of Minas Gerais.

In Figure 75, the four arrays shown are of the same sample. The black line in 16-microlens optimized and 36-microlens rectangular arrays is a fissure generated when detaching the cover glass from the mold. Some imperfections at the borders, especially in the top left corner of the 10-microlens array, were generated also by the detachment process. Although it is done carefully and slowly, sometimes the necessary strength may be high enough to damage the structures. An interesting prospective work is to test different substances in the place of PMMA, to prevent adhesion of the optical adhesive while preserving the optical surface quality.

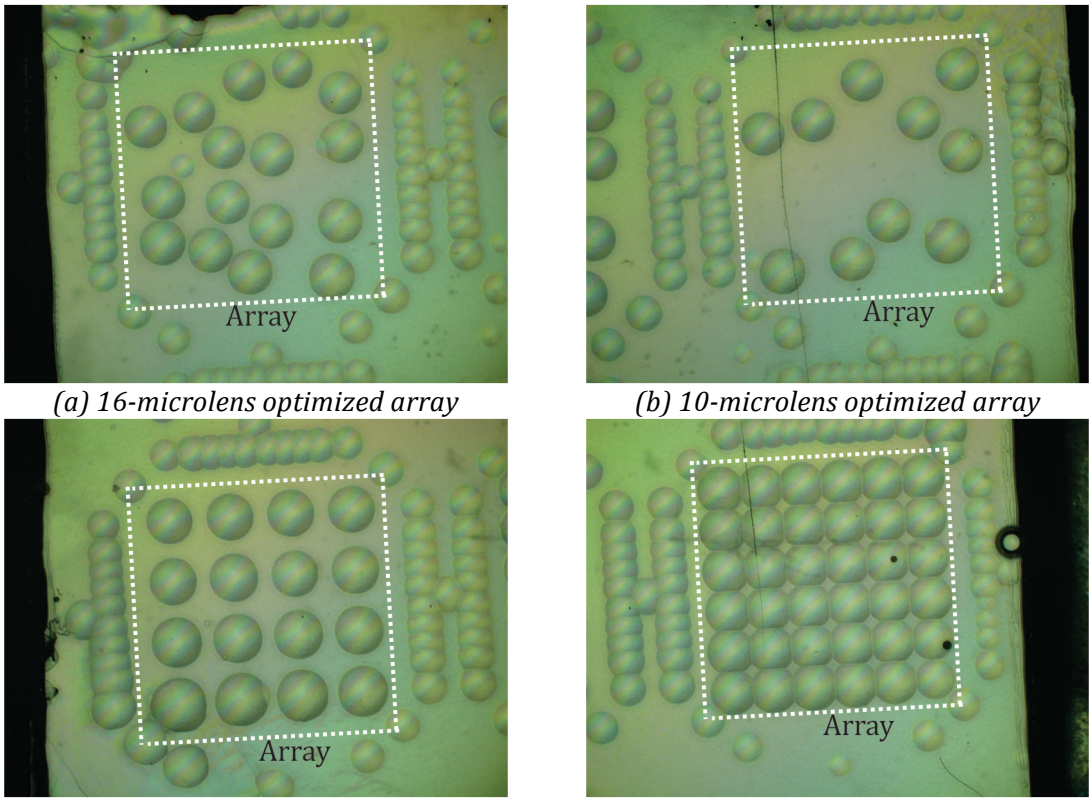

(a) 16-microlens optimized array *(b) 10-microlens optimized array*

(c) 16-microlens rectangular array *(d) 36-microlens rectangular array*

Figure 75 – Fabricated microlens arrays.

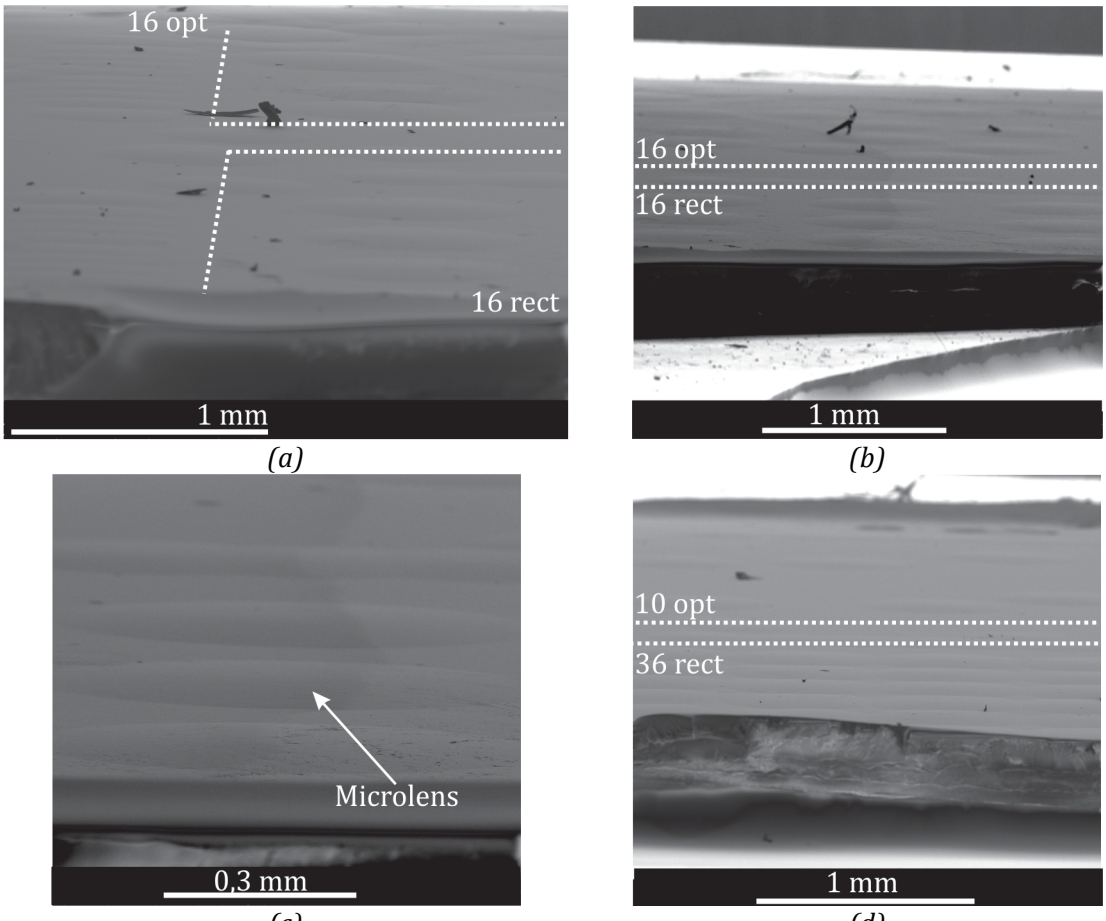

(a) *(b)*

(c) *(d)*

Figure 76 – Microlens arrays imaged with SEM.

In Figure 76a, it can be seen part of the 16-microlens rectangular array in the bottom of the sample and the 16-microlens optimized array on top. The same image is shown in Figure 76b, but with less zoom. In Figure 76c, some microlenses from the 16-microlens rectangular array are shown in detail. At last, in Figure 76d, it can be seen in the bottom of the sample the 36-microlens rectangular array and, in the top, the 10-microlens optimized array. To distinguish the lenses on the substrate, it was necessary a very large view angle, since the lens sagitta is much smaller than its diameter. Therefore, it is possible to see, especially in parts b and d of Figure 76, the border of the sample. In some regions of these images, the border is lifted up, due to damages, and prevents one from seeing some of the microlenses. If seen on microscope, as in Figure 75, it can be noted that the microlenses were not affected.

6.3. TEST OF THE FABRICATED MICROLENS ARRAYS

A simple test was carried out to observe the focusing ability of the microlens array. Figure 77 shows the image generated by the 16-microlens rectangular array projected on a piece of white paper, which is placed in the proximity of the focal plane of the lenses. The paper is tilted in relation to the light beam transversal plane, as shown in Figure 78. Note in Figure 77 that the focused spots are much brighter than the background. Therefore, if the light beam intensity is low, the background may not be visible whereas the light spots generated by the microlenses can still be perceived in the detector. In the case of an array with 100% fill-factor, all optical power is concentrated on the spots, naturally eliminating background illumination.

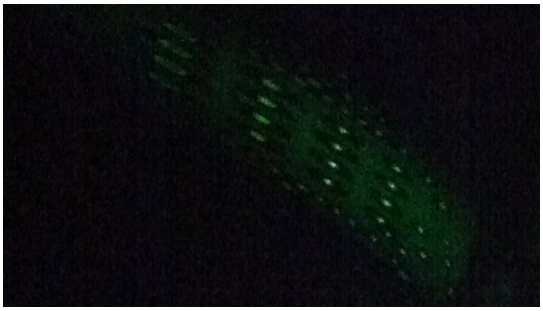

Figure 77 – Image generated by the 16-microlens rectangular array in the proximity of the focal plane.

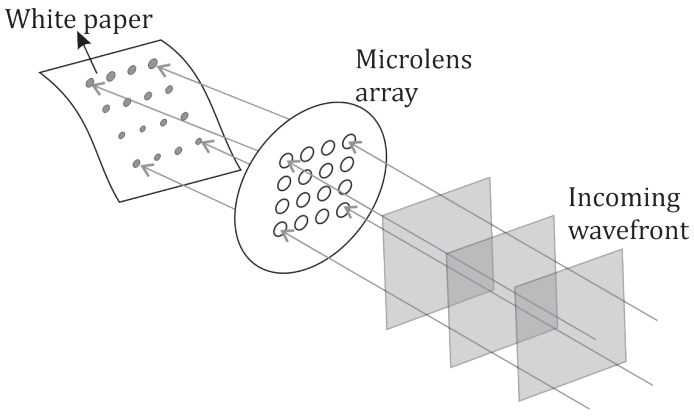

Figure 78 – Schematics of the optical setup for the observing the focusing ability of the array.

To test the performance of the arrays, they were used to measure an optical aberration. All the four fabricated arrays were tested, and the results were compared to those of a commercial 127-microlens hexagonal array from OKO Technologies (OKO TECHNOLOGIES, 2006) which is available at the OptMA[lab].

An optical setup was developed in the OptMA[lab] by Amaral (2011) to measure intraocular lens (IOL) aberrations using the Hartmann-Shack method. This optical setup, with few modifications, was used to test the microlens arrays. A schematics of the adapted optical setup is shown in Figure 79, while Figure 80 shows a picture of the setup. A CCD camera (µEye UI2210-SE-M-GL – Sony) is used with a 127-microlens hexagonal array attached to it. It uses the FrontSurfer© software from OKO Technologies to capture the images from the camera and return the final result with the values of the Zernike terms.

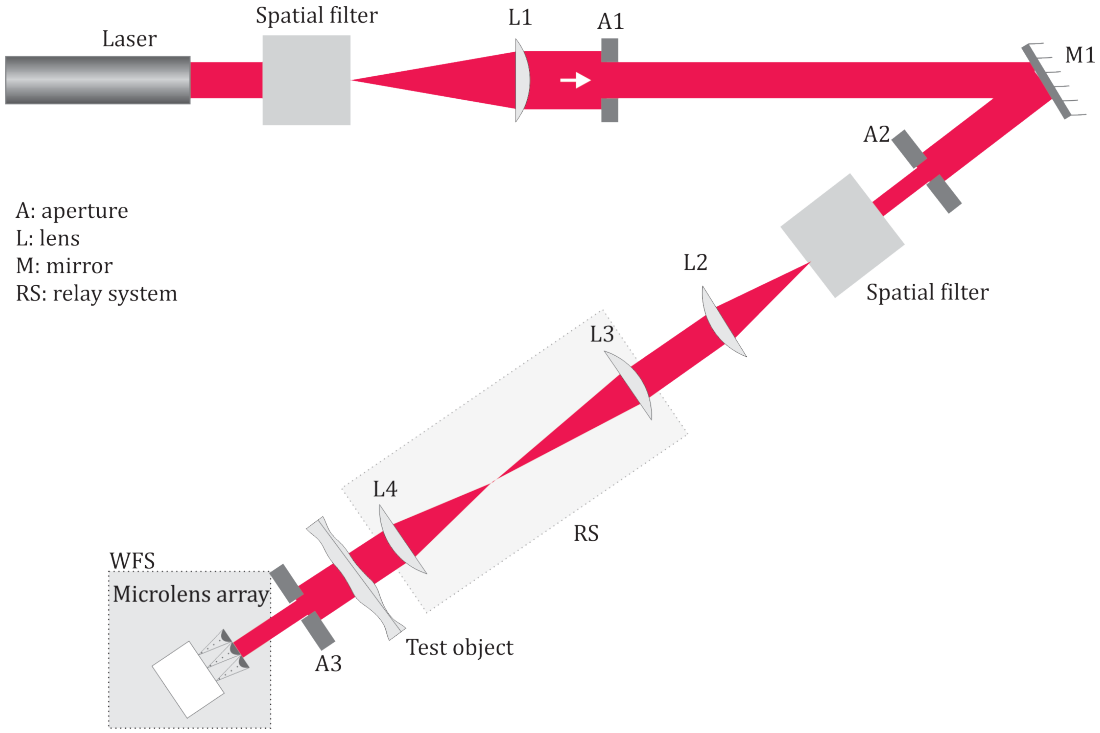

Figure 79 – Optical setup designed to characterize intraocular lenses.

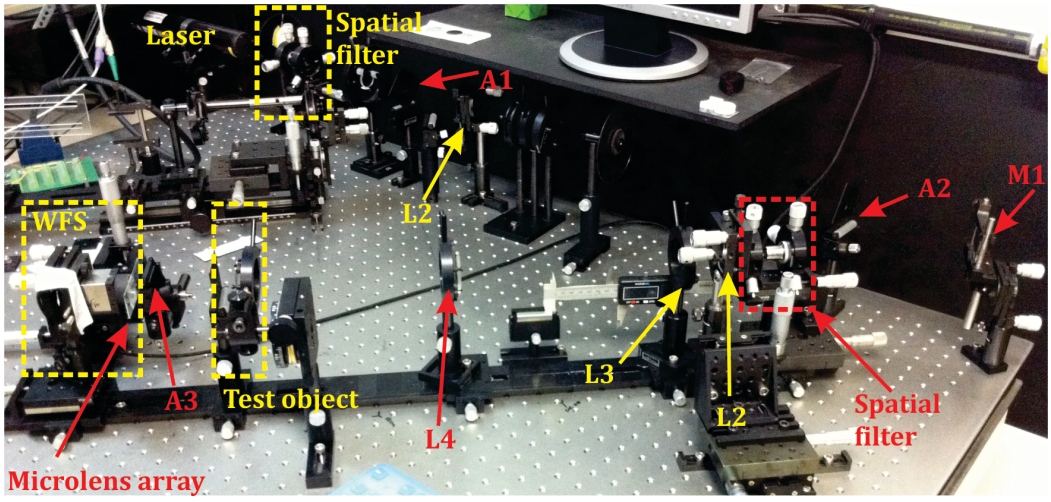

Figure 80 – Adapted optical setup to test the microlens arrays.

The modifications consisted in placing one support for a glass containing the aberration to be measured and another for the microlens array fixation. This last support had micrometric position-adjustment.

To compare all the arrays, an arbitrary optical aberration was produced. A drop of the optical adhesive used to fabricate the arrays was placed on top of a clean cover glass. This drop was spread out over the surface of the cover glass arbitrarily and then was cured with UV light. After curing, the cover glass was positioned in the optical setup to measure the aberration it introduced in the light beam. The measurement was carried out with collimated light and the 127-microlens hexagonal array, with which the whole setup had already been calibrated. This was done a few times until the obtained wavefront aberration had Zernike coefficients close to the ones predicted by the used aberration statistics of the human eye (PORTER, GUIRAO, *et al.*, 2001). The chosen aberration has the Zernike coefficient values shown in Figure 81. These values are the result of an average performed over 10 measurements of the same aberration. The standard variation is too low to be shown in the picture scale.

An improvement of this test consists in using a known optical aberration, instead of an arbitrary one, which is designed to match exactly the desired ophthalmic statistics. This is part of a near future work, in which the test optical aberrations will be fabricated using a technique of micromachining to generate arbitrary polynomial surfaces (DE LIMA MONTEIRO, AKHZAR-MEHR, *et al.*, 2003).

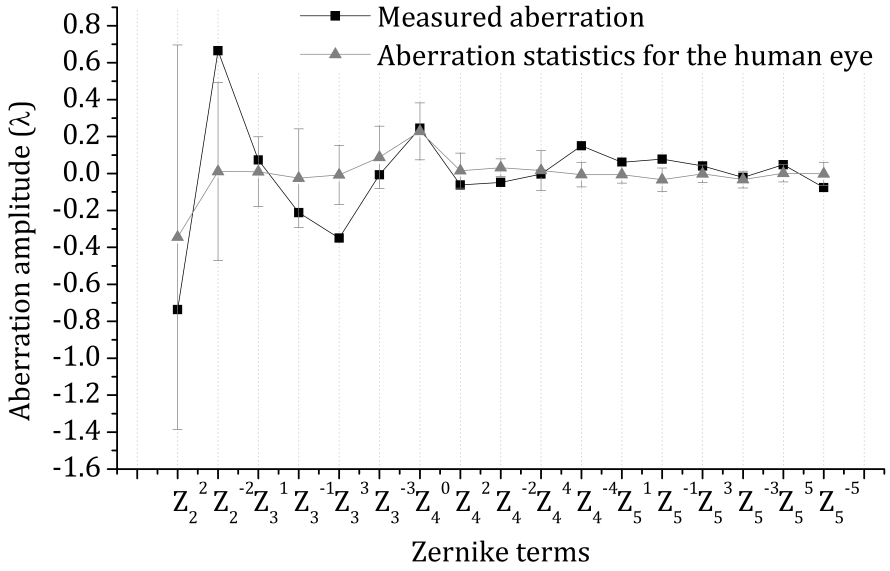

Figure 81 – Arbitrary wavefront aberration chosen to test the arrays.

It can be noted in Figure 81 that 13 Zernike terms of the arbitrary aberration had values within the variation range of the used ophthalmic statistics. From the four remaining Zernike terms, two had values very close to the limits of the variation range of the used statistics. The values for the terms Z_2^{-2} and Z_3^3 were the most deviating ones and their difference to the limiting value of the respective term from the statistics was lower than $\lambda/5$. This was considered a sufficiently small deviation, since, for instance, the typical

standard quality parameter for commercial optical components such as lenses or mirrors is $\lambda/10$. Therefore, the found aberration was considered sufficiently compatible with the used ophthalmic statistics and hence was used to test the fabricated microlens arrays.

Figure 82 shows the hartmograms generated by the fabricated arrays for the chosen aberration.

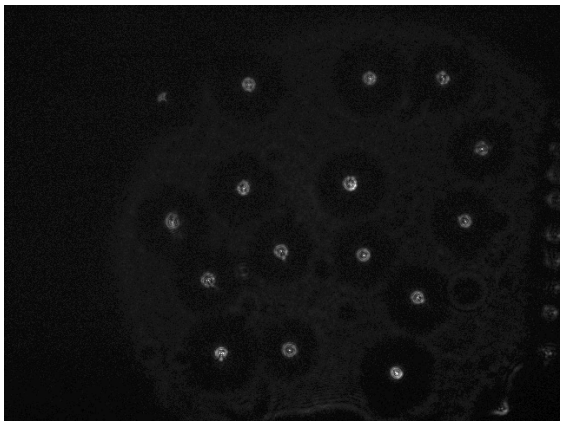

(a) 16-microlens optimized array

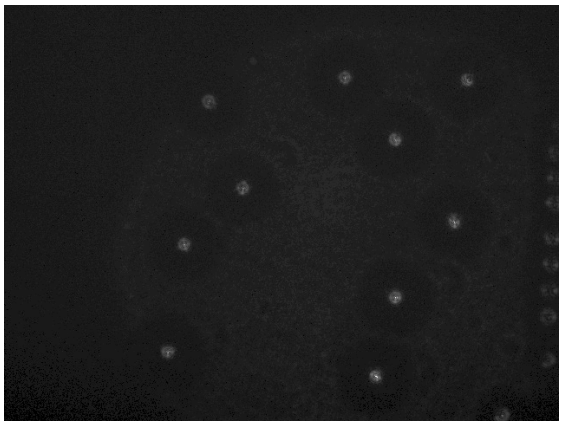

(b) 10-microlens optimized array

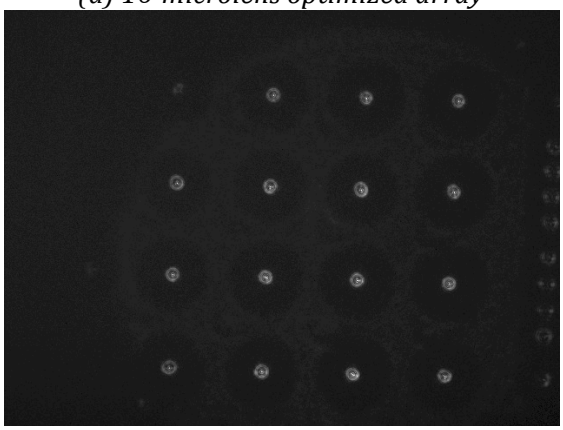

(c) 16-microlens rectangular array

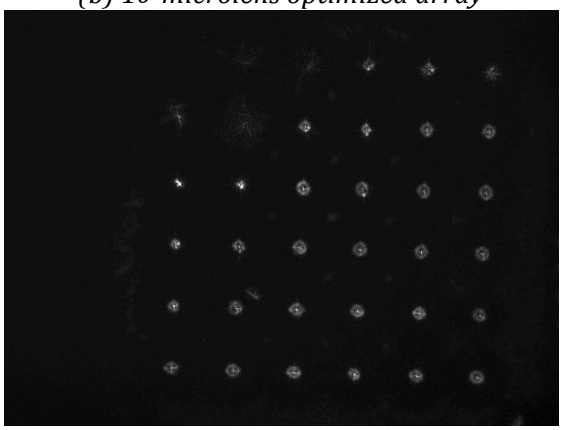

(d) 36-microlens rectangular array

Figure 82 – Hartmograms generated by the fabricated arrays for the arbitrary aberration used.

The aberration was then measured with each of the fabricated arrays. Again, the reported values are an average over 10 measurements and the standard deviation is of the order of 0.003λ, which is too low to be represented in the present scale. The final result is shown in Figure 83. In this figure, the black squares represent the measurement with the commercial 127-microlens hexagonal array, which is therefore the reference to which the other measurements must be compared. Note that the array that returned values closer to the reference was the optimized one with 16 microlenses. The rectangular array with 16 microlenses yielded many deviating values, especially for Zernike terms higher than Z_4^4.

The 10-microlens optimized array alternated good and bad results for different Zernike terms. In Table 4, it was shown the condition number associated with different arrays. Among the optimized arrays, the one with 10 microlenses has the smaller condition number, which indicates it is more prone to yield a singular matrix $\boldsymbol{B}^T\boldsymbol{B}$. Besides, as discussed in section 6.1.5, the minimum number of microlenses that can be used with 20 Zernike terms is 10. Therefore, this array is in the limiting case. Hence, the reason for the discrepant values in some of the Zernike terms may be related to numerical errors.

The 36-microlens rectangular array generated some discrepant results, especially for the Z_3^3 and Z_4^{-4} terms. This may have happened because damages were caused to some microlenses of the border of this array. These damages can be noted in Figure 82d, where three light spots of the top left corner cannot be observed. The lack of information about the spots associated to these lenses influences in the final reconstruction error. Additionally, it can be noted in Figure 69 that both the terms Z_3^3 and Z_4^{-4} have increased slopes at the top-left border, what may also have contributed to the poor results of these terms, considering the change in the array geometry caused by the absence of the microlenses. An alternative to try to overcome these damages in the array would be to configure the FrontSurfer© to process only the 33 microlenses for which there are corresponding light spots, instead of processing the whole set of 36 microlenses in which three do not generate the spots, as this has a numerical impact on the reconstruction matrix operations.

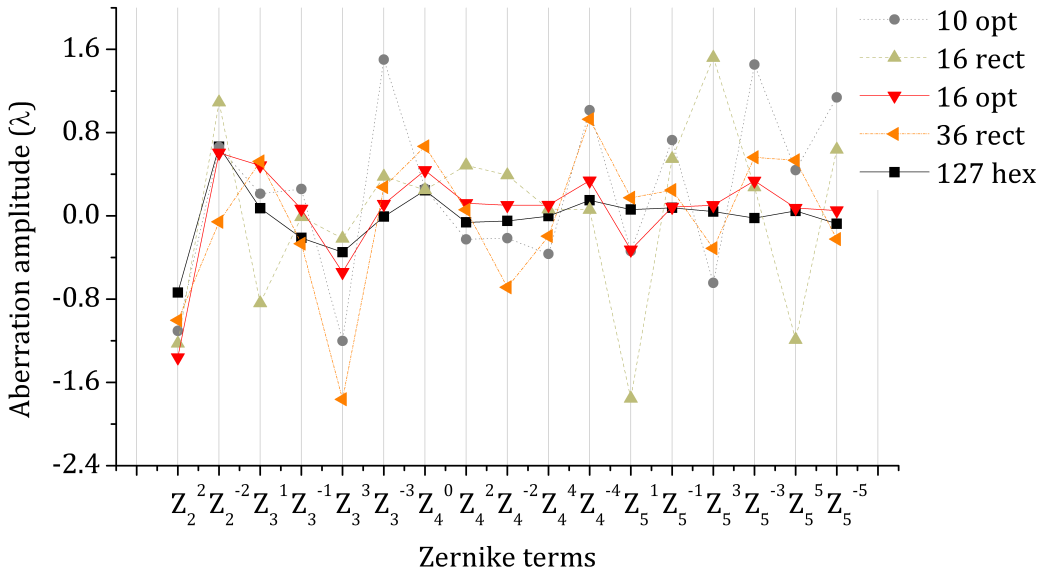

Figure 83 – Comparison among the fabricated and the commercial arrays. In the legend, the numbers represent the number of microlenses in each array and the letters represent the array geometry: 'hex' stands for hexagonal; 'opt', for optimized; and 'rect', for rectangular.

Since the 16-microlens optimized array presented the best results, its coefficients were compared to the ones of the 127-microlens hexagonal array. Figure 84 shows a graph of the correlation between the Zernike coefficients of the two arrays. The calculated Pearson`s coefficient[26] was 0.8554048, which indicates a strong positive correlation between both data sets and, therefore, that both arrays yielded comparable results. As a matter of comparison, two different measurements of the same aberration using the 127-

[26] The Pearson`s coefficient measures the linear correlation between two sets of data. It assumes values always between -1 and +1. The values -1 and +1 indicate perfect negative and positive correlation, respectively. Positive correlation means an increase in the values of one set also causes an increase in the values of the other, whereas the negative correlation means an increase in the values of one set causes a decrease in the values of the other. The value 0 means the two data sets are not correlated. Typically, it is assumed that the data sets are strongly correlated if Pearson`s coefficient is larger than 0.75.

microlens hexagonal arrays are shown in Figure 85. In this case, the Pearson`s coefficient was 0.9996696, which indicates that the variability in the results of several measurements with the same array is very low.

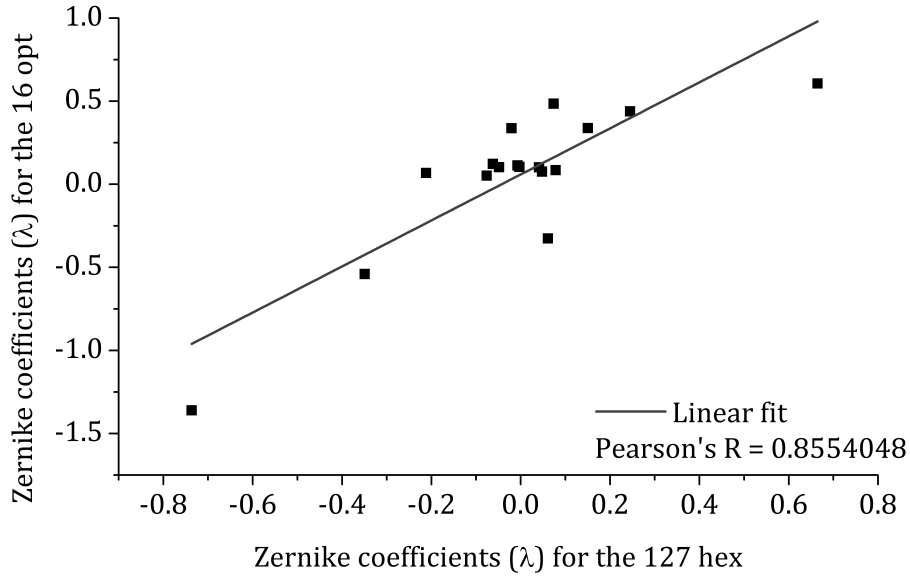

Figure 84 – Comparison of the Zernike coefficients of the 16-microlens optimized array (16 opt) and the 127-microlens hexagonal array (127 hex).

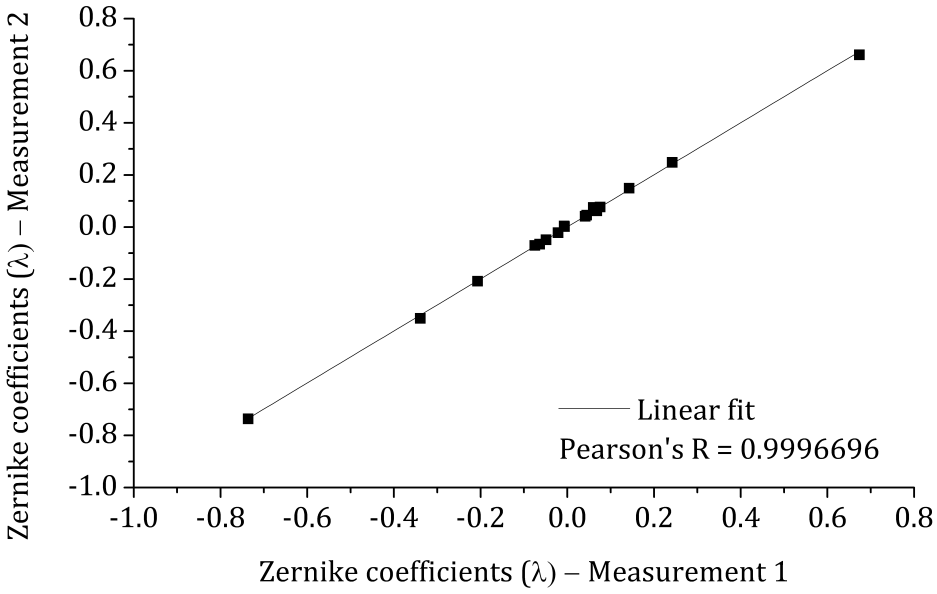

Figure 85 – Comparison of the Zernike coefficients of two different measurements of the 127-microlens hexagonal array.

For all the fabricated arrays, the Zernike coefficients obtained in the measurement of the used aberration were subtracted from the respective values generated by the 127-microlens hexagonal array. The results are shown in Figure 86 together with three bands. Data points that are inside the larger rectangle represent differences in the Zernike terms smaller than or equal to 0.5λ. Those points that are inside the darker rectangle represent differences smaller than or equal to 0.25λ. Similarly, the points that are inside the smaller rectangle represent differences of less than 0.1λ. The 16-optimized array presents the

smaller differences with respect to the reference array. From the 17 analyzed Zernike terms, 16 present differences smaller than or equal to 0.4λ and for 13 terms, the differences were less than 0.25λ.

These differences may be compared with some common industrial standards. For instance, common optical components, such as lenses or mirrors, have aberration amplitudes smaller than 0.25λ. That means that the Zernike terms that describe the wavefront actually produced by the optical component differ of less than 0.25λ from the reference values, which are determined by the component design. Some more precise optical components have deviations smaller than 0.1λ. In what concerns wavefront sensing techniques, interferometric methods have a typical precision of about 0.01λ while H-S wavefront sensors may yield results with precision as high as 0.02λ. Moreover, the standard clinical tolerance in the refraction measurements of the human eye is of 0.25D, what corresponds to a defocus with amplitude of approximately 0.9*λ* for a pupil diameter of 6mm.

Regarding the application to ophthalmology, it is important to mention the work of Rozema *et al.* (2006), in which they have compared the performance of 6 different commercial aberrometers that use different wavefront sensing techniques, including Hartmann-Shack. They have measured the aberrations of 44 healthy eyes and reported the Zernike terms variances among the different equipment, using the same 17 Zernike modes employed in this work. The authors have found differences of up to 0.4*λ* among the measurements performed by the standard commercial aberrometers. Note that this value was also the maximum variance observed for 16 of the 17 Zernike modes measured by the 16-microlens optimized array in the present work.

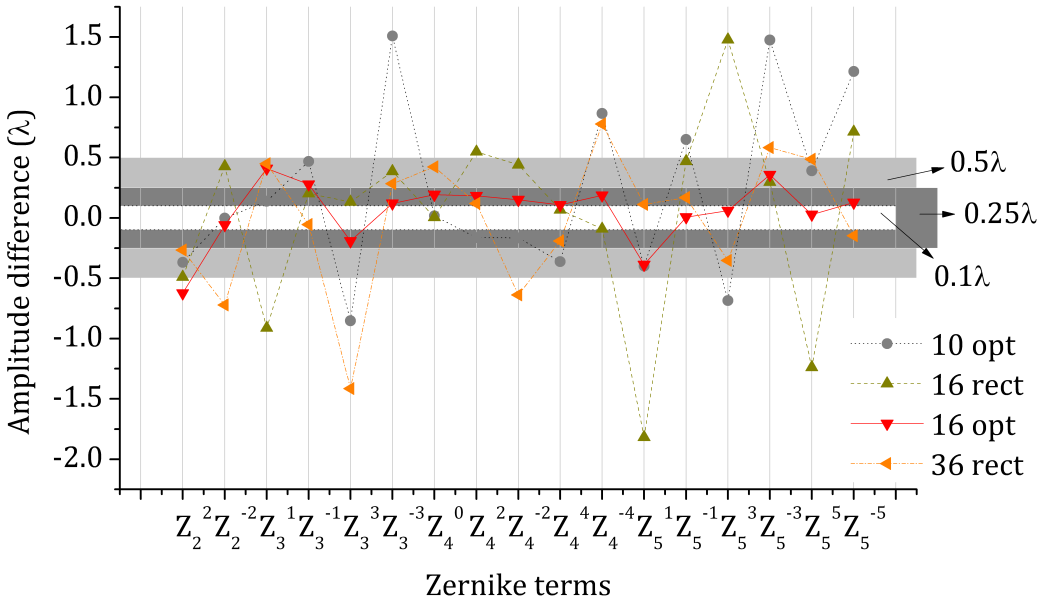

Figure 86 – Deviation of the values of the Zernike terms for each array with respect to the values of the 127-microlens hexagonal array. The hatched rectangles are used as a reference to identify differences smaller than 0.5*λ*, 0.25*λ and* 0.1*λ*.

It is important to reemphasize that the used test aberration was an approximation to the statistics used to design the optimal microlens array. The fact that some of the Zernike terms of the fabricated optical aberration do not match the values and ranges predicted by the statistics may have influenced in the performance of some arrays for measuring some Zernike terms. As already mentioned, an improvement consists in fabricating a known optical aberration with all Zernike terms values fully compliant to the used statistics.

In general, the obtained results corroborate with the ones predicted by the simulations, despite several problems that occurred during the fabrication procedure.

7. FINAL REMARKS

This work proposed the optimization of the microlens array to be used in the measurement of ocular aberrations by means of the Hartmann-Shack technique. The work was divided into three basic parts: numerical optimization, fabrication and test of the microlens array.

This proposal was motivated by the already known influence of the array geometry on the sampling process of a wavefront. It was already shown in the literature that, in general, arrays with random distribution of microlenses could yield smaller reconstructions errors than rectangular arrays.

Moreover, the optimization of the microlens array for a given aberration statistics, such as that for ophthalmology, may produce benefits such as reduction in the wavefront reconstruction error and processing time; the last favors real-time wavefront-measurement systems.

The first part of the work consisted in performing the optimization process, which was carried out for the 10-, 16- and 36-microlens arrays. The results showed that these arrays generate reconstruction errors as small as those for the 25- and 36-microlens rectangular array. That means that an optimized array can afford fewer microlenses while maintaining a low reconstruction error. Moreover, it was shown that the 16-microlens rectangular array is inappropriate to sample the 17 Zernike modes used (piston, tip, tilt and defocus were not considered), since it generates too high reconstruction errors. Nevertheless, the 16-microlens optimized array was shown to perform similarly to the other tested arrays. Arrays with fewer microlenses are more flexible to be designed, since the extra space can be used with other purposes, such as to increase microlens diameter or to include additional integrated circuit functionality on the focal plane, e.g. in a corresponding PSD array. It was also demonstrated that the optimized arrays were not significantly affected by rotation of the array with respect to the wavefront aberration.

The second part of the work consisted in fabricating the microlens arrays. They were fabricated through replication on a mold built using photolithography and a KOH etching technique. The molds were produced in silicon and the arrays were replicated in a UV-curing photopolymer. Despite some problems, the process was successful in producing the desired microlens arrays. It is pertinent to emphasize that these were the first microlens arrays fabricated at UFMG with the KOH etching technique.

The last part of the work consisted in testing the fabricated arrays and comparing their results with those generated by a commercial 127-microlens hexagonal array. The arrays were used to measure an optical aberration. As expected by the simulations, the 16-microlens rectangular array generated the worst results, in comparison with the reference. The 10-microlens optimized array alternated some bad and good results for different Zernike terms, probably because of numerical errors. The array is in the numerical limiting case, since this is the minimum number of microlens necessary to reconstruct 20 Zernike modes. The 36-microlens array had its performance influenced, at least in some of the Zernike modes, by the lack of information from three corner microlenses, which presented fabrication damages and therefore could not generate light spots on the focal plane.

The 16-microlens optimized array presented results closer to the reference ones. The values for the Zernike coefficients generated by both the 16-microlens optimized and the 127-microlens hexagonal arrays were compared using the Pearson's coefficient. It was shown that both arrays produced strongly correlated results (Pearson's R = 0.8554048). Moreover, from the 17 analyzed Zernike terms, 16 presented differences smaller than or equal to 0.4λ, which is compatible with the standard clinical tolerance for defocus measurement. Besides, that value is also comparable with the maximum deviation observed in the comparison of results generated by different commercial aberrometers.

In general, the final results corroborate with those from the numerical simulations, and are very encouraging as regards application of optimized microlens arrays in systems where the wavefront statistics are known.

8. PROSPECTIVE WORK

Several ideas for additional work arose during the execution of the present work. At least some of them will be implemented in the near future. The main ideas consist in:

a) Fabricating an optical aberration fully compatible with the used wavefront aberration statistics. This is important to improve the test results, since the aberration used in this work contained some modes outside the used statistics range.
b) Obtaining a more comprehensive set of eye-aberration data, which could allow the use of the analytical expression proposed by Diaz-Santana, Walker and X-Bará (2005) to calculate the wavefront reconstruction error.
c) Including the number of microlenses as a variable also to be optimized. This would make it possible to find also the optimal number of microlenses in the array.
d) Optimizing the microlens-array geometry for aberrations with high-order terms out of the population statistics. The effects of high-order terms over the vision quality are not yet clearly understood. Since the values of these terms in the statistics are approximately zero, it would be of practical interest to precisely measure those cases in which these values are out of the statistical range.
e) Optimizing the microlens-array geometry for low- (defocus and astigmatism) and mid-order terms (spherical and coma) only, since these are currently the terms for which the influences on vision quality are better understood and perceptible. By including the number of microlenses as a variable of the optimization problem, it is likely that the optimized array will contain even fewer microlenses, if less Zernike modes are considered.
f) Changing the microlens diameter and perimeter geometry, to assess their influence over the reconstruction error and to try to find optimized arrays with larger fill-factor. After optimization, the lenses in the array can be designed with different shapes so that they touch each other and a 100% fill-factor array is built. This contributes to an increase in the signal-to-noise ratio at the detector, since more light energy is collected per lens.
g) Designing a setup to alternate regular and optimized geometries to favor both high- and low-frequency modes. This can be interesting because apparently regular arrays perform good to sample low-frequency Zernike modes, such as defocus and astigmatism. An automated measurement using both regular and optimized arrays could be used to favor simultaneously low- and high-frequency modes.
h) Including a constraint in the optimization process to guarantee that the reconstruction errors for low-order Zernike modes are as low as possible. This is an important improvement to guarantee that benefits of the optimized array do not negatively affect the precision in the measurement of the modes that are currently well known and most significant in clinical practice.
i) Elaborating a control procedure to identify all possible error sources during the fabrication process.
j) Testing different substances to be applied on top of the mold in order to facilitate the detachment of the cover glass and optical adhesive from the mold. This was a laborious step of the fabrication process and some tests were performed until a

satisfactory result was empirically achieved with PMMA. However, a systematic study about the characteristics of the coating to facilitate detachment would certainly contribute to improve results (e.g. PDMS).

k) Designing microlenses with different focal distances, so that the corresponding spot sizes are also different. Then the spots can be easily recognized by its size and associated to the corresponding microlens on the array. This guarantees a larger focal-plane dynamic range in comparison with the currently available microlens arrays, in which a light spot produced by a high-amplitude local wavefront tilt may lie in the region corresponding to a microlens other than the one that generated it. This represents a source of errors in the measurement.

l) Designing a portable pupilometer, which could be used to measure the pupil-diameter variation of the patient during his daily routine. The information regarding pupil behavior is important for a doctor to precisely plan the clinical procedures most appropriate to the patient.

m) Using the intensity profile of the spots in the aberrometry to assess and monitor cataract in very early stages, when the vision quality is not yet sufficiently affected. Cataract refers to an opacification process of the crystalline lens. The process is gradual and such measurements would allow the identification of changes in the transmittance of the crystalline lens much before the patient complains about a decrease in his vision quality.

n) Investigating the influence of high-power laser exposure on SiO_2 etching, which could allow the production of rounded cavities to mold the microlenses directly on the SiO_2.

ACKNOWLEDGEMENTS

First of all, I thank the Lord for being so merciful to me. The completion of this thesis represents a significant achievement in my life and it would not be possible without His support and love.

Many people have contributed directly and indirectly to the realization of this work. Some helped me with the technical aspects, others with discussions and ideas, some with personal support and some others contributed just because they have crossed my way. It is certainly not possible to name all of them, but each of them has a special place in my heart.

I thank my wife Luciane for being so strong by my side. She has been with me since the very beginning of the Ph.D. program, in 2008, and things definitely were not easy. Many challenges and choices were present all the time and her support and perseverance were indispensible. Her care and love gave me the strength to persist towards our objectives. I also apologize for the many moments when the work did not allow me to be as present as I should.

I also thank my baby Artur, for providing us with so many delightful moments. He was a gift from the Lord and has made me much stronger.

I thank my parents and brother, Graça, Toninho and Fael. They were always by my side, independently of the adversities. Knowing that I can always count on them whenever I need is priceless. The real family they have always been to me, gave me support and confidence to always believe I can achieve something significant in my life.

Many friends and relatives were very important for sharing with me both enjoyable and troublesome moments. Special thanks to the great friends Gustavo Camilo and the guys from the IBBP church Paulo, João, and Marcelo.

I also thank my colleagues from the OptMA^{lab}. They have helped me a lot with technical aspects of this work. Special thanks to Rodolfo, for helping me with the fabrication processes; to Luciana, for the help during the numerical modeling step; to Felipe Tayer Amaral, for helping me with the tests; to Luiz, Felipe Viana, Marcos Carvalho, Thiago Coura and Jens, who helped a lot with our attempts with the optical bench. I thank all the OptMA current and past members, who have provided technical support and a very productive environment.

I thank the agencies that financially supported me and my work in the lab: CNPq and Fapemig.

And at last, but definitely not the least, I thank and express my admiration for my supervisor Davies. With him, I learned much more than technical knowledge. His expertise, patience, perfectionism, excitement and care taught me I should always believe I could reach higher levels and be a better person. I am certainly a better person now, after the Ph.D.

Davies, you made the difference in my life! Thank you very much for that.

ABOUT THE AUTHOR

Otávio Gomes de Oliveira was born in Manhuaçu – Minas Gerais/Brazil, on August 2nd, 1983. At Universidade Federal de Juiz de Fora (UFJF/Brazil) he received the degrees of BSc in Physics (2005) and MSc in Ecology (2007). During the Master`s program, he has worked with the development of a computer-controlled optical equipment to study the vertical movement of cyanobacteria. In 2008, he joined the OptMA^{lab}/UFMG as a Ph.D. student of the Post-Graduation Program in Electrical Engineering, where he worked with applied optics. His whole academic career was characterized by multidisciplinary research in problems of practical interest. His professional experience so far include undergraduate teaching, research, R&D management and entrepreneurship.

APPENDIX

In this section, it is presented an additional work that aimed at developing an embedded DSP-based system to control an adaptive optics system. This work was temporarily discontinued in order to allocate more efforts on the optical aspects presented in this thesis, however the results achieved are worth reporting.

EMBEDDED SYSTEM FOR ADAPTIVE OPTICS SYSTEM CONTROL

Greenaway and Burnett (2004) emphasize that the first generation of adaptive optics systems has yielded impressive results, but are not still in routine use in the world. Therefore, there is a growing interest in low-cost, robust, compact and "plug-and-play" systems and components.

In this sense, this work aims at developing a dedicated embedded system for controlling the adaptive optics system. To accomplish to this task, the system must be able to perform the following tasks:

a. receive as input either the image generated by an off-the-shelf camera or the signals generated by an array of position-sensitive detectors. In this work, a CCD camera is used.
b. analyze the input so as to extract the deviations of each light spot, which were generated by the Hartmann-Shack method.
c. reconstruct the wavefront aberration.
d. actuate the wavefront modulator: a deformable mirror, in the present case.

Hitherto this system has not been completed yet. Then, this section will describe the used technology and the parts that have already been concluded.

DIGITAL SIGNAL PROCESSOR (DSP)

The control task in an adaptive optics system is generally accomplished by a computer. The substitution by an embedded control system is motivated by the possibility of building more compact and portable AO systems. Although cost reduction is also likely to occur with the substitution, it is not sufficiently significant (in comparison with the cost of the entire AO system) to motivate the whole task by itself. Portable and compact AO systems may contribute to increasing its range of applications to include the possibility of using it in airplanes and submarines, for instance. Moreover, such systems could be designed to offer mobility, in the sense that the same system could be transported to perform diagnostics in different places of, for example, a production line in industry.

The first step in designing the control system for AO consists in selecting the appropriate development hardware, which depends on the application requirements. When a camera is used to capture the image of the light spots generated in the Hartmann-Shack method, the input to the control system is an image. That means that the development hardware must be capable of decoding video. Moreover, the hardware must feature large enough memory space to allow embedded processing of image data and reconstruction of the

wavefront aberration. These requirements guided the choice of the development hardware.

A DSP-based (Digital Signal Processor) hardware was chosen to be used in the control system. A development kit from Analog Devices, Inc. was chosen, the ADSP-BF533 EZ-KIT Lite®, which already contains decoder and encoder chips for video processing onboard (ANALOG DEVICES, INC., 2007). The kit uses the DSP BF533 of the *BlackFin*® series of Analog Devices, Inc.

Besides the system requirements mentioned above, the choice was also guided by convenience in aspects such as availability of personal contacts with experience in programming processors from this family, availability of a development kit featuring enough memory size and video interface, familiar development environment and familiar programming language.

The use of a development kit, rather than the processor and specific electronics for running the control system, is purely due to convenience. As the name suggests, it is easier to use it during the development step, once there is no need to worry about electronic-circuit design. Moreover, the low cost of a development kit (compared to the entire AO system cost), together with characteristics such as portability, compactness and reliability, suggest that the development of a specific electronics for the AO control system can be postponed to future work, as the market is still a niche one and the focus of this development is currently on academic research. Designing such electronic circuits, including video decoder, access to external memories and interfaces for communication with the development environment would demand additional effort, which could be as for now more usefully in the firmware[27] development.

The development kit is designed to be used in conjunction with the Visual DSP++® development environment, which is a management system that provides a suite of tools for developing processor applications and projects with a C/C++ compiler. Besides the project manager facility, it also includes debugging features, such as plotting values from memory and using breakpoints to view registers and memory (ANALOG DEVICES, INC., 2007).

The ADSP-BF533 EZ-KIT Lite® features (ANALOG DEVICES, INC., 2007): ADSP-BF533 *BlackFin*® processor; 64MB of synchronous dynamic random access memory (SDRAM); 2MB of flash memories; analog audio interface with 96KHz audio codec, with 4 input and 6 output RCA jacks; analog video interface through video decoder and encoder chips with 3 input and 3 output RCA jacks; universal asynchronous receive/transmitter (UART); LEDS and push buttons. Some characteristics of the BF533 processor are (ANALOG DEVICES, INC., 2008): performance of 600MHz, 148KB of RAM memory, external memory controller, parallel peripheral interface (PPI), DMA (direct memory access), SPI-compatible port, real-time clock and universal asynchronous receiver/transmitter (UART).

[27] A firmware is an algorithm that is programmed and runs directly on the hardware.

IMAGE ANALYSIS ALGORITHM

The first two tasks the embedded system has to perform are receiving an image as an input and processing the image in order to determine the light-spot deviations. Figure 87 shows an example of a Hartmann-Shack image that must be processed by the image analysis algorithm.

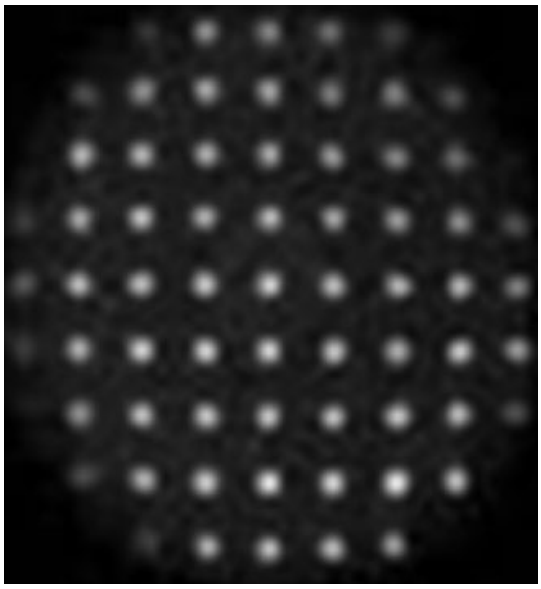

Figure 87 – An example of an output image of the Hartmann-Shack method.

In the figure, the brighter regions correspond to the light spots and the main objective of the image analysis algorithm is to determine the coordinates of each light-spot centroid or, in other words, the coordinates of the center of each bright region. Difficulties may arise when the images do not have good quality, in terms of contrast between the brighter regions and the background. In the presented image, for instance, the light spots are immersed in a noisy gray background[28]. This imposes limitations to the image analysis algorithm. One of them refers to the light spots which have peak intensity of the same order as the background, what makes it difficult to be distinguished from the noisy background. Another limitation refers to the precision with which the light-spots centroid coordinates are calculated, due to the noisy background.

The first step is to configure the video decoder and the DMA, so that when a frame is available at the input of the kit, it is decoded and sent to the PPI. The DMA takes the data automatically and sends it to the SDRAM. When DMA finishes the transfer, it generates an interrupt on the main code, indicating that the image is ready to be processed, i.e. that the image has just been acquired. During the image processing, the interrupts are disabled.

The image processing algorithm comprises pre-processing, identification of light spots, calculation of the centroid coordinate of each light spot and conversion of the position values from pixel[29] units to micrometers (the chosen unit for the wavefront reconstruction

[28] The referred noise may be present either because of the camera itself or because of optical effects such as speckle, diffraction and spurious reflection or refraction.
[29] Pixel is the smallest element of a digital image. Its value is associated with the light intensity on it.

algorithm). Figure 88 shows a block-diagram emphasizing the sequence of tasks performed by the algorithm. Each step will be treated in detail.

It is first important to note that the acquired images are in 8bit-grayscale format. That means that the pixels have values that range from 0 to 255, which represent black and white points, respectively.

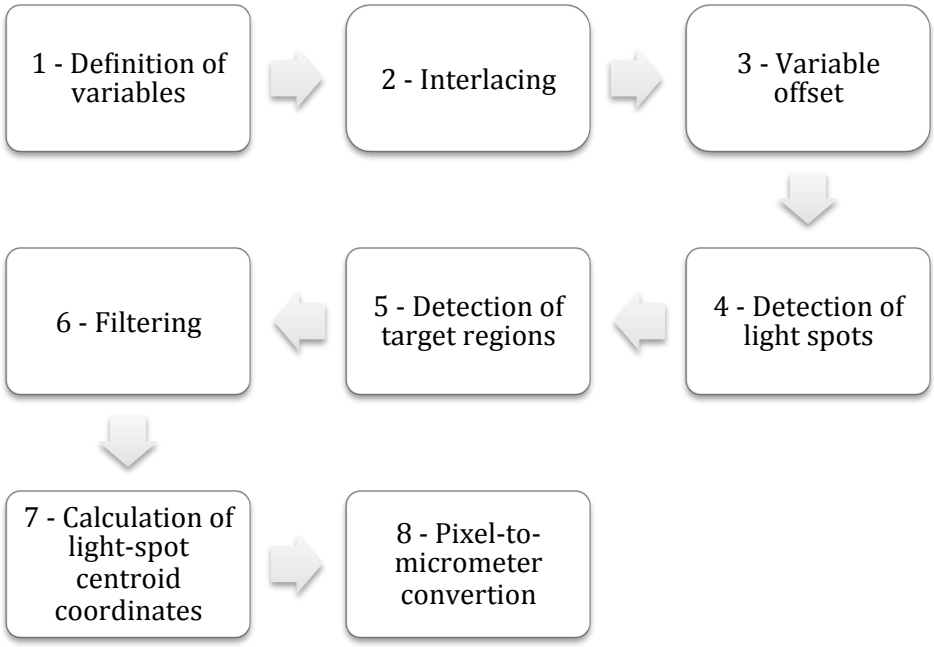

Figure 88 – Block-diagram of the image-processing algorithm.

All the variables and arrays used in the algorithm are declared in step 1. All the arrays used to store images during the processing point directly to the SDRAM, since they demand a large memory space. These arrays store the acquired image; temporary images, which are created during the processing; and information regarding the detected light spots. The acquired image, for instance, is stored in the SDRAM from the first address. The array which points to the acquired image is then mapped to SDRAM also from the first address. Each element of the array contains the value of one pixel. The size of the image in terms of number of pixels in each of the two dimensions is defined previously in the decoder configuration. The reference between the elements position in the array and the pixel coordinates is done as follows:

$$a = y * width + x \qquad 30$$

where a corresponds to the element count, (x, y) corresponds to the (column, line) pixel values in the image and $width$ is the number of columns of the image.

The video decoder is factory pre-configured to process the even and odd lines of the image independently. The image is then transferred by DMA to the SDRAM as two independent sub-images. One contains the even lines and the other contains the odd lines. Hence, each sub-image contains only half the image acquired by the camera. In step 2, these two sub-images are interlaced. That means they are put together to form the acquired image, which contains all the lines and therefore represents exactly the image projected in pupil of the

camera. The acquired image replaces the sub-images stored in the memory, once they will not be used anymore.

In step 3, the image is submitted to a pre-processing, where the light spots are intensified in relation to the background. This is necessary for reducing the amount of false light spots found in step 5, due to background noise. The intensification of the light spots is done through the summation of a variable offset value to each pixel. The offset is defined as a function of the pixel value, as follows:

$$Offset = 2^{(\frac{pixel\ value}{50})} \qquad 31$$

An exponential offset guarantees that pixels with larger values will have larger offset. Therefore, the difference between the values of pixels from the light spots and from the background will be increased. The choice of the constant values in equation 31 was made based on two restrictions. The first one is that the offset function should provide a reasonable increase in the difference between the background and the light spots values. The second is that it should not provide too big values because the image is in 8-bit format and therefore a pixel value cannot be higher than 255. The resultant image does not replace the original one in the SDRAM. Figure 89 shows the offset values magnitudes as a function of the pixel value.

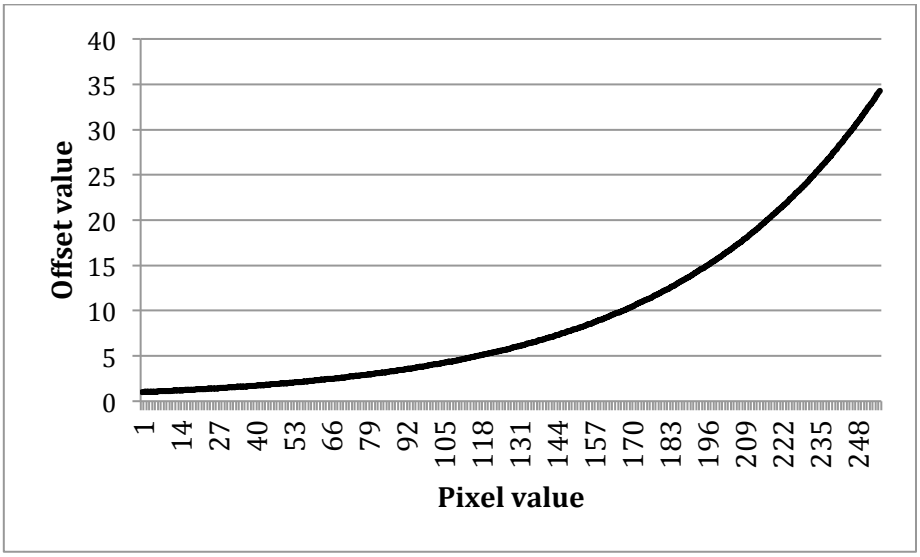

Figure 89 – Graph of the offset function.

With the offset added, the new image can be more easily processed in step 4. The processing consists in sequentially screening, point-to-point, the whole image with a 20x20 pixel mask. The center of the mask coincides with the current pixel. For each pixel in the image, the variance v is calculated within the mask. The variance is given as a function of the value $m[x_i, y_i]$ of the pixel in the position (x_i, y_i) and the average $mean$ of all the pixel values inside the mask.

$$v = \frac{1}{20^2 - 1}\{m[x_i, y_i] - mean\}^2 \qquad 32$$

The size of the mask was chosen to be 20x20 pixels, based on many tests to assess how the size of the mask influences the light-spot centroids determination. This size is of the same order as the light-spot diameter.

The algorithm compares the variance value of the current pixel with a pre-established threshold. If greater, the pixel value is set to 255 (white, in the image). On the other hand, if the variance is smaller than the threshold, the pixel value is set to 0 (black). These new values of each pixel are stored in another variable, i.e., another image, which is binary in the sense that it contains only two colors. This procedure is called image thresholding (RUSS, 2007).

Therefore, in this new image, the binary image, the white points correspond to those for which the variance inside the 20x20 pixels mask is greater than the threshold. Each white region is likely to correspond to a light spot. Figure 90b shows an example of a binary image generated by step 4. Figure 90a is the acquired image. One can note that to each white region in (b), it is associated a light spot in (a). However, there are some light spots in (a) without correspondence in (b), as the one marked in yellow, for instance. This is because the light-spot peak intensity is of the same order as the background noise. Therefore, the algorithm was not capable of distinguishing it from the background.

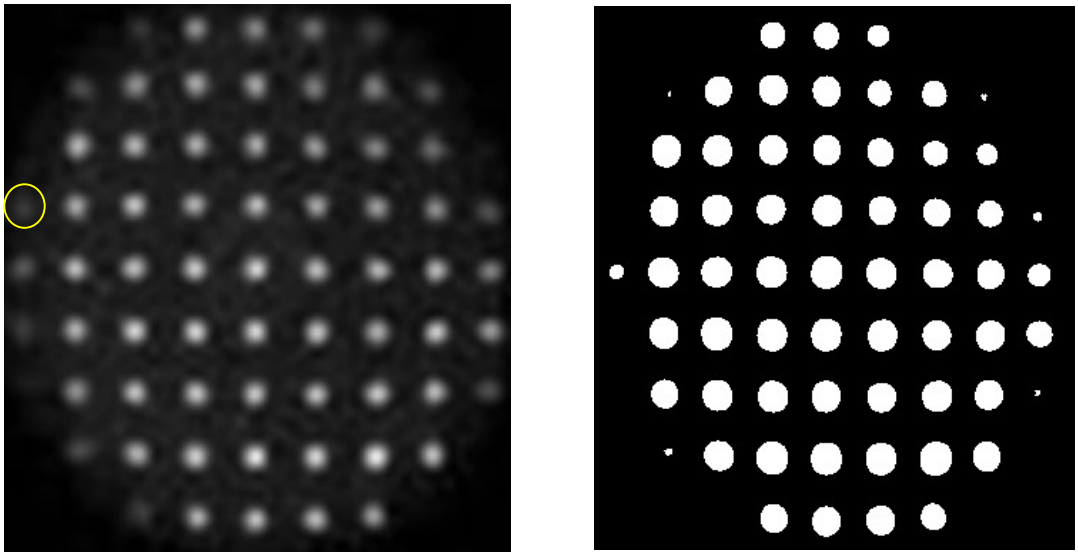

(a) (b)

Figure 90 – Binary image generated by step 4.

Step 4 is nothing but a method for searching for contours – regions of high variance values in an image. In the present case, the algorithm searches for the light-spot boundaries. If the mask used has a small lateral size (in comparison with the light-spot diameter), the points for which the variance is greater than the threshold are only the ones close to the light-spot boundary. In this case, the expected final image contains a curve around the light-spot, representing its border (as illustrated in the picture on the left of Figure 91). On the other hand, if the mask has a lateral size similar to the light-spot diameter, a variance greater than the threshold is associated to any point of the light-spot. Therefore, the expected binary image is so that the whole area that corresponds to the light-spot is set to white, i.e. the pixel values are equal to 255 (as illustrated in the picture on the right of Figure 91).

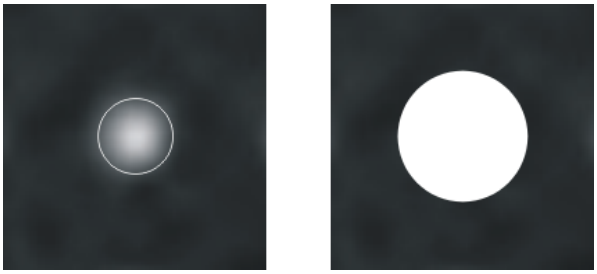

Figure 91 – Detection of light spots. The lateral size of the mask used in the picture on the right is 20 times bigger than the one on the left.

Once the binary image is completely generated, it is necessary to identify the white regions. A blob-coloring algorithm (step 5) (BALLARD and BROWN, 1982) is responsible for detecting the regions and the coordinates of each of its N points. Simultaneously, the centroid coordinates (x, y) of each region is also calculated through the average of each pixel coordinates (x_i, y_i):

$$x = \frac{1}{N}\sum_{i=1}^{N} x_i \qquad y = \frac{1}{N}\sum_{i=1}^{N} y_i \qquad 33$$

The centroid coordinates of each region are then passed to a filtering step. Two regions that are too close to each other are likely to represent two parts of the same light spot or be a noise around a spot (See Figure 92 for an example of a white region that occurred due to noise). The outputs of step 6 are two arrays, each containing one of the centroid coordinates (x, y) of the white regions that represent light spots. However, the centroid coordinates of the regions do not necessarily represent the centroid position of the light spot.

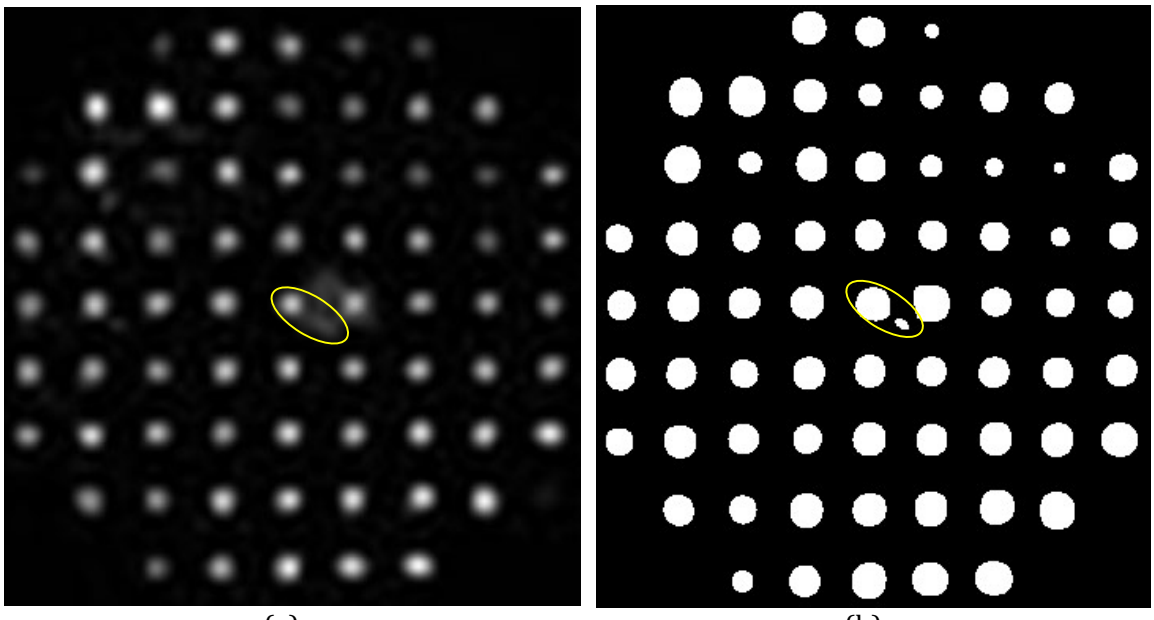

(a) (b)

Figure 92 – Example of white regions that do not represent light spots. The acquired image is shown in (a) and the binary image, in (b).

In step 7, the position of maximum intensity of each light spot is calculated. In the acquired image (output of step 2), a $N \times N$-pixel mask is centered in each of the coordinates (x, y) calculated in step 6. The size of the used mask was empirically chosen to be $N = 32$ pixels based on tests to assess how the size of this mask influence in the precision on the centroid coordinates determination. The sum M of the values $m[x_i, y_i]$ of all the pixels inside the mask is calculated and then the coordinates (x_c, y_c) of the intensity center of each light spot are given by:

$$\begin{aligned} x_c &= \frac{1}{M} \sum_{i=1}^{N} x_i \cdot m[x_i, y_i] \\ y_c &= \frac{1}{M} \sum_{i=1}^{N} y_i \cdot m[x_i, y_i] \end{aligned} \qquad 34$$

Two arrays, each of them containing the x_c and y_c coordinates of the light spots, respectively, correspond to the output of step 7 and almost to the final result of the image analysis algorithm. One last step must be carried out to convert the values (x_c, y_c), given in pixels, into values (x_s, y_s), given in micrometers. Step 8 consists then in solving the following pair of equations:

$$\begin{cases} x_s = x_c \cdot p_x \\ y_s = y_c \cdot p_y \end{cases} \qquad 35$$

where (p_x, p_y) are the size in micrometers of each pixel in the image. When these values are not informed by the camera manufacturer, the determination of the pixel dimensions has to be carried out in practice. A pinhole is used as a point-like light source and is placed at two different positions before the wavefront sensor. In both cases, the centroid positions are calculated and the deviations between the two images are analyzed. The comparison to theoretical calculation results in the pixel dimensions.

The two arrays containing the coordinates x_s and y_s, respectively, are then the output of the image analysis algorithm. These are the values which will be used in the wavefront reconstruction algorithm.

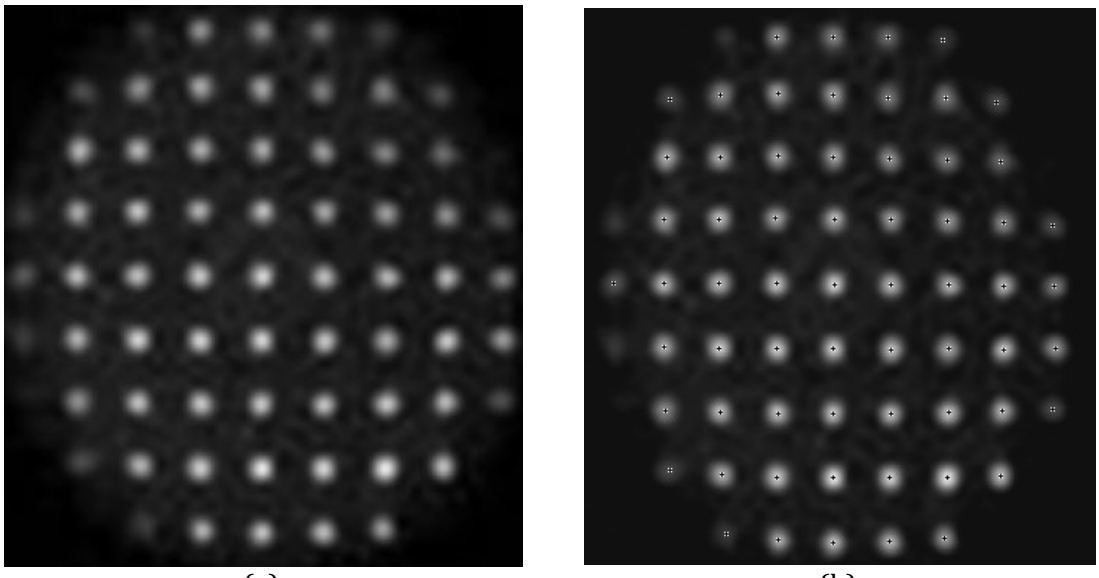

(a) (b)

Figure 93 –(a) Acquired image. (b) Image with light-spots centroids detected (marked with a small black cross in the middle of a white box).

WAVEFRONT RECONSTRUCTION ALGORITHM

The wavefront reconstruction algorithm implemented in the embedded system is the same as the one used in the Hartmann-Shack numerical model.

Reconstruction the wavefront aberration consists in solving equation 13, repeated here for convenience:

$$\boldsymbol{B}^T\boldsymbol{S} = [\boldsymbol{B}^T\boldsymbol{B}]\boldsymbol{C}$$

where $\boldsymbol{B}$ is the Zernike terms derivative matrix and $\boldsymbol{B}^T$ is its transpose, $\boldsymbol{S}$ is the vector of light-spot deviations and $\boldsymbol{C}$ is the vector Zernike coefficients, which has to be found.

The first step in the algorithm consists in calculating $\boldsymbol{B}^T$. A numerical function is responsible for calculating the Zernike terms and the derivatives are calculated also numerically, rather than analytically.

Then, the matrices $[\boldsymbol{B}^T\boldsymbol{B}]$ and $[\boldsymbol{B}^T\boldsymbol{S}]$ are calculated. The system of linear equations from equation 13 can then be solved by Gaussian elimination with partial pivoting and back-substitution (PRESS, TEUKOLSKY, *et al.*, 1992). It consists basically in making operations in the equations so that the matrix $[\boldsymbol{B}^T\boldsymbol{B}]$ is reduced to an upper-triangular form. Then the back-substitution step is responsible for solving the system for all the unknown Zernike coefficients.

The image analysis algorithm and the reconstruction algorithm are implemented, but are not working together yet.

ADAPTIVE OPTICS SYSTEM DESIGN

In this work, the adaptive optics system was thought to accomplish two tasks: identify wavefront aberrations in optical components and correct for wavefront aberrations. The idea is to use the same system both to characterize the aberrations present in optical components, such as lenses, transparent materials or even the human eye, and to correct for these aberrations. Therefore, the system must feature a laser, to provide light to impinge on the optical components and then to be analyzed by the wavefront sensor. Moreover, the system must contain structures where the components to be analyzed will be placed, taking into account that it will be used with either transmissive or reflective components.

The optical components introduce aberrations in the impinging light beam. These aberrations must be measured by the wavefront sensor and corrected by the deformable mirror. A challenge is to guarantee that the wavefront aberration does not change in the paths between the component and the wavefront sensor and between the deformable mirror and the components. In other words, it is equivalent to say that these optical structures must be phase-conjugated, or must be in phase-conjugated planes. That ensures that the optical system produces a spatially-invariant effect on the point-spread function of the imaging system (GREENAWAY and BURNETT, 2004).

The phase conjugation between two planes A and B can be achieved by the use of a relay system, i.e. two in-line lenses with focal distances $f_1$and f_2 and positioned $f_1 + f_2$ apart. Planes A and B must be located at distances L_1 and L_2 from their respective lenses, as shown in Figure 94. This optical configuration is known as relay system.

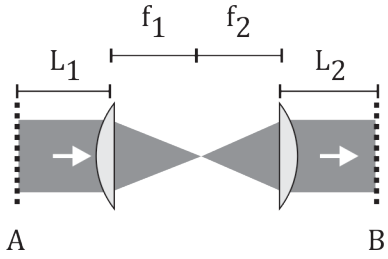

Figure 94 – Lenses configuration for optical phase conjugation.

Once the lenses are chosen, as well as L_1, the distance L_2 can be calculated using equation 36.

$$L_2 = \frac{f_2(f_1^2 + f_1 f_2 - L_1 f_2)}{f_1^2} \qquad 36$$

If the lenses have different focal distances, the beam diameter is altered according to the ratio of the focal distances. The beam diameter in plane B is to the beam diameter in plane A as f_2 is to f_1.

An adaptive optics system has been designed and assembled. The optical setup is ready and the system can already detect wavefront aberrations. To complete the whole closed-loop AO system, the mirror control must still be incorporated.

Some requirements established the optical design of the system. One of them is to have an AO system that can be used to measure aberrations introduced in the light beam either through reflection or refraction. Another desired characteristic of the system is to be able to assess qualitatively the operation of the deformable mirror, by means of far-field imaging of the mirror's surface.

The deformable mirror is placed at a phase-conjugated plane to both the planes where wavefront aberrations should be introduced and to the entrance pupil of the Hartmann-Shack sensor; the two latter planes being also phase conjugated.

The optical system design is shown in Figure 95.

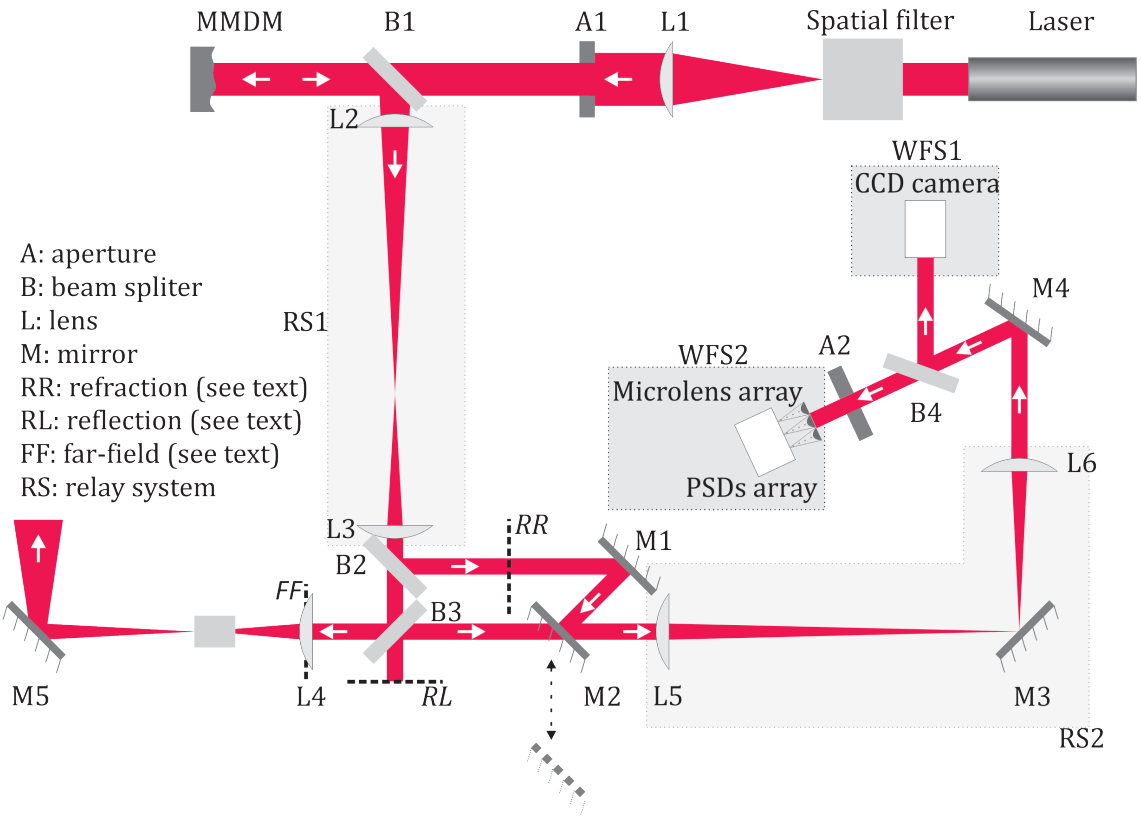

Figure 95 – AO system design.

The light beam is emitted by the laser and passes through a spatial filter, emerging divergently from it. After passing through the lens L1, the beam becomes parallel, i.e. collimated. In aperture A1, the beam diameter is set to 12mm, to match the reliable reflective area of the deformable mirror. The deformable mirror diameter is 15mm. It is advisable to avoid the boundaries of the deformable surface, since the electrodes are concentrated in the center and the border is anchored on a frame that limits its deflection and might affect its correction capabilities. Therefore, the beam diameter impinging on the mirror is 12mm.

Then the beam passes through the beam splitter B1 and reaches the deformable mirror perpendicularly. In its way backwards, the beam is reflected by the beam splitter B1 and enters in the relay system RS1. This relay system is used to phase-conjugate the deformable mirror and three planes: the ones to introduce aberration (aberration planes) through reflection (RL) and refraction (RR) and the plane (FF) to generate the far-field image. The same relay system is also used to reduce the beam diameter to 6 mm, to match the entrance pupil of many optical components for which the wavefront aberration is to be measured, including the eyes, and also the entrance pupil of the Hartmann-Shack wavefront sensors deployed here.

In beam splitter B2, part of the beam is reflected to impinge on the optical component through refraction. The other part of the beam reaches beam splitter B3 and is divided to impinge on the lens L4 and the plane RL. The light that reaches the lens L4 is focused on a micro-objective to generate the far-field image, which is projected on the wall by mirror M5.

The mirror M2 is used to choose between the aberration planes to be analyzed: reflection or refraction. It can be moved in order to prevent that one of the beams coming from either RL or RR reaches the relay system RS2. This relay system is used to phase-conjugate the aberration planes to the entrance pupil of the wavefront sensor.

Two Hartmann-Shack wavefront sensors are being used. One (WFS1) uses a CCD camera to detect the image of light-spots. The other (WFS2) uses a 2D array of position-sensitive detectors. The purpose of using two wavefront sensors is to compare the results from both methods. When the light beam reaches beam splitter B4, it is divided to reach both wavefront sensors. The lenslet array used in WFS1 is coupled to the camera, whereas the one in WFS2 is placed before the PSDs array, as indicated in the figure. The WFS2 is not yet coupled to the system.

The assembled system is shown in Figure 96.

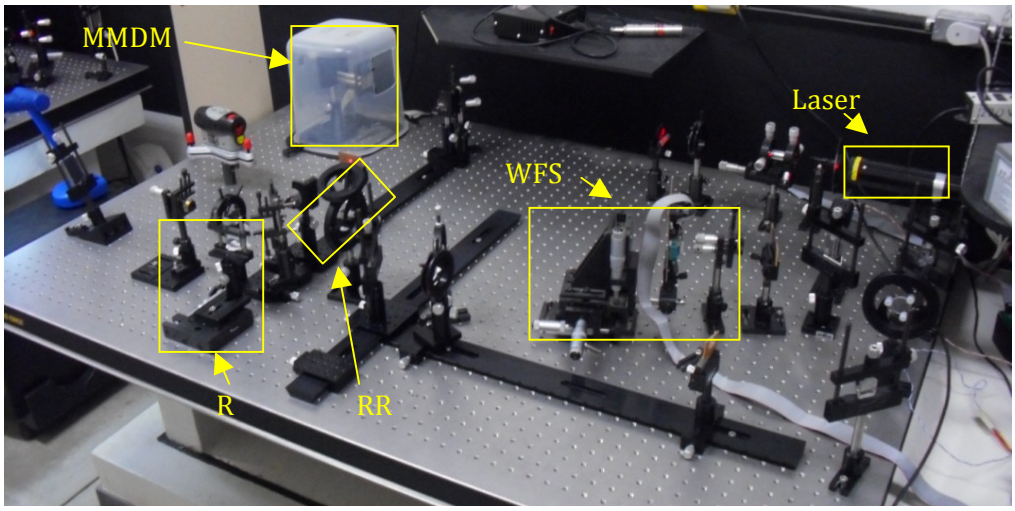

Figure 96 – AO system assembled.

As already emphasized, the optical system is already assembled and partially working. It is possible to measure the wavefront aberration introduced by an external optical component, for instance, but only qualitatively, since it is not calibrated yet. A demonstration experiment was carried out in which the wavefront aberration introduced by a beam splitter (transmitted portion) was measured. First, in Figure 97 it is shown the far-field and the interferogram images generated before placing the beam splitter in the system.

(a) (b)

Figure 97 – (a) Far-field and (b) interferogram images without the beam splitter.

Figure 98 shows the same images for when the beam splitter is placed at the aberration plane. The deformations observed in both images are generated by the aberration introduced in the light beam when it passes through the beam splitter.

(a) (b)

Figure 98 – (a) Far-field and (b) interferogram images generated with the beam splitter.

The images shown in Figure 97 and Figure 98 were generated with the software FrontSurfer® (OKO TECHNOLOGIES, 2006).

BIBLIOGRAPHY

AMARAL, F. T. **Circuito Óptico e Metodologia para Caracterização de Lentes Intraoculares**. Belo Horizonte: Universidade Federal de Minas Gerais - Programa de Pós Graduação em Engenharia Elétrica, 2011. 121 p. Available at: http://www.cpdee.ufmg.br/defesas/69M.PDF.

ANALOG DEVICES, INC. **ADSP-BF533 EZ-KIT Lite: Evaluation system manual**. Norwood, p. 89. 2007. (3.1).

ANALOG DEVICES, INC. **Visual DSP++ 5.0 user's guide**. Norwood, p. 442. 2007. (3.0).

ANALOG DEVICES, INC. **BlackFin embedded processor: ADSP-BF531/ADSP-BF532/ADSP-BF533**. Norwood, p. 64. 2008.

ARNOLD, C. B.; MCLEOD, E. A new approach to adaptive optics for materials processing. **Photonics Spectra**, p. 78-84, November 2007.

ARNON, S.; KOPEIKA, N. S. Adaptive optical transmitter and receiver for space communication through thin clouds. **Applied Optics**, v. 36, n. 9, p. 1987-1993, 20 March 1997.

ASHCROFT, N. W.; MERMIN, N. D. **Solid State Physics**. Orlando: Harcourt College Publishers, 1976. 848 p. ISBN 0-03-083993-9.

ASSIL, K. K. Intraoperative Aberrometry and Limbal Relaxing Incisions. **Cataract and Refractive Surgery Today**, p. 65-67, August 2009.

BAGAYEV, S. N.; RAZHEV, A. M.; ZHUPIKOV, A. A. Excimer Laser Ophthalmic Devices for Eye Microsurgery. **Laser Physics**, v. 8, n. 3, p. 794-798, 1998.

BALLARD, D. H.; BROWN, C. M. **Computer vision**. Englewood Cliffs: Prentice-Hall, Inc., 1982.

BIEHL, S. et al. Refractive Microlens Fabrication by Ink-Jet Process. **Journal of Sol-Gel Science and Technology**, v. 13, n. 1-3, p. 177-182, 1998. DOI: 10.1023/A:1008648615758.

BORN, M.; WOLF, E. **Principles of optics:** eletromagnetic theory of propagation, interference, and diffraction of light. 6th. ed. New York: Pergamon Press, 1989.

BORRELLI, N. F. **Microoptics Technology:** Fabrication and Applications of Lens Arrays and Devices. New York: Marcel Dekker, 1999. 360 p. ISBN 978-0824713485.

CAMERON, P. B.; BRITTON, M. C.; KULKARNI, S. R. Precision astromety with adaptive optics. **The Astronomical Journal**, v. 137, p. 83-93, January 2009.

CARROLL, J. C. et al. Recent advances in retinal imaging with adaptive optics. **Optics and Photonics News**, p. 36-42, January 2005.

CHEN, C.-Y. et al. Reduction of Distortion Aberration in Imaging Systems by Using a Microlens Array. **Optics Communications**, v. 283, n. 14, p. 2798–2802, 15 July 2010. DOI: 10.1016/j.optcom.2010.03.027.

COX, I. G.; KINGSTON, A. C. The Influence of Wavefront Aberrations. **Review of Cornea and Contact Lenses**, 13 October 2011. Acessed in 11/03/2012. Available at: http://www.reviewofcontactlenses.com/content/c/30280/.

CUBALCHINI, R. Modal wave-front estimation from phase derivative measurements. **Journal of the Optical Society of America**, v. 69, n. 7, p. 972-977, July 1979.

DALY, D. et al. The Manufacture of Microlenses by Melting Photoresist. **Measurement Science and Technology**, v. 1, n. 8, p. 759-766, August 1990. DOI:10.1088/0957-0233/1/8/016.

DE LIMA MONTEIRO, D. W. **CMOS-based integrated wavefront sensor**. Delft: Delft University Press, 2002.

DE LIMA MONTEIRO, D. W. et al. Single-mask microfabrication of aspherical optics using KOH anisotropic etching of Si. **Optics Express**, v. 11, n. 18, p. 2244-2252, September 2003.

DE LIMA MONTEIRO, D. W. et al. **Improvement of Dynamics Features of an Adaptive Optical System for Detection and Correction of Ophthalmic Distortions**. NSTI-Nanotech. Boston: [s.n.]. 2006. p. 413-418.

DE LIMA MONTEIRO, D. W.; AKHZAR-MEHR, O.; VDOVIN, G. **Prime microlens arrays for Hartmann-Shack sensors - an economical fabrication technology**. 4th Adaptive Optics Conference for Industry and Medicine. Münster: Springer. 2005. p. 197-205.

DIAZ-SANTANA, L.; WALKER, G.; X BARA´, S. Sampling Geometries for Ocular Aberrometry: A Model for Evaluation of Performance. **Optics Express**, v. 13, n. 22, p. -8818, 31 October 2005. DOI:10.1364/OPEX.13.008801.

FAULKNER, A. R. Aberrometry: How These Devices Work. **Cataract and Refractive Surgery Today**, p. 47-49, July 2011.

FERREIRA JR., A. I.; DE LIMA MONTEIRO, D. W.; PATARO, C. D. M. **Diagnóstico de aberrações ópticas e controle de sistema óptico adaptativo com o método Adaline**. Universidade Federal de Minas Gerais. Belo Horizonte, p. 75. 2006.

FLEXIBLE OPTICAL BV. **Flexible Optical**. Available at: <www.okotech.com>. Access date: 25 January 2010.

FORBES, G. W. Robust and Fast Computation for the Polynomials of Optics. **Optics Express**, v. 18, n. 13, p. 13851-13862, 7 June 2010.

FORBES, G. W. Characterizing the Shape of Freeform Optics. **Optics Express**, v. 20, n. 3, p. 2483-2499, 30 January 2012.

GIRKIN, J. M.; POLAND, S.; WRIGHT, A. J. Adaptive optics for deeper imaging of biological samples. **Current Opinion in Biotechnology**, v. 20, p. 106-110, March 2009.

GREENAWAY, A.; BURNETT, J. **Industrial and medical applications of adaptive optics**. Technology Tracking. [S.l.]. 2004.

GREIVENKAMP, J. E. Interference. In: BASS, M., et al. **Handbook of Optics - Fundamentals, Techniques and Design**. 2nd Ed. ed. New York: McGraw-Hill, Inc., v. 1, 1995. p. 2.3-2.44. ISBN 0-07-047740-7.

GUENTHER, R. D. **Modern Optics**. New York: John Wiley & Sons, Inc, 1990. 712 p. ISBN 9780471605386.

GUYTON, A. C.; HALL, J. E. **Tratado de Fisiologia Médica**. 9th Edition. ed. Rio de Janeiro: Guanabara Koogan, 1997. ISBN ISBN: 85-277-0395-5.

HAMELINCK, R. et al. **Deformable membrane mirror with high actuator density and distributed control**. Proceedings of the Sixth International Workshop on Adaptive Optics for Industry and Medicine. London, UK: Imperial College Press. 2007. p. 35-40.

HARDY, J. W. Adaptive Optics: Technology developed during the cold war is giving new capabilities to ground-based astronomical telescopes. **Scientific American**, p. 40-45, 1994.

HECHT, E. **Optics**. 4th Edition. ed. San Francisco: Addison and Wesley, 2002.

HEIN, M. **Adaptive optics: an introduction and overview**. Portland State University. Portland. 2005.

HOLOHAN, M. L.; DAINTY, J. C. Low-order adaptive optics: a possible use in underwater imaging? **Optics and Laser Technology**, v. 29, n. 1, p. 51-55, 1997.

HUANG, C.-Y. et al. Fabrication of a Double-Sided Micro-Lens Array by a Glass Molding Technique. **Journal of Micromechanics and Microengineering**, v. 21, n. 8, p. 085020 (6pp), August 2011. DOI:10.1088/0960-1317/21/8/085020.

IMAGINE EYES SA. Retinal Image Galery. **rtx1™ Adaptive Optics Retinal Camera**. Available at: <http://www.imagine-eyes.com/content/view/124/127/>. Access date: 09 January 2012. Images acquired at Imagine Eyes during the INOVEO project.

JESACHER, A. et al. Adaptive optics for direct laser writing with plasma emission aberration sensing. **OPTICS EXPRESS**, v. 18, n. 2, p. 657-661, January 2010.

KAMIYA, K. et al. Progression of Pellucid Marginal Degeneration and Higher-Order Wavefront Aberration of the Cornea. **Japanese Journal of Ophthalmology**, v. 47, n. 5, p. 523-525, September-October 2003. DOI: 10.1016/S0021-5155(03)00126-6.

KECK OBSERVATORY; UCLA GALACTIC CENTER GROUP. Cosmic Matters. **W. M. Keck Observatory**, 2007/2008. Available at: <http://www.keckobservatory.org/cosmicmatters/archive/category/winter_2007_spring_2008/>. Access date: 08 January 2012. Topic: Two Beams of Light.

KENDALL, D. L. et al. Micromirror Arrays Using KOH:H2O Micromachining of Silicon for Lens Templates, Geodesic Lenses, and Other Applications. **Optical Engineering**, v. 33, n. 11, p. 3578-3588, November 1994. DOI: 10.1117/12.179881.

KUNNAVAKKAM, M. V. et al. Low-Cost, Low-Loss Microlens Arrays Fabricated by Soft-Lithography Replication Process. **Applied Physics Letters**, v. 82, n. 8, p. 1152-1154, 24 February 2003. DOI: 10.1063/1.1555694.

KURODA, T. et al. Wavefront Analysis of Higher-Order Aberrations in Patients With Cataract. **Journal of Cataract and Refractive Surgery**, v. 28, n. 3, p. 438-444, March 2002. DOI: 10.1016/S0886-3350(01)01176-2.

LAWLESS, M. et al. Keratoconus: Diagnosis and Management. **Australian and New Zealand Journal of Ophthalmology**, v. 17, n. 1, p. 33-60, February 1989. DOI: 10.1111/j.1442-9071.1989.tb00487.x.

LIN, C.-P.; YANG, H.; CHAO, C.-K. Hexagonal Microlens Array Modeling and Fabrication Using a Thermal Reflow Process. **Journal of Micromechanics and Microengineering**, v. 13, n. 5, p. 775-781, September 2003. DOI:10.1088/0960-1317/13/5/333.

LLORENTE, L. et al. Effect of sampling on real ocular aberrations measurements. **Journal of the Optical Society of America A: Opt Image**, v. 24, n. 9, p. 2783-2796, September 2007.

MAEDA, N. Clinical Applications of Wavefront Aberrometry – a Review. **Clinical and Experimental Ophthalmology**, v. 37, n. 1, p. 118-129, January/February 2009. DOI: 10.1111/j.1442-9071.2009.02005.x.

MAEDA, P. Y. Zernike Polynomials and Their Use in Describing the Wavefront Aberrations of the Human Eye. **Applied Vision and Imaging Systems Course Project**, 2003. Available at: <http://scien.stanford.edu/pages/labsite/2003/psych221/projects/03/pmaeda/index.html>. Access date: 15 January 2012.

MALACARA, D. **Optical Shop Testing**. 3rd Edition. ed. New York: John Wiley & Sons, Inc., 2007. 888 p. ISBN 978-0471484042.

MALACARA-DOBLADO, D.; GHOZEIL, I. Hartmann, Hartmann-Shack and Other Screen Tests. In: MALACARA, D. **Optical Shop Testing**. 3rd Edition. ed. New York: John Wiley & Sons, Inc., 2007. p. 361-397. ISBN 978-0471484042.

MANSURIPUR, M. The Shack-Hartmann Wavefront Sensor. **Optics & Photonics News**, v. 10, n. 4, p. 48-51, April 1999. doi: 10.1364/OPN.10.4.000048.

MCMAHON, T. T. et al. A New Method for Grading the Severity of Keratoconus: The Keratoconus Severity Score (KSS). **Cornea**, v. 25, n. 7, p. 794-800, August 2006.

MITCHELL, M. **An introduction to genetic algorithms**. Cambridge, MA: The Mit Press, 1999.

MORENO-BARRIUSO, E. et al. Comparing Laser Ray Tracing, the Spatially Resolved Refractometer, and the Hartmann- Shack Sensor to Measure the Ocular Wave Aberration. **Optometry and Vision Science**, v. 78, n. 3, p. 152-156, March 2001.

NAVARRO, R.; ARINES, J.; RIVERA, R. Direct and inverse discrete Zernike transform. **Optics Express**, v. 17, n. 26, p. 24269-24281, 21 December 2009. doi: 10.1364/OE.17.024269.

NAVARRO, R.; MORENO-BARRIUSO, E. Laser Ray-Tracing Method for Optical Testing. **Optics Letters**, v. 24, n. 14, p. 951-953, 15 July 1999. DOI: 10.1364/OL.24.000951.

NEAL, D. R.; COPLAND, J.; NEAL, D. Shack-Hartmann Wavefront Sensor Precision and Accuracy. In: DUPARRÉ, A.; SINGH, B. **Advanced Characterization Techniques for Optical, Semiconductor, and Data Storage Components (Proceedings of SPIE)**. Bellingham: Society of Photo-Optical Instrumentation Engineers, v. 4779, 2002. p. 148-160. ISBN 978-0819445469.

NEWTON, S. I. **Opticks:** or a treatise of the reflections and refractions, inflections & colours of light. New York: Cosimo Classics, 2007. 110-111 p. Prop. VIII. Prob. II. "To shorten Telescopes."

NINOMIYA, S. et al. Evaluation of Lenticular Irregular Astigmatism Using Wavefront Analysis in Patients With Lenticonus. **Archives Ophthalmology**, v. 120, n. 10, p. 1388-1393, October 2002.

NOLL, R. J. Zernike polynomials and atmospheric turbulence. **Journal of the Optical Society of America**, v. 66, n. 3, p. 207-211, March 1976.

OKO TECHNOLOGIES. **Adaptive Optics Product Guide**. Röntgenweg: [s.n.], 2006. ISBN ISBN: 90-8559-164-3.

OKO TECHNOLOGIES. Technical documents: Typical passports. **Flexible Optical**, 2006. Available at: <http://www.okotech.com/passports>. Access date: 14 January 2010.

OLIVEIRA COSTA, R. F. **Investigação de Aspectos Topológicos de Componentes e Dispositivos Microfabricados em Silício**. Belo Horizonte: Universidade Federal de Minas Gerais - Programa de Pós Graduação em Engenharia Elétrica, 2010. 96 p.

OLIVEIRA, O. G.; DE LIMA MONTEIRO, D. W. Optimization of the Hartmann–Shack Microlens Array. **Optics and Lasers in Engineering**, v. 49, n. 4, p. 521-525, April 2011. DOI: 10.1016/j.optlaseng.2011.01.002.

ONG, N. S.; KOH, Y. H.; FU, Y. Q. Microlens Array Produced Using Hot Embossing Process. **Microelectronic Engineering**, v. 60, n. 3-4, p. 365-379, April 2002. DOI:10.1016/S0167-9317(01)00695-5.

OPTICAL SOCIETY OF AMERICA. **Handbook of Optics:** Fundamentals, Techniques and Design. 2nd Edition. ed. New York: McGraw-Hill, Inc, v. 1, 1994.

OUGHSTUN, K. E. Intracavity adaptive optic compensation of phase aberrations. I: Analysis. **J. Opt. Soc. Am.**, v. 71, p. 862-872, 1981.

PAN, C. T. et al. Hot Embossing of Micro-Lens Array on Bulk Metallic Glass. **Sensors and Actuators A: Physical**, v. 141, n. 2, p. 422-431, 15 February 2008. DOI:10.1016/j.sna.2007.10.040.

PESUDOVS, K.; ELLIOTT, D. B. Refractive Error Changes in Cortical, Nuclear, and Posterior Subcapsular Cataracts. **British Journal of Ophthalmology**, v. 87, n. 8, p. 964-967, August 2003. DOI: 10.1136/bjo.87.8.964.

PLATT, B. C.; SHACK, R. History and principles of Shack-Hartmann wavefront sensing. **Journal of Refractive Surgery**, v. 17, p. 573-577, September/October 2001.

POPOVIC, Z. D.; SPRAGUE, R. A.; CONNELL, G. A. N. Technique for Monolithic Fabrication of Microlens Arrays. **Applied Optics**, v. 27, n. 7, p. 1281-1284, 1 April 1988.

PORTER, J. Principals of eye design. **Center for Adaptive Optics**, 2003. Available at: <http://cfao.ucolick.org/pubs/presentations/eyedesign/06_Aberrations_JP.pdf>. Access date: 10 January 2010.

PORTER, J. et al. Monochromatic aberrations of the human eye in a large population. **Journal of the Optical Society of America**, v. 18, n. 8, p. 1793-1803, August 2001.

PORTER, J. et al. **Adaptive optics for vision science:** principles, practices, design and applications. Jersey City: John Wiley & Sons, 2006. 640 p. ISBN 978-0-471-67941-7.

PRESS, W. H. et al. **Numerical recipes in C:** The art of scientific computing. Second Edition. ed. New York: Cambridge University Press, 1992.

RAZHEV, A. M. et al. Investigating the Action of the 193-nm and 223-nm Radiation of Excimer Lasers on the Cornea of the Human Eye in Refractive Surgery. **Journal of Optical Technology**, v. 76, n. 5, p. 263-267, May 2009. DOI: 10.1364/JOT.76.000263.

ROORDA, A. Adaptive Optics Ophthalmoscopy. **Journal of Refractive Surgery**, v. 16, p. 602-607, September/October 2000.

ROORDA, A. et al. Adaptive optics scanning laser ophthalmoscopy. **Optics Express**, v. 10, n. 9, p. 405-412, 6 May 2002. 405-412.

ROZEMA, J. J.; VAN DYCK, D. E. M.; TASSIGNON, M.-J. Clinical Comparison of 6 Aberrometers. Part 1: Technical Specifications. **Journal of Cataract and Refractive Surgery**, v. 31, n. 6, p. 1114-1127, June 2005. DOI: 10.1016/j.jcrs.2004.11.051.

ROZEMA, J. J.; VAN DYCK, D. E. M.; TASSIGNON, M.-J. Clinical Comparison of 6 Aberrometers - Part 2: Statistical Comparison in a Test Group. **Journal of Cataract and Refractive Surgery**, v. 32, n. 1, p. 33-44, January 2006. DOI: 10.1016/j.jcrs.2004.11.052.

RUSS, J. C. **The image processing handbook**. Fifth Edition. ed. New York: CRC Press, 2007.

SABESAN, R. et al. Vision improvement by correcting high-order aberrations with customized soft contact lenses in keratoconic eyes. **Optics Letters**, v. 32, n. 8, p. 1000-1002, April 2007.

SALLES, L. P.; DE LIMA MONTEIRO, D. W. Designing the Response of an Optical Quad-Cell as Position-Sensitive Detector. **IEEE Sensors Journal**, v. 10, n. 2, p. 286-293, February 2010. DOI: 10.1109/JSEN.2009.2033806.

SHACK, R. V.; PLATT, B. C. Production and Use of a Lenticular Hartmann Screen. **Journal of the Optical Society of America**, New York, v. 61, n. 5, p. 656, May 1971.

SMITH, W. J. **Modern Optical Engineering:** The Design of Optical Systems. Fourth Edition. ed. New York: McGraw-Hill Professional, 2007. 764 p. ISBN 978-0071476874.

SOLOVIEV, O.; VDOVIN, G. Hartmann-Shack test with random masks for modal wavefront reconstruction. **Optics Express**, 13, 14 November 2005.

SOUTHWELL, W. H. Wave-front estimation from wave-front slope measurements. **Journal of the Optical Society of America**, v. 70, n. 8, p. 998-1006, August 1980.

TAN, J. Wavefront Customization Strategies: There Is No One-Size-Fits All Solution. **Cataract and Refractive Surgery Today Europe**, p. 2-3, June 2011.

THE MATHWORKS, INC. The MathWorks: accelerating the pace of engineering and science. **Documentation:** Genetic Algorithm and Direct Search Toolbox, 2010. Available at: <http://www.mathworks.com/access/helpdesk/help/toolbox/gads/f6187.html>. Access date: 31 January 2010.

THEUWISSEN, A. J. P. **Solid-State Imaging with Charge-Coupled Devices**. Dordrecht: Kluwer Academic Publishers, 1995. ISBN 978-0792334569.

THIBOS, L. N. et al. Standards for Reporting the Optical Aberrations of Eyes. **Journal of Refractive Surgery**, v. 18, n. 5, p. S652-S660, September/October 2002.

TYSON, R. K. **Adaptive optics engineering handbook**. 1ª Edição. ed. New York: Marcell Dekker Inc, 1999. 339 p. ISBN 0824782755.

TYSON, R. K. **Principles of adaptive optics**. 3rd Edition. ed. San Diego: Academic Press, 2011.

U.S. DEPARTMENT OF DEFENSE. Airborne laser fact sheet. **The Missile Defense Agency**, 16 September 2009. Available at: <http://www.mda.mil/global/documents/pdf/laser.pdf>. Access date: 5 January 2012.

VDOVIN, G. et al. **Silicon micro-optics for smart light control**. Photonics West - SPIE - MOEMS, Displays and Imaging Systems II. San Jose, CA: Bellingham: SPIE Press. February 2004. p. 135-149.

VDOVIN, G.; LOKTEV, M. Deformable mirror with thermal actuators. **Optics Letters**, v. 27, n. 9, p. 677-679, May 2002.

VDOVIN, G.; LOKTEV, M.; SOLOVIEV, O. **Deformable mirrors based on transversal piezoeffect**. Proceedings of the Sixth International Workshop on Adaptive Optics for Industry and Medicine. London, UK: Imperial College Press. 2007. p. 83-88.

WANG, J. Y.; SILVA, D. E. Wave-Front Interpretation With Zernike Polynomials. **Applied Optics**, v. 19, n. 9, p. 1510-1518, 1 May 1980. DOI: 10.1364/AO.19.001510.

WANG, L.; KOCK, D. D. The Concept of Wavefront-Guided Corneal Surgery. In: KOHNEN, T.; KOCK, D. D. **Cataract and Refractive Surgery**. New York: Springer-Verlag Berlin Heidelberg, 2005. p. 271-287. ISBN 3-540-20046-0.

WELFORD, W. T. **Aberrations of Optical Systems**. New York: Adam Hilger, 1986. 284 p. ISBN 978-0852745649.

WELP, P.; HEUCK, H.-M.; WITTROCK, U. **Intracavity adaptive optics optimization of an end-pumped Nd:** YVO4 laser. Conference on Lasers and Electro-Optics Europe, 2007 and the International Quantum Electronics Conference. CLEOE-IQEC 2007. Munich: [s.n.]. 2007. p. 1.

WEYRAUCH, T. et al. **Fiber coupling with adaptive optics for free-space optical communication**. Proc. SPIE. San Diego, CA, USA: [s.n.]. 2003. p. 177-184.

WRIGHT, A. J. et al. Adaptive optics for enhanced signal in CARS microscopy. **Optics Express**, v. 15, n. 26, p. 18209-18219, 24 December 2007.

WYANT, J. C.; CREATH, K. Basic wavefront aberration theory for optical metrology. In: SHANNON, R. R.; WYANT, J. C. **Applied Optics and Optical Engineering**. Boston: Academic Press, v. XI, 1992. Cap. 1.

YOON, G. Center for adaptive optics. **Principles of Eye Design**, 2003. Available at: <http://cfao.ucolick.org/pubs/presentations/eyedesign/05_aberrations_GY.pdf>. Access date: 5 January 2012.

YOON, G. Wavefront Sensing and Diagnostic Uses. In: PORTER, J., et al. **Adaptive Optics for Vision Science:** Principles, Practices, Design and Applications. New York: John Wiley and Sons, 2006. p. 63-81. ISBN 9780471679417.

YURA, H. T. Imaging in clear ocean water. **Applied Optics**, v. 12, n. 5, p. 1061-1066, May 1973.

ZERNIKE, F. Beugungstheorie des Schneidensverfahrens und seiner verbesserten Form, der Phasenkontrastmethode. **Physica**, v. 1, p. 689-704, 1934.

ZHANG, Y.; POONJA, S.; ROORDA, A. MEMS-based adaptive optics scanning laser ophthalmoscopy. **Optics Letters**, v. 31, n. 9, p. 1268-1270, 1 May 2006.

ZIMMER, K.; HIRSCH, D.; BIGL, F. Excimer Laser Machining for the Fabrication of Analogous Microstructures. **Applied Surface Science**, v. 96-98, p. 425-429, 2 April 1996. DOI:10.1016/0169-4332(95)00498-X.